Growth, Morphology, and Positioning of Microtubule Asters in Large Zygotes

Johnathan L. Meaders

A dissertation

submitted to the

Department of Biology

in partial fulfillment

of the requirements for the degree of

Doctor of Philosophy

Boston College
Morrissey College of Arts and Sciences
Graduate School

Accepted December, 2020

Growth, Morphology, and Positioning of Microtubule Asters in Large Zygotes

Johnathan L. Meaders

Advisor: Professor David R. Burgess, Ph.D

Microtubule (MT) asters are radial arrays of MTs nucleated from a microtubule organizing center (MTOC) such as the centrosome. Within many cell types, which display highly diverse size and shape, MT asters orchestrate spatial positioning of organelles to ensure proper cellular function throughout the cell cycle and development. Therefore, asters have adopted a wide variety of sizes and morphologies, which are directly affects how they migrate and position within the cell. In large cells, for example during embryonic development, asters growth to sizes on the scales of hundreds of microns to millimeters. Due to this relatively enormous size scale, it is widely accepted that MT asters migrate primarily through pulling mechanisms driven by dynein located in the cytoplasm and/or the cell cortex. Moreover, prior to this dissertation, significant contributions from pushing forces as a result of aster growth and expansion against the cell cortex have not been detected in large cells. Here we have reinvestigated sperm aster growth, morphology, and positioning of MT asters using the large interphase sperm aster of the sea urchin zygote, which is historically a powerful system due to long range migration of the sperm aster to the geometric cell center following fertilization. First, through live-cell quantification of sperm aster growth and geometry, chemical manipulation of aster geometry, inhibition of dynein, and targeted chemical ablation, we show that the sperm aster migrates to the zygote center predominantly through a pushing-based mechanism that appears to largely independent of proposed pulling models. Second, we investigate the fundamental principles for how sperm aster size is determined during growth and centration. By physically manipulating egg size, we obtain samples of eggs displaying a wide range of diameters, all of which are at identical developmental stages. Using live-cell and fluorescence microscopy, we find strong preliminary evidence that aster diameter and migration rates show a direct, linear scaling to cell diameter. Finally, we hypothesize that a collective growth model for aster growth, or centrosome independent MT nucleation, may explain how the sperm aster of large sea urchin zygotes overcomes the proposed physical limitations of a pushing mechanism during large aster positioning. By applying two methods of super resolution microscopy, we find support for this collective growth model in the form of MT branching. Together, we present a model in which growth of astral MTs, potentially through a collective growth model, pushes the sperm aster to the zygote center.

Table of Contents

Acknowledgments

I would first like to thank my family, who has supported me since the beginning of my journey as a scientist. My mother, Diana Meaders, has provided me with unwavering encouragement to pursue science throughout elementary, middle, and high school. She has had a direct and nurturing influence on my interest in science from an early age, by encouraging hobbies such as astronomy when giving me my first (and second) telescope. I find personal happiness by the fact that as a kid she encouraged me to use a telescope to look outward toward the stars, and now today I use microscopes to look inward at asters, which is Latin for “star”. I would also like to thank my aunt and uncle, Mel and Phil, who have always had a passion for education, travelling, and charitable work. As a kid they had a large impact on my pursuits in academics, and as a young adult, I found a love for exploring different countries and cultures through charitable work abroad. Their influence encouraged me to live and study science abroad during my undergraduate and Masters education. Last, I would like to thank my wife, Claire, who has been with me throughout the course of my PhD. The emotional and intellectual support she has given me is irreplaceable. Furthermore, for anyone who has ever met Claire, we can all agree that she’s the more enthusiastic out of us two. This enthusiasm spills over into her passion for education and science, and in doing so has set an example that I consciously try draw from as a scientist, and equally important, as a person.

Secondly, I would like to thank my previous research advisors, Rene Medema, Randall King, and Florian Winau for their support and guidance during my initial development as a scientist. I would also like to thank my current and past mentors from my committee. My current committee, Eric Folker, Sarah McMenamin, Vicki Losick, and Chris Field, and previous committee member Laura Anne Lowery, have provided invaluable expertise, criticism, and discussion in guiding me throughout this dissertation. I’m fortunate to have had such talented scientists guide me in ways that encourage critical and thorough science at the highest level.

I would also like to thank the talented undergraduates I had the pleasure of mentoring in the lab. Not only were they wonderful people to work with, but they also taught me a side of science I had not yet experienced – teaching, encouraging and guiding a scientist from their first day in a lab. Their hard work and devotion has been integral to much of the studies presented in this dissertation.

Last, but certainly not least, I thank David Burgess. His day-to-day support, encouragement, and incredibly positive attitude has helped me push through difficult times at the bench. The enormous freedom he has given me, combined with his knowledge and guidance has helped me to thrive through the easy times. His approach to science and mentorship has set an unwavering example that I aspire to follow during my future as a scientist.

Chapter 1. Background and Summary of Thesis

*Background is adapted from a published review article: Meaders JL, Burgess DR. Microtubule-Based Mechanisms of Pronuclear Positioning. *Cells*. 2020;9(2):505. Published 2020 Feb 23. doi:10.3390/cells9020505

1.1 Significance and General Background of Aster Growth and Positioning

The mature oocyte is the starting point of what eventually becomes a fully developed organism composed of multiple organ systems, multicellular tissues, and a multitude of differentiated and undifferentiated cell types in most animals. The first stage of this transformation begins with one of the most complex transitions in cellular and developmental biology-remodeling the oocyte into a totipotent zygote. Even more noteworthy is the fact that the oocyte contains almost everything required, from mRNA transcripts to molecular signaling proteins and machinery, to guide the oocyte-to-zygote transition (Sha et al., 2019).

One exception to this maternally dominated “rule” is the paternal contribution of the centrosome during fertilization, which enters the egg with the sperm pronucleus in most non-parthenogenetic animals (Schatten, 1994). This sperm-derived microtubule organizing center (MTOC) is essential to restore the diploid condition upon union of the male and female pronuclei, which is the defining feature of the zygote (Reinsch and Gonczy, 1998). The transitional period from mature oocyte to zygote is characterized by massive reorganization of the microtubule (MT) cytoskeleton. These MT reorganizations can be subdivided into two general categories, cortical and cytoplasmic. Remodeling the cortical cytoskeleton is centrosome independent and has no known role for union of

maternal and paternal pronuclei. Instead, cortical rearrangements are localized with developmental cues important for development (Nishikata et al., 2019). Conversely, cytoplasmic reorganization of the MT cytoskeleton is centrosome-dependent and results in formation of the radial array of MTs, known as the sperm aster. The sperm aster nucleates from the sperm-derived centrosome, which is attached directly to the male pronucleus. Through a process that is still not fully understood, the sperm aster in many animals moves the male pronucleus to the center of the newly fertilized egg where union of male and female pronuclei occurs prior to mitotic spindle formation. Because the location of pronuclei establishes where the mitotic spindle forms, precise and accurate positioning of the sperm aster and pronuclei within the zygote is critical to determination of the first division axis (Pollard and O'Shaughnessy, 2019; Rappaport, 1961).

Precisely how the MT asters generates and responds to forces to move to the cell center can be described by three different mechanisms, each of which appears to function differently in eggs of different shapes and sizes (Chart 1).The first is through a cortical pulling model in which dynein anchored to the cell cortex attaches to the astral MT plus-ends at the cortex opposite of the side of sperm entry (or front MTs) and generates centering pulling forces through retrograde motility. These MTs also capture the female pronucleus pulling it to the centrosome of the sperm aster, which results in centration of both male and female pronuclei by the end of sperm aster migration. However, this model requires that astral MTs reach the far cortex on the leading, front side of the aster in order for movement to occur (Chart 1). The second mechanism is through pulling forces generated by retrograde flow of cytoplasmic cargo-bound dynein along astral MTs on all sides of the sperm aster. In this model, termed the MT length dependent cytoplasmic pulling model, a MT length asymmetry within the aster results in more dynein dependent force generation on longer MTs relative to shorter MTs (Hamaguchi and Hiramoto, 1986).

Organism/Cell Type	Size	Force Mechanism
S. pombe 	~ 8-15 µm	MT Pushing
C. elegans 	~50 µm	Pulling (Cortical and Cytoplasmic)
L. pictus (urchin)	~100 µm	Cytoplasmic Pulling
D. rerio 	~700 µm	Cytoplasmic Pulling
X. laevis 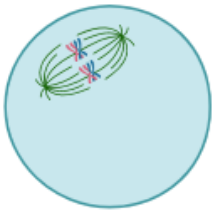	~1.0-1.3 mm	Cytoplasmic Pulling

Chart 1. Comparison of Cell/Egg Sizes Across Model Organisms Commonly Used to Study Aster Positioning.

Accordingly, if MTs at the front of the aster are longer than the rear, then greater pulling forces will be generated in the front relative to the rear and move the sperm aster toward the cell center. The female pronucleus is captured and transported toward the aster center, presumably in a dynein dependent fashion (Reinsch and Karsenti, 1997a). In this sense, the female pronucleus is also considered dynein-bound cargo, which also contributes to force generation during centration. One strength of this model is that front, leading astral MTs are not required to reach the far cortex before aster migration is

permitted, which benefits large embryonic cells and/or zygotes where this distance can be several dozen to hundreds of microns (Chart 1). The third mechanism is a pushing model in which migration of the sperm aster is dependent on polymerization of rear MTs against the cell cortex on the side of sperm entry. In contrast to the pulling mechanisms, the sperm aster expands to the cell center at a rate that is approximately equal to MT polymerization rates of rear cortical facing MTs and independent of growth rates of front cytoplasmic facing MTs. While cortical and cytoplasmic pulling models for sperm aster positioning have been extensively studied, a pushing model has not yet been observed in large developmental models. Instead, it is widely accepted that pushing is not possible during aster positioning in large cell types due to force loss as longer MTs tend to buckle and slip as the grow against surfaces. Therefore, MT-based pushing models during nuclear migration remain exclusive to very small cell types such as *S. pombe* () (Chart 1).

The following sections of the introduction will evaluate historical and recent studies, with a focus on reorganization of the MT cytoskeleton into the sperm aster during the oocyte-to-zygote transition, which is pivotal for centration and union of male and female pronuclei. We will compare the primary model organisms in which pronuclear positioning has been studied, including *Caenorhabditis elegans (C. elegans)*, *Xenopus laevis*, and echinoderms. We will also discuss the current state of our knowledge of the different force generating mechanism for sperm aster and pronuclear migration and describe how these mechanisms relate to the dynamics of sperm aster formation, including aster geometry, MT growth rates, and proximity to cellular boundaries across model organisms. Finally, we will include an assessment of the current gaps in our knowledge of the topic and outline the questions that experimental work performed in this thesis aims to address.

1.2 Sperm aster growth and centration in *C. elegans*

Due to its powerful genetic tool kit and optically tractable eggs, *C. elegans* is one of the most thoroughly studied models for the assembly and migration of sperm asters. *C. elegans* eggs represent a ~50 um oval-shaped cell type, consisting of the future anterior end containing the maternal meiotic spindle and the future posterior end where fertilization and entry of the male pronucleus occurs (Figure 1A) (Wu and Griffin, 2017). The unfertilized egg is arrested in meiosis I, which resumes upon fertilization resulting in formation of the female pronucleus upon meiotic completion (McNally and McNally, 2005). During the time period between fertilization and formation of the female pronucleus, maturation of the paternal centriole is suppressed and held in place at the posterior cortex by F-actin and kinesin-1 in order to prevent premature capture of the meiotic spindle by the sperm aster (McNally et al., 2012; Panzica et al., 2017). After fertilization and completion of meiosis II, centrosome maturation occurs due to recruitment of γ-tubulin and other maternally supplied factors, resulting in dynein-dependent separation of the centrosomes and sperm aster formation (Figure 1B) (Gönczy et al., 1999; Hamill et al., 2002; Kemp et al., 2004; Pelletier et al., 2006). The morphology of the sperm aster in this model was first observed by immunofluorescence revealing two MTOCs attached to the male pronucleus at the future posterior end of the cell (Albertson, 1984). These centrosomes migrate to opposite sides of the male pronucleus, orienting their bipolar axis perpendicular to the anterior-posterior axis at the onset of the first mitotic prophase. This centrosome pair then nucleates MTs which contact the nearby cortex behind the male pronucleus (Albertson, 1984), which was later found to deliver determinants to establish the posterior-anterior axis (Figure 1B) (Lang and Munro, 2017). As these aster pairs begin to grow, an early aster asymmetry becomes apparent. Front MTs oriented toward the anterior side of the egg are longer than rear MTs growing toward the posterior side, interacting with the cortex (Albertson, 1984). These longer front MTs are responsible for capturing and transporting the female pronucleus toward the male pronucleus in a dynein-

dependent manner (Figure 1C) (Malone et al., 2003). Around this time point, the sperm aster pair, along with the female pronucleus (termed the pronuclear complex or PNC), migrates toward the cell center. During this phase, known as the centration phase, the sperm asters orient perpendicular to the anterior-posterior axis, located between the male and female pronuclei. As the PNC approaches the cell center rotation of the asters occurs, orienting them parallel with the anterior-posterior axis (Figure 1D). Finally, the PNC is displaced posteriorly, as the first mitotic spindle begins to form, resulting in the diploid zygote (Figure 1E).

The force generating mechanisms governing centration and posterior migrations in *C. elegans* have been systematically investigated in a series of genetic loss of function studies. First, it was established that dynein and MTs are required for faithful aster centration in this system (Gönczy et al., 1999; Hamill et al., 2002; Pelletier et al., 2006), which suggests that a pulling mechanism along MTs is the predominant force driver. Which pool of dynein, cortical, cytoplasmic, or a combination of both, contributes to aster centration has been a topic of numerous studies within the field. RNAi-mediated inhibition of cortical factors required for dynein recruitment results in faster migration of sperm asters during centering (Albertson, 1984; Lang and Munro, 2017), while posterior displacement after rotation of the PNC is abrogated (Albertson, 1984; Kimura and Onami, 2007; Malone et al., 2003; De Simone et al., 2018; Zipperlen et al., 2001). These studies indicate that cytoplasmic dynein is the primary candidate for generating centering pulling forces on the sperm asters during centration, which are counteracted by cortical pulling forces (Figure 1B inset). These cortical pulling forces then take over to displace the forming mitotic spindle during posterior movements (Figure 1E inset). Furthermore, because total dynein inhibition abrogates aster centration, it's believed that MT polymerization against the cortex does not significantly contribute to sperm aster migration (Gönczy et al., 1999).

Conversely, a more recent study using magnetic tweezers to pull the aster pair anteriorly or posteriorly after aster migration is complete implicates spring-like forces which maintain the position of aster pairs, which is consistent with MT-based pushing mechanisms (Garzon-Coral et al., 2016). Finally, while kinesin-1 is required to prevent premature centrosome maturation and pronuclear migration (McNally et al., 2012), it is still unknown if kinesins-1 and/or other kinesins are essential for pronuclear migration during the centration phase, which would implicate potential and substantial motor-driven pushing forces. However, a contribution of pushing forces to aster movement is still unclear.

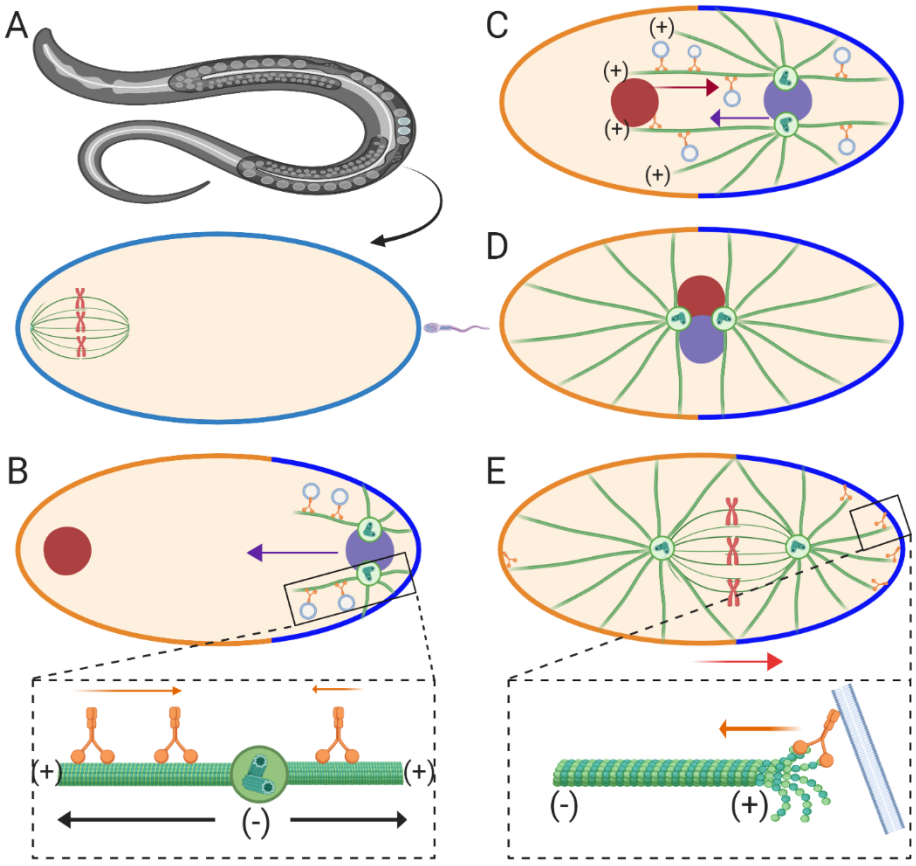

Figure 1. Fertilization and pronuclear migration in *C. elegans*.

(**A.**) The *C. elegans* oocyte is arrested in metaphase of meiosis I just prior to fertilization. The meiotic spindle is located on the future anterior end of the oocyte, while the sperm/male pronucleus enters on the future posterior end.

(**B.**) Early centration phase. Fertilization prompts the completion of meiosis and formation of the female pronucleus (red circle). After sperm entry and maturation of the paternally derived centrioles, two sperm asters form oriented on opposite sides of the male pronucleus (purple circle), perpendicular to the anterior-posterior axis. These asters help define the posterior half (bright blue plasma membrane). The asters migrate toward the egg center due to cytoplasmic dynein-dependent pulling forces that scale with MT length (inset). Force (black arrows) is generated in the opposite direction of movement (orange arrows). Therefore, more force is generated on the longer front MTs relative to the short rear/cortical facing MTs.

(**C.**) Late centration phase. The aster pairs expand during the centration phase, enlarging the posterior half relative to the anterior half of the egg (blue and orange membrane, respectively). The female pronucleus is captured by long front astral MTs and is transported to the male pronucleus by dynein.

(**D.**) Maintenance phase. The combined male and female pronucleus (pronuclear complex or PNC) finish migrating to the egg center and rotate. This rotation orients centrosomes parallel to the anterior-posterior axis.

(**E**.) Posteriorization phase. Nuclear envelope breakdown occurs, combining maternal and paternal chromosomes as the first mitotic apparatus forms in the zygote. The apparatus is pulled toward the posterior side by more dynein activity at the posterior half relative to the anterior (inset). MT catastrophe is also considered as a potential mechanism to generate forces (inset).

In a cytoplasmic dynein-dependent pulling model, retrograde movement of dynein/cargo is expected to generate pulling forces on all sides of the aster (Hamaguchi and Hiramoto, 1986; Shinar et al., 2011). How does pulling on all sides of the sperm aster translate into directionally applied forces and migration rates? The asymmetric geometry of the sperm aster during the centration phase reveals longer MTs in front of the centrosome pair growing deep into the cytoplasm compared to the rear MTs limited by the posterior cortex. If cytoplasmic dynein-dependent force scales with MT length, then we can assume that

more force will be generated along the front astral MTs relative to the rear, driving aster migration in the direction of the longest MTs (Hamaguchi and Hiramoto, 1986) (Figure 1B inset). This cytoplasmic MT length-dependent pulling hypothesis was first modeled *in silico* using *C. elegans* (Kimura and Onami, 2005). Computer simulations predict that in the MT length-dependent pulling model, migration rates of the sperm aster pair will fit a sigmoidal curve when plotted as migration distance vs. time. Conversely, a pushing model should display a convex curve in which rates positively scale with the number of MTs polymerizing against the rear cortex (Kimura and Onami, 2005). While tracking PNC migration during the centration phase, rates match a sigmoidal curve suggesting that the asters are being pulled by cytoplasmic pulling forces, which positively scale with MT-length. These sigmoidal migration dynamics were more recently confirmed by an independent study, which also showed an increase in migration rates upon removal of cortical antagonistic factors, providing compelling evidence for a MT-length dependent cytoplasmic pulling model during the centration phase in *C. elegans* (De Simone et al., 2018). However, the MT growth rate parameters used to simulate migration curves in a pushing model assume non-variable MT growth rates (Kimura and Onami, 2005). While MT growth rates have not been measured with precise temporal resolution during the centration phase, average MT growth rates during early pronuclear migration are highly variable (Srayko et al., 2005). An alternative, untested hypothesis is MT growth rates start off slow as the sperm asters are forming, then increase during the bulk of the migration phase, and slow down as the sperm aster approaches the egg center, which would also result in a sigmoidal migration curve for a pushing model. Future work measuring MT growth rates with high temporal resolution throughout the aster centration phase in *C. elegans* will help test this hypothesis. Finally, what are the exact membrane bound cytoplasmic cargoes that anchor dynein in order to generate MT-length dependent pulling forces? Evidence for endocytic transport is implicated in generating cytoplasmic pulling forces (Kimura and Kimura, 2011). By

inhibiting different Rab-coated endocytic transport, it was shown that the PNC moves at a slower rate during the centration phase. Furthermore, centration rates of the sperm aster pair are increased when retrograde transport of the largest cargo, the female pronucleus, is inhibited in a background lacking cortical antagonistic factors (De Simone et al., 2018). Another cytoplasmic dynein/cargo interaction that could result in pulling forces on the sperm aster is dynein-mediated transport of the endoplasmic reticulum (ER). By interacting with the ER through membrane contact sites, endomembrane compartments, such as lysosomes bound to dynein, may transport the endomembrane and its associated ER retrograde toward the MTOC (Bonifacino and Neefjes, 2017). These endomembrane/ER interactions increase the size and drag of the cytoplasmic anchor for dynein, which in turn should increase the amount of effective pulling forces each dynein motor may generate on the sperm aster. Indeed, ER has been shown to undergo massive retrograde migration and accumulation around the centrosomes of the centering sperm aster (Terasaki and Jaffe, 1991), making it a strong candidate for generating cytoplasmic pulling forces. Future work focusing on other cargoes will be required to elucidate the identity of new cytoplasmic cargo and the specific contributions of different cargoes required for generating cytoplasmic pulling forces.

Generation of pulling forces due to cortical factors during the posterior-directed movements of the asters after centration are relatively straightforward upon initial observation. That is, cortically bound dynein can anchor astral MTs and generating pulling forces through retrograde motility (Figure 1E inset). However, how dynein moves the centered asters specifically toward the posterior side of the egg is more complex. This problem is solved by an asymmetric distribution of dynein at the cortex in which dynein is more concentrated along the posterior half than the anterior (McNally, 2013). Therefore, more dynein-dependent pulling forces are generated on the posterior side of the egg than

the anterior, resulting in a shift of the aster pair posteriorly (Figure 1E). A second potential mechanism used to generate pulling forces is depolymerization of cortically anchored MT plus-ends (Figure 1E inset) (Kozlowski et al., 2007; Nguyen-Ngoc et al., 2007). Experiments using taxol to study the role of MT dynamics in these posterior movements suggest that regulated MT depolymerization may be responsible for generating the required pulling forces (Nguyen-Ngoc et al., 2007). Other work shows a strong correlation between MT catastrophe and aster movement (Kozlowski et al., 2007). MT depolymerization-dependent pulling was directly shown more recently *in vitro*. Dynein was artificially anchored to a barrier, where it was directly shown to attach and negatively regulate the lengths of MT lengths (Laan et al., 2012). However, a potential role for dynein-dependent catastrophe-mediated pulling during aster positioning has not yet been directly characterized *in vivo* using a developmental model.

1.3 Sperm aster growth and centration in echinoderms

In contrast to *C elegans*, the echinoderm egg is a perfectly spherical, ~80~200 um diameter, non-polarized oocyte. Additionally, the oocyte of some echinoderms, such as sea urchins, have already completed meiosis before fertilization occurs (Figure 2A), which results in stark differences compared to *C. elegans*. In the sea urchin, the female pronucleus has already formed in the mature oocyte, and can be located anywhere in the cytoplasm (Peng and Wikramanayake, 2013). Similarly, fertilization occurs at spatially indiscriminate locations around the oocyte plasma membrane (Figure 2A). Therefore, the male and female pronuclei are positioned at random locations relative to each other just after fertilization, rather than at opposite poles as in *C. elegans*. Because of this initial location, engagement between the male and female pronucleus also occurs at seemingly random time points after fertilization, sometimes resulting in fusion of the male and female

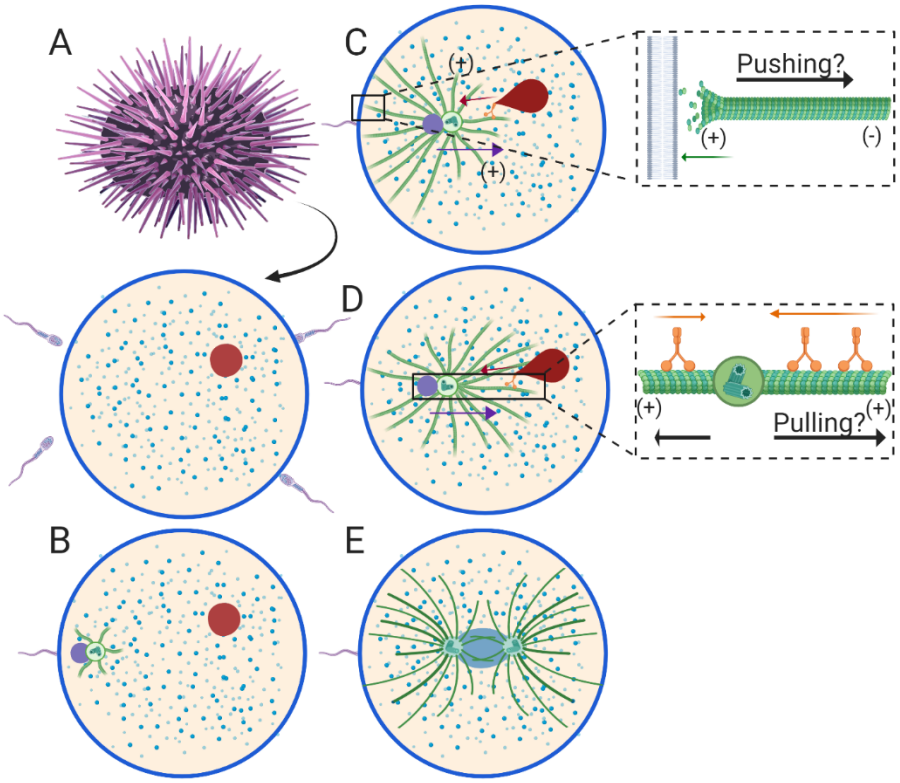

Figure 2. Fertilization and pronuclear migration in the sea urchin (echinoderm).

(**A**.) The sea urchin oocyte has already completed meiosis resulting in formation of the female pronucleus (red circle), which is located randomly within the oocyte cytoplasm. Fertilization may also occur anywhere around the oocyte.

(**B**.) Almost immediately after fertilization, the paternally-derived centrosome is attached to the male pronucleus (purple circle) and begins forming the interphase sperm aster near the cortex. During this early time-point the sperm aster does not begin to migrate until astral MTs reach the rear cortex. (**C. and D**.) As the sperm aster grows, it enters the centration phase where it reaches a constant maximum speed. This velocity is either set by growth rates of rear cortical facing MTs pushing against the cortex as in

(**C**.), cytoplasmic dynein-dependent pulling forces that scale with MT lengths as in

(**D**.), or a combination of the two. The female pronucleus is captured by astral MTs and is presumably transported towad the aster center/male pronucleus by dynein. Transport causes the female pronucleus to form a “tear drop” shape

(**E**.) The sperm aster slows down as it approaches the egg center, prophase centrosomes separation occurs, and pronuclei fuse forming the zygote nucleus (blue oval).

pronucleus before centration has even completed. The engagement between the sperm aster and the female pronucleus and subsequent retrograde transport is presumably dynein-dependent in echinoderms (Figure 1C and 1D). However, direct testing of this hypothesis has yet to be performed. Another difference when compared to *C. elegans* is that there is no requirement for sperm aster formation and migration to be delayed while the maternal chromosomes complete meiosis in sea urchin eggs. Accordingly, centrosome maturation, sperm aster growth, and migration begin almost immediately after the male pronucleus enters the egg cytoplasm (Chambers, 1939).

Initial immunofluorescence observation of the echinoderm sperm aster revealed an interphase sperm monaster, which appears to expand as it approaches the cell center (Bestor and Schatten, 1981; Hamaguchi et al., 1985; Harris et al., 1980). These early studies describe three phases of sperm aster migration distinguished by different migration rates, throughout the centration

process. The first phase is just after fertilization (Figure 2B), when the asters can be described as “small stars” (Harris et al., 1980) and move at a rate of ~3.5 um/min (Schatten, 1981). Another independent study indicates that the aster during this phase has a symmetrical geometry, as it is beginning to grow (Chambers, 1939). The second phase consists of the bulk of aster expansion and the majority of the movement toward the egg center at rates of ~4.9 um/min. Bright field microscopy of aster geometry during this phase describes an asymmetric aster geometry in which rear/cortical MTs grow at a faster rate

than front MTs leading into the cytoplasm, which is consistent with a pushing model (Figure 2C) (Chambers, 1939). A later independent study using DIC microscopy indicates that the male pronucleus does not begin moving until expansion of rear MTs contact and grow against the rear cortex, leading to the conclusion that the aster is pushed to the cell center (Hamaguchi and Hiramoto, 1980). During the third phase, the aster slows down to ~2.6 um/min as it nears the center, and centrosome separation around the newly formed zygote nucleus results in two large asters that completely fill the cytoplasm (Figure 2E). These three phases of aster migration were recently reconfirmed in an independent study using updated methods for tracking sperm aster migration (Tanimoto et al., 2016).

One caveat of echinoderms as a model system is they lack genetic tools to study aster formation and pronuclear migration. However, because they are very malleable, clear, and not yet polarized, echinoderm eggs represent a powerful live-cell system to study the biophysical principles of how aster geometry translates to migration rates and directional forces. Previous work describes a prominent network of astral MTs extending to the cortex, which were originally predicted to push the sperm aster to the cell center (Figure 2C) (Bestor and Schatten, 1981). Additionally, MTs don't reach the far opposite cortex until the third phase of aster migration, when centrosome separation occurs and migration rates come to a halt (Figure 2E), indicating that cortical pulling mechanisms are not a contributing factor. However, subsequent work using the MT inhibitor, colcemid, weakened this pushing hypothesis in sand dollar eggs (Hamaguchi and Hiramoto, 1986). In a hallmark study, eggs were treated with colcemid and then fertilized. Following fertilization, colcemid was deactivated with UV irradiation in a 50-60 um diameter region of the egg containing the male pronucleus. When the male pronucleus is at the periphery of the irradiated region, it migrates toward the geometric center of the region where it comes to a halt. In other words, male pronuclear migration occurs in the direction of the

longest astral MTs until it reaches the center of the irradiated region, where MT lengths are presumably equal on all sides of the aster (Figure 2D inset). These experiments provided the first evidence for a MT length-dependent cytoplasmic pulling mechanism in any model organism (Hamaguchi and Hiramoto, 1986).

More recently, modern techniques utilizing laser ablation, magnetic tweezers and *in silico* modeling have revisited the MT-length dependent pulling model, investigating how such a model accounts for aster migration direction and speeds in the sea urchin (Minc et al., 2011; Sallé et al., 2018; Tanimoto et al., 2016, 2018). Laser ablation of side portions of the sperm aster results in drift of the male pronucleus away from the side of ablation in a MT-dependent manner, indicating that it is being pulled from the opposite side where MTs are theoretically longer (Tanimoto et al., 2016). Likewise, by using magnetic tweezers, the aster is pulled perpendicular to the centration path. When the magnets are released, the aster resumes migration toward the cell center, in the direction of the theoretically longest MTs (Tanimoto et al., 2018). Together, these series of experiments suggest that aster directionality is maintained by forces on side astral MTs that scale with MT length. Additionally, ablations along front, cytoplasmic facing MTs results in momentary pauses in aster forward migration (Tanimoto et al., 2016), suggesting pulling forces at the front of the aster. Mathematical and computational modeling of the sperm aster in this same study suggests that aster migration rates are determined by growth rates of the sperm asters, where speed is equal to the length of front astral MTs minus the length of rear astral MTs (Figure 2D inset). Together, this body of literature suggests MT-length dependent pulling forces driven by cytoplasmic dynein are predominant during aster migration and centration in echinoderms. However, while global inhibition of dynein using Ciliobrevin D halts aster migration in the sea urchin, inhibition of dynein during laser ablation, magnetic redirection, and colcemid experiments has not yet been tested (Hamaguchi and Hiramoto, 1986;

Tanimoto et al., 2016, 2018). Therefore, the presumed role of dynein in the observed movements away from the site of ablation, away from the released magnets, and toward the center of UV irradiated colcemid regions, respectively, is currently unknown. Moreover, while side and front astral MTs have been manipulated in these studies, experiments manipulating the MTs growing against the rear cortex at the site of sperm entry have not been conducted. Such manipulation experiments will more directly test if MT pushing may drive aster forward migration (Reinsch and Gonczy, 1998). Finally, the MT length dependent pulling model critically depends on a particular aster geometry in which the front/cytoplasmic facing radius must be longer than the rear/cortical facing radius (Figure 2D) (Tanimoto et al., 2016). Earlier characterization of aster geometry using bright field and DIC microscopy suggests that the rear/cortical radius of the aster expands faster than the front radius during the migration phase, which is consistent with a pushing model and challenges the MT-length dependent pulling model (Figure 2C) (Chambers, 1939). However, modern approaches to characterize sperm astral MT lengths and dynamics in live cells have not yet been reported. These measurements will prove particularly important to thoroughly investigate these conflicting models.

1.4. Sperm Aster Growth and Centration in *Xenopus*

Amphibian eggs represent extremely large cells, sometimes reaching diameters of up to 1 mm. Accordingly, pronuclei must undergo extremely long migration distances compared to *C. elegans* and echinoderms. The earliest accurate studies of pronuclear migration dynamics were performed in the amphibian (Roux, 1885). Before fertilization, the egg is arrested in metaphase II of meiosis, much like in *C. elegans*, and the meiotic spindle is located at the animal pole (Figure 3A). Fertilization occurs randomly along the animal half of the egg and triggers completion of meiosis, resulting in formation of the female pronucleus. Meanwhile, paternal centrosomes carried by the sperm nucleate the

interphase sperm aster (Figure 3B). Immunofluorescence microscopy of the sperm aster reveals massive expansion into the egg cytoplasm within the animal pole, which eventually captures the female pronucleus (Figure 3C) (Wühr et al., 2010). The sperm aster then carries the male and female pronuclei toward the center of the egg, just above the yolk-dense vegetal half. Here, onset of the first mitosis occurs, and fusion of the maternal and paternal DNA completes, forming the diploid zygote (Stewart-Savage and Grey, 1982).

Due to the opaque properties of the frog egg, modern live-cell investigations of sperm aster growth and migration dynamics are notably limited. However, experiments combining microinjection and fixed-cell immunofluorescence microscopy have shed light on how the sperm aster positions pronuclei at the cell center. As the sperm aster expands, MT lengths are restricted by the cortex proximal to the site of sperm entry (Wühr et al., 2010). Conversely in front of the aster, MTs are not near long enough to contact the opposite cortex ruling out a cortical pulling model. Therefore, much like in *C. elegans* and sea urchins, the centration mechanisms are likely due to either pushing from MT polymerization against the rear membrane or from pulling in the cytoplasm by dynein bound to its cargo. To test for dynein-dependent pulling, eggs were injected with a dominant negative fragment of the dynactin complex (p150-CC1) after fertilization and processed for immunofluorescence microcopy at varying time-points post-fertilization. Injected eggs displayed reduced sperm aster migration dynamics when compared to controls. Furthermore, aster morphology in injected eggs display centrosomes still near the cortex, with a longer front aster radius reaching into the cytoplasm, and a shorter rear aster radius limited by the rear cortex

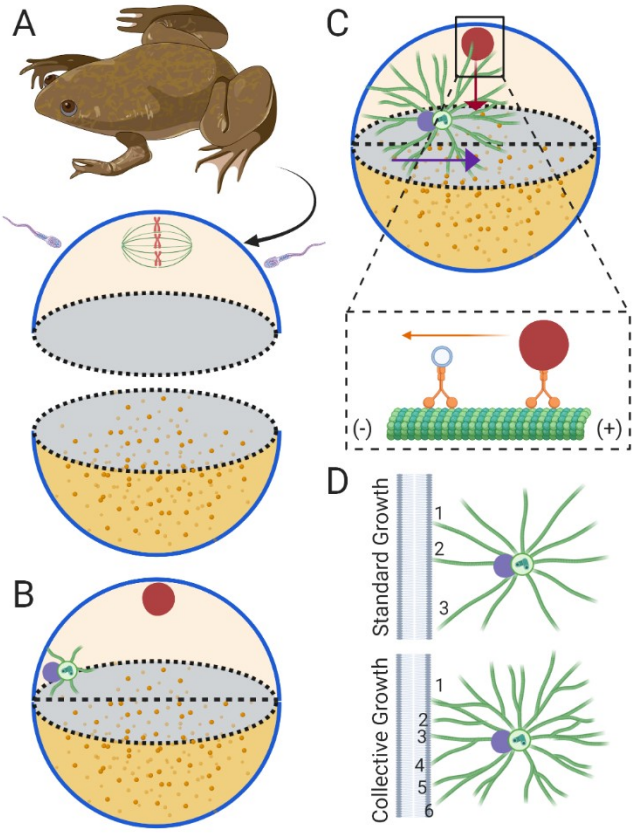

Figure 3. Fertilization and pronuclear migration in *Xenopus*.

(A.) The frog oocyte is arrested in metaphase II of meiosis. The meiotic spindle is located at the pole of the animal half of the egg (top beige hemisphere). The sperm can fertilize the egg along the side of the animal half. The yolky vegetal half is illustrated as the lower dark yellow hemisphere.

(B.) Fertilization resumes the cell cycle resulting in formation of the female pronucleus (red circle) near the animal pole after meiosis completes. The paternally derived centrosomes begin forming the interphase sperm aster attached to the male pronucleus (purple circle).

(C.) The sperm aster expands and migrates toward the center of the egg, just above the vegetal half. As the astral MTs contact the female pronucleus it is transported retrograde along astral MTs in a dynein dependent manner (inset). Furthermore, cytoplasmic dynein/cargoe (inset) likely generates pulling forces through retrograde transport.

(D.) Simplification of sperm aster growth according the standard growth model (top) and the collective growth model (bottom). The standard growth model predicts that asters are formed solely

from centrosome-nucleated MTs, while the collective growth model includes MT-dependent MT nucleation, or MT branching. When considering pushing forces due to MT polymerization against the cell cortex, long individual MTs (numbered 1-3) nucleate from the centrosome and bear a high compression load, which can lead to MT buckling and decentering (see text for details). However, this problem is solved by the collective growth model in which the compression load is redistributed to a greater number of short MTs (numbered 1-6) polymerizing against the cortex.

(Wühr et al., 2010). Together, these experiments provide strong support that dynein in the cytoplasm is required to pull the sperm aster to the egg center (Figure 3C).

While live cell experimentation in amphibian eggs is challenging, the use of *Xenopus* egg extracts provides a powerful model for *in vitro* studies of aster growth dynamics and positioning of male and female pronuclei (Field and Mitchison, 2018; Murray and Kirschner, 1989). The requirement of dynein during female pronuclear translocation along MTs were first directly tested in *Xenopus* interphase egg extracts (Reinsch and Karsenti, 1997b). Magnetic beads were used to bind DNA and form an artificial nucleus lacking a centrosome. These nuclei move along MTs toward purified centrosomes ends at rates comparable to those measured during female pronuclear migration in echinoderms (Schatten, 1981), and inhibition of dynein using blocking antibodies or vanadate abrogates these movements. Importantly, the extracts in which purified nuclei and centrosomes were diluted consists of the cytoplasm taken directly from interphase eggs, providing strong support that female pronuclear migration along interphase sperm asters is dynein dependent (Figure 3C). Determining if *Xenopus* female pronuclear migration along the sperm aster is dynein dependent *in vivo* may prove challenging because dynein also appears to be required for migration of the sperm aster. Additionally, the mechanisms required for precise control of migration and positioning of large interphase sperm aster using *Xenopus* extracts has not yet been tested. By using micro-fabricated chambers matching the sizes and shapes of eggs from different model organisms, these extracts will

provide a rich reconstitution system for uncovering the exact contribution of differing mechanisms during sperm aster centration.

More recently, *Xenopus* extracts have prompted a reconsideration for how large MT asters grow in developmental systems. So far we have only considered astral MTs nucleated from the paternally inherited centrosome, also known as the radial elongation model of aster growth (Figure 3D top) (Bergen et al., 1980). However, work using both interphase and meiotic *Xenopus* egg extracts has led to the discovery that these especially large asters nucleate MTs remote from the centrosome, termed the collective growth model (Figure 3D bottom) (Ishihara et al., 2014; Petry et al., 2013). In meiotic egg extracts, these centrosome-independent MT nucleation events occur through a process of MT-dependent MT nucleation, or MT branching (Petry et al., 2013). The first question that the collective model answers is how can an aster radius span the large cytoplasm of large oocytes after fertilization? In the radial elongation model, this would mean individual centrosome-nucleated MTs, whose lengths are bound by dynamic instability at their plus-ends (Mitchison and Kirschner, 1984), must grow hundreds of microns in lengths to span the cytoplasm. However, in the collective growth model, parental MTs nucleated at the centrosome nucleate subsequent daughter MTs along their sides, and these daughter MTs may then nucleate new MTs in a branched network spanning large distances (Figure 3D bottom). This branching was also recently predicted to account for the increase in MT density observed in the *Xenopus* sperm aster at distances remote from the centrosome in fixed immunofluorescence images. That is, the number of MTs increases as a function of distance from the centrosome (Ishihara et al., 2014, 2016). While elaborate *in vitro* studies are currently focusing on the mechanisms and dynamics of MT branching during aster growth (Alfaro-Aco et al., 2017, 2020; King and Petry, 2020; Song et al., 2018; Thawani

et al., 2019), future work determining if sperm asters contain branched MTs *in vivo* will be required.

The collective growth model also has strong implications for the mechanisms required for sperm aster positioning and pronuclear migration. First, one limitation to the pushing model for aster positioning in large asters is the extremely high number of MTs that would be required to push a large sperm aster over large distances through the highly viscous cytoplasm. This number was estimated to be approximately 12,000 MTs midway through centration in *Xenopus* sperm asters (Reinsch and Gonczy, 1998). Such a high estimate is partially due to *in vitro* data indicating that as MTs become longer they tend to buckle, resulting in a loss of centering forces (Figure 3D bottom) (Bjerknes, 1986; Dogterom and Yurke, 1997; Dogterom et al., 2005; Holy et al., 1997). In smaller cell types such as *S. pombe,* short MTs can push nuclei into the correct position prior to cell division through microtubule polymerization against the cell cortex (). Similarly, in large cells we hypothesize that a collective growth model will permit compression loads to be redistributed among many shorter branched MTs growing at the cortex in a , rather among long individual MTs that are prone to buckling and slipping (Figure 3D). This redistribution of the compression load across a network of branched astral MTs, should reduce the required number of MT polymerization events at the cell cortex to move large sperm aster. Additionally, MT branching should result in more MT polymerization events occurring against the cell cortex when compared to the standard growth model (Figure 3D). Modeling how this force would be redistributed among a branched network and how many polymerization events would be required to generate enough pushing will be required to test this hypothesis. A second implication to consider is retrograde transport of organelles, including the female pronucleus, along a branched network of MTs. In other words, how can transport of cargo ranging from small vesicles to the large female pronucleus occur

through a dense network of branched astral MTs? One hypothesis is that dynein and its bound cargo can switch from one MT to another during migration (Rouvière et al., 1994). However, in such a model, whether or not the female pronucleus can maintain the recorded migration rates (~0.24 um/second) is unknown.

1.5. Major gaps in the field

Decades of research using *C. elegans*, echinoderm, and *Xenopus* eggs suggests a relatively conserved mechanism in which sperm aster positioning is dominated by dynein dependent pulling forces in the cytoplasm that may scale with MT length. Despite the major evolutionary differences between the model organisms presented here, all three have adopted a pulling mechanism, which appears essential for aster and pronuclear positioning. From an evolutionary perspective, this is likely due to the relatively large size of zygotes requiring long migration distances for the sperm aster and pronuclei to reach the cell center. These distances present physical constraints when considering a pushing model (Figure 3D), which may have resulted in convergence of these organisms on a pulling model.

The potential for collective growth during aster formation may solve the physical constraints on long range migration of MT structures such as the sperm aster, making the argument for pushing based-mechanisms far more plausible (Figure 3D). While the dogma that dynein function is essential for pronuclear migration has been well established, whether or not dynein is sufficient is still an important unanswered question. That is, are there any roles for MT-based and/or motor based pushing models during aster migration? If the sperm aster lacks potential pushing factors such as rear/cortical MTs or kinesin function, can dynein-dependent pulling still move the sperm aster to the cell center with

the pronuclei in tow? If not, pushing mechanisms may be just as important to position pronuclei as dynein-dependent pulling.

1.6 Summary of Thesis

Chapter II (In Review in Cell Reports): We utilize the transparent sea urchin zygote of *Lytechinus pictus* to revisit the mechanism(s) of sperm aster centration. As outlined above, elegant *in silico* modelling has provided evidence for a dynein-dependent MT-length dependent pulling mechanism as the predominant force generator during aster centration (Tanimoto et al., 2016, 2018). However, thorough experimentation to complement this modelling has yet to be performed in the sea urchin system. First, the MT-length dependent pulling mechanism is dependent on a very specific aster geometry in which front aster radii are longer than rear. We therefore aimed to determine the geometry of the sperm aster as it grows and migrates toward the zygote center. While aster geometry has been investigated by immunofluorescence microscopy (Tanimoto et al., 2016), we improved upon existing analysis by performing live-cell fluorescence imaging and quantification of sperm aster growth and dynamics for the first time. By microinjecting eggs with EB1-GFP and Tau-mCherry, we were able to follow the sperm aster from initial fertilization to centration and measure aster front and rear radii in real-time. To our surprise, we find that aster rear radii are longer than front during sperm aster migration, which precludes the MT length dependent-pulling model.

Second, we take advantage of our live-cell methodology to compare aster migration dynamics with aster growth dynamics. To this end, we find that aster migration rates matches growth rates of rear aster radii remarkably well. Conversely, front radii grow at a steady linear rate and do not change as aster migration rates change. When we increase

or decrease aster growth rates using chemical manipulation, aster migration rates also increase or decrease, respectively. Importantly, in these conditions, sperm aster migration matches growth rates of rear radii, but not front, which is a hallmark of a pushing model rather than the widely accepted MT length-dependent pulling model.

Third, we aim to investigate a role for dynein during aster centration in the sea urchin. This has only been tested using the general ATPase inhibitor, ciliobrevin, which was shown to be non-specific for dynein inhibition (Roossien et al., 2015). While the use of ciliobrevin is appropriate during preliminary experimentation of dynein-dependency for aster migration, more specific methods of dynein inhibition are required. Therefore, we co-injected p150-CC1, a dominant-negative inhibitor of dynein/dynactin interactions, with Tau-mCherry and imaged sperm aster migration using live-cell confocal microscopy. Rather than causing a halt in sperm aster migration, as predicted by a pulling model, we find that the sperm aster migrates to the cell center. Even more noteworthy, sperm aster migration rates are significantly higher in p150-CC1 injected zygotes when compared to controls. Together this data argues that dynein instead acts antagonistically to aster centration forces. In our revised model for aster centration, we hypothesize that aster migration rates may be set by an interplay between pushing by rear aster growth, and a still unidentified antagonistic force driven by dynein dependent pulling. We support this model with data showing that, when rear aster growth rates are increased, aster migration rates increase (outlined in the above paragraph). Likewise, when dynein activity is decreased, aster migration increases.

Last, as outlined in the background above, while dynein is widely believed to be essential for aster migration, it has not yet been tested if dynein is sufficient for aster migration. In other words, when rear portions of the sperm aster are removed, can dynein still pull the sperm aster to the cell center? To directly address this question we performed chemical

ablations with a light inducible MT depolymerizing compound called Caged-Combretastatin 4 (CA4). When we activate the drug using UV light in the rear portion of the sperm aster, migration comes to an almost immediate halt, indicating the dynein-dependent pulling is not sufficient for aster migration in the sea urchin, and pushing by rear MTs is essential to aster migration. Additionally, front ablations of the sperm aster do not halt aster migration, indicating that pulling in this system is not essential to aster migration. Taken together, we conclude through this study that sperm aster migration in the sea urchin zygote is driven predominantly by a novel pushing mechanism.

Chapter III: Preliminary data. The impact of our pushing model necessitates revisions in our understanding of how MT asters grow and migrate with tightly regulated temporal and spatial precision to help organize large cells. The first important and perhaps equally fundamental question that our pushing model underscores is how aster size regulated. Because aster size, notably the radius of the rear portion of the sperm aster, dictates how far the aster migrates, determining how size is regulated will likely have direct implications on positioning of the sperm aster and its associated organelles within the cell. In biology cell sizes vary dramatically, and as such organelle sizes have been observed to adjust to cell size across different cell types through an occurrence called size scaling (West and Brown, 2005). While size scaling has been observed for various organelles such as the mitotic spindle and the nucleus (Good et al., 2013; Hazel et al., 2013; Lacroix et al., 2018; Mukherjee et al., 2020), this phenomenon has not been investigated in the context of interphase aster size. The sea urchin makes a powerful model organism to study size scaling due to the ability to accurately and precisely manipulate egg size, without requiring successive reductive divisions and the changes in developmental cues that accompany them. In our preliminary data, we take advantage of this feature and show that by decreasing the sizes of sea urchin eggs, sperm aster size also appears to decrease.

Furthermore, migration rates are notably slower, but because of the smaller sizes of the cells, asters find the cell center in approximately the same amount of time as control, fully-sized cells. Together, these data suggest that aster size, and thus migration rates, may be controlled by cell size.

Our second question is how can an aster spanning dozens to potentially hundreds of microns be pushed to accurate locations within a cell when pushing forces have been shown to be incapable of centration *in vitro* when astral MTs reach ~ 10 um due to MT buckling and slipping? We are not the first to hypothesize that bundling may reinforce MTs along their lengths sufficiently enough to prevent buckling (Reinsch and Gonczy, 1998). Furthermore, anchoring bundled MTs at the cortex may prevent slipping. An alternative hypothesis that simultaneously may prevent bundling and slipping in a pushing model is based on centrosome-independent MT nucleation during aster growth in the form of MT branching. In this model MT-dependent MT nucleation may result in more numerous and shorter MTs polymerizing against the cortex, which would conceptually redistribute pushing forces throughout a branched MT network rather than long individual MTs and prevent slipping/buckling. Importantly, these two hypotheses are not mutually exclusive. Rather, it may be a combination of branching and bundling during aster growth that leads to aster growth and positioning in large cells. In Chapter III we will present and discuss preliminary data in support of these models.

References

Albertson, D.G. (1984). Formation of the first cleavage spindle in nematode embryos. Dev. Biol. *101*, 61–72.

Alfaro-Aco, R., Thawani, A., and Petry, S. (2017). Structural analysis of the role of TPX2 in branching microtubule nucleation. J. Cell Biol. *216*, 983 LP – 997.

Alfaro-Aco, R., Thawani, A., and Petry, S. (2020). Biochemical reconstitution of branching microtubule nucleation. Elife *9*, e49797.

Bergen, L.G., Kuriyama, R., and Borisy, G.G. (1980). Polarity of microtubules nucleated by centrosomes and chromosomes of Chinese hamster ovary cells in vitro. J. Cell Biol. *84*, 151 LP – 159.

Bestor, T.H., and Schatten, G. (1981). Anti-tubulin immunofluorescence microscopy of microtubules present during the pronuclear movements of sea urchin fertilization. Dev. Biol. *88*, 80–91.

Bjerknes, M. (1986). Physical theory of the orientation of astral mitotic spindles. Science (80-.). *234*, 1413 LP – 1416.

Bonifacino, J.S., and Neefjes, J. (2017). Moving and positioning the endolysosomal system. Curr. Opin. Cell Biol. *47*, 1–8.

Chambers, E.L. (1939). The Movement of the Egg Nucleus in Relation to the Sperm Aster in the Echinoderm Egg. J. Exp. Biol. *16*, 409 LP – 424.

Dogterom, M., and Yurke, B. (1997). Measurement of the Force-Velocity Relation for Growing Microtubules. Science (80-.). *278*, 856–860.

Dogterom, M., Kerssemakers, J.W., Romet-Lemonne, G., and Janson, M.E. (2005). Force generation by dynamic microtubules. Curr. Opin. Cell Biol. *17*, 67–74.

Field, C.M., and Mitchison, T.J. (2018). Assembly of Spindles and Asters in Xenopus Egg Extracts. Cold Spring Harb. Protoc. .

Garzon-Coral, C., Fantana, H.A., and Howard, J. (2016). A force-generating machinery maintains the spindle at the cell center during mitosis. Science (80-.). *352*, 1124 LP – 1127.

Gönczy, P., Pichler, S., Kirkham, M., and Hyman, A.A. (1999). Cytoplasmic Dynein Is Required for Distinct Aspects of Mtoc Positioning, Including Centrosome Separation, in the One Cell Stage Caenorhabditis elegans Embryo. J. Cell Biol. *147*, 135 LP – 150.

Good, M.C., Vahey, M.D., Skandarajah, A., Fletcher, D.A., and Heald, R. (2013). Cytoplasmic Volume Modulates Spindle Size During Embryogenesis. Science (80-.). *342*, 856 LP – 860.

Hamaguchi, M.S., and Hiramoto, Y. (1980). Fertilization Process in the Heart-Urchin, Clypeaster Japonicus Observed with a Differential Interference Microscope. Dev. Growth Differ. *22*, 517–530.

Hamaguchi, M.S., and Hiramoto, Y. (1986). Analysis of the Role of Astral Rays in Pronuclear Migration in Sand Dollar Eggs by the Colcemid-UV Method. Dev. Growth Differ. *28*, 143–156.

Hamaguchi, Y., Toriyama, M., Sakai, H., and Hiramoto, Y. (1985). Distribution of fluorescently labeled tubulin injected into sand dollar eggs from fertilization through cleavage. J. Cell Biol. *100*, 1262–1272.

Hamill, D.R., Severson, A.F., Carter, J.C., and Bowerman, B. (2002). Centrosome Maturation and Mitotic Spindle Assembly in C. elegans Require SPD-5, a Protein with Multiple Coiled-Coil Domains. Dev. Cell *3*, 673–684.

Harris, P., Osborn, M., and Weber, K. (1980). Distribution of tubulin-containing structures in the egg of the sea urchin Strongylocentrotus purpuratus from fertilization through first cleavage. J. Cell Biol. *84*, 668 LP – 679.

Hazel, J., Krutkramelis, K., Mooney, P., Tomschik, M., Gerow, K., Oakey, J., and Gatlin, J.C. (2013). Changes in Cytoplasmic Volume Are Sufficient to Drive Spindle Scaling. Science (80-.). *342*, 853 LP – 856.

Holy, T.E., Dogterom, M., Yurke, B., and Leibler, S. (1997). Assembly and positioning of microtubule asters in microfabricated chambers. Proc. Natl. Acad. Sci. *94*, 6228 LP – 6231.

Ishihara, K., Nguyen, P.A., Groen, A.C., Field, C.M., and Mitchison, T.J. (2014). Microtubule

nucleation remote from centrosomes may explain how asters span large cells. Proc. Natl. Acad. Sci. *111*, 17715 LP – 17722.

Ishihara, K., Korolev, K.S., and Mitchison, T.J. (2016). Physical basis of large microtubule aster growth. Elife *5*.

Kemp, C.A., Kopish, K.R., Zipperlen, P., Ahringer, J., and O'Connell, K.F. (2004). Centrosome Maturation and Duplication in C. elegans Require the Coiled-Coil Protein SPD-2. Dev. Cell *6*, 511–523.

Kimura, A., and Onami, S. (2005). Computer Simulations and Image Processing Reveal Length-Dependent Pulling Force as the Primary Mechanism for C. elegans Male Pronuclear Migration. Dev. Cell *8*, 765–775.

Kimura, A., and Onami, S. (2007). Local cortical pulling-force repression switches centrosomal centration and posterior displacement in C. elegans . J. Cell Biol. *179*, 1347–1354.

Kimura, K., and Kimura, A. (2011). Intracellular organelles mediate cytoplasmic pulling force for centrosome centration in the Caenorhabditis elegans early embryo. Proc. Natl. Acad. Sci. *108*, 137 LP – 142.

King, M.R., and Petry, S. (2020). Phase separation of TPX2 enhances and spatially coordinates microtubule nucleation. Nat. Commun. *11*, 270.

Kozlowski, C., Srayko, M., and Nedelec, F. (2007). Cortical Microtubule Contacts Position the Spindle in C. elegans Embryos. Cell *129*, 499–510.

Laan, L., Pavin, N., Husson, J., Romet-Lemonne, G., van Duijn, M., López, M.P., Vale, R.D., Jülicher, F., Reck-Peterson, S.L., and Dogterom, M. (2012). Cortical Dynein Controls Microtubule Dynamics to Generate Pulling Forces that Position Microtubule Asters. Cell *148*, 502–514.

Lacroix, B., Letort, G., Pitayu, L., Sallé, J., Stefanutti, M., Maton, G., Ladouceur, A.-M., Canman, J.C., Maddox, P.S., Maddox, A.S., et al. (2018). Microtubule Dynamics Scale with Cell Size to Set Spindle Length and Assembly Timing. Dev. Cell *45*, 496-511.e6.

Lang, C.F., and Munro, E. (2017). The PAR proteins: from molecular circuits to dynamic self-stabilizing cell polarity. Development *144*, 3405 LP – 3416.

Malone, C.J., Misner, L., Le Bot, N., Tsai, M.-C., Campbell, J.M., Ahringer, J., and White, J.G. (2003). The C. elegans Hook Protein, ZYG-12, Mediates the Essential Attachment between the Centrosome and Nucleus. Cell *115*, 825–836.

McNally, F.J. (2013). Mechanisms of spindle positioning. J. Cell Biol. *200*, 131–140.

McNally, K.L., and McNally, F.J. (2005). Fertilization initiates the transition from anaphase I to metaphase II during female meiosis in C. elegans. Dev. Biol. *282*, 218–230.

McNally, K.L.P., Fabritius, A.S., Ellefson, M.L., Flynn, J.R., Milan, J.A., and McNally, F.J. (2012). Kinesin-1 Prevents Capture of the Oocyte Meiotic Spindle by the Sperm Aster. Dev. Cell *22*, 788–798.

Minc, N., Burgess, D., and Chang, F. (2011). Influence of Cell Geometry on Division-Plane Positioning. Cell *144*, 414–426.

Mitchison, T., and Kirschner, M. (1984). Dynamic instability of microtubule growth. Nature *312*, 237–242.

Mukherjee, R.N., Sallé, J., Dmitrieff, S., Nelson, K.M., Oakey, J., Minc, N., and Levy, D.L. (2020). The Perinuclear ER Scales Nuclear Size Independently of Cell Size in Early Embryos. Dev. Cell.

Murray, A.W., and Kirschner, M.W. (1989). Cyclin synthesis drives the early embryonic cell cycle. Nature *339*, 275–280.

Nguyen-Ngoc, T., Afshar, K., and Gönczy, P. (2007). Coupling of cortical dynein and Gα proteins mediates spindle positioning in Caenorhabditis elegans. Nat. Cell Biol. *9*, 1294.

Nishikata, T., Goto, T., Yagi, H., and Ishii, H. (2019). Massive cytoplasmic transport and microtubule organization in fertilized chordate eggs. Dev. Biol. *448*, 154–160.

Panzica, M.T., Marin, H.C., Reymann, A.-C., and McNally, F.J. (2017). F-actin prevents interaction between sperm DNA and the oocyte meiotic spindle in C. elegans. J. Cell Biol. *216*, 2273–2282.

Pelletier, L., O'Toole, E., Schwager, A., Hyman, A.A., and Müller-Reichert, T. (2006). Centriole assembly in Caenorhabditis elegans. Nature *444*, 619–623.

Peng, C.J., and Wikramanayake, A.H. (2013). Differential Regulation of Disheveled in a Novel Vegetal Cortical Domain in Sea Urchin Eggs and Embryos: Implications for the Localized Activation

of Canonical Wnt Signaling. PLoS One *8*, e80693.

Petry, S., Groen, A.C., Ishihara, K., Mitchison, T.J., and Vale, R.D. (2013). Branching Microtubule Nucleation in Xenopus Egg Extracts Mediated by Augmin and TPX2. Cell *152*, 768–777.

Pollard, T.D., and O'Shaughnessy, B. (2019). Molecular Mechanism of Cytokinesis. Annu. Rev. Biochem. *88*, null.

Rappaport, R. (1961). Experiments concerning the cleavage stimulus in sand dollar eggs. J. Exp. Zool. *148*, 81–89.

Reinsch, S., and Gonczy, P. (1998). Mechanisms of nuclear positioning. J. Cell Sci. *111*, 2283 LP – 2295.

Reinsch, S., and Karsenti, E. (1997a). Movement of nuclei along microtubules in Xenopus egg extracts. Curr. Biol. *7*, 211–214.

Reinsch, S., and Karsenti, E. (1997b). Movement of nuclei along microtubules in Xenopus egg extracts. Curr. Biol. *7*, 211–214.

Roossien, D.H., Miller, K.E., and Gallo, G. (2015). Ciliobrevins as tools for studying dynein motor function. Front. Cell. Neurosci. *9*, 252.

Rouvière, C., Houliston, E., Carré, D., Chang, P., and Sardet, C. (1994). Characteristics of pronuclear migration in Beroe ovata. Cell Motil. *29*, 301–311.

Roux, W. (1885). Die Entwickelungsmechanik der Organismen. Wien *8*.

Sallé, J., Xie, J., Ershov, D., Lacassin, M., Dmitrieff, S., and Minc, N. (2018). Asymmetric division through a reduction of microtubule centering forces. J. Cell Biol. jcb.201807102.

Schatten, G. (1981). Sperm incorporation, the pronuclear migrations, and their relation to the establishment of the first embryonic axis: Time-lapse video microscopy of the movements during fertilization of the sea urchin Lytechinus variegatus. Dev. Biol. *86*, 426–437.

Schatten, G. (1994). The Centrosome and Its Mode of Inheritance: The Reduction of the Centrosome during Gametogenesis and Its Restoration during Fertilization. Dev. Biol. *165*, 299–

335.

Sha, Q.-Q., Zhang, J., and Fan, H.-Y. (2019). A story of birth and death: mRNA translation and clearance at the onset of maternal-to-zygotic transition in mammals†. Biol. Reprod. *101*, 579–590.

Shinar, T., Mana, M., Piano, F., and Shelley, M.J. (2011). A model of cytoplasmically driven microtubule-based motion in the single-celled Caenorhabditis elegans embryo. Proc. Natl. Acad. Sci. *108*, 10508 LP – 10513.

De Simone, A., Spahr, A., Busso, C., and Gönczy, P. (2018). Uncovering the balance of forces driving microtubule aster migration in C. elegans zygotes. Nat. Commun. *9*, 938.
Song, J.-G., King, M.R., Zhang, R., Kadzik, R.S., Thawani, A., and Petry, S. (2018). Mechanism of how augmin directly targets the γ-tubulin ring complex to microtubules. J. Cell Biol. *217*, 2417 LP – 2428.

Srayko, M., Kaya, A., Stamford, J., and Hyman, A.A. (2005). Identification and Characterization of Factors Required for Microtubule Growth and Nucleation in the Early C. elegans Embryo. Dev. Cell *9*, 223–236.

Stewart-Savage, J., and Grey, R.D. (1982). The temporal and spatial relationships between cortical contraction, sperm trail formation, and pronuclear migration in fertilizedXenopus eggs. Wilhelm Roux's Arch. Dev. Biol. *191*, 241–245.

Tanimoto, H., Kimura, A., and Minc, N. (2016). Shape–motion relationships of centering microtubule asters. J. Cell Biol. *212*, 777 LP – 787.

Tanimoto, H., Sallé, J., Dodin, L., and Minc, N. (2018). Physical forces determining the persistency and centring precision of microtubule asters. Nat. Phys. *14*, 848–854.

Terasaki, M., and Jaffe, L. a (1991). Organization of the Sea-Urchin Egg Endoplasmic-Reticulum and Its Reorganization at Fertilization. J. Biophys. Biochem. Cytol. *114*, 929–940.

Thawani, A., Stone, H.A., Shaevitz, J.W., and Petry, S. (2019). Spatiotemporal organization of branched microtubule networks. Elife *8*, e43890.

West, G.B., and Brown, J.H. (2005). The origin of allometric scaling laws in biology from genomes to ecosystems: towards a quantitative unifying theory of biological structure and organization. J.

Exp. Biol. *208*, 1575 LP – 1592.

Wu, Y., and Griffin, E.E. (2017). Regulation of Cell Polarity by PAR-1/MARK Kinase. Curr. Top. Dev. Biol. *123*, 365–397.

Wühr, M., Tan, E.S., Parker, S.K., Detrich, H.W., and Mitchison, T.J. (2010). A Model for Cleavage Plane Determination in Early Amphibian and Fish Embryos. Curr. Biol. *20*, 2040–2045.

Zipperlen, P., Fraser, A.G., Kamath, R.S., Martinez-Campos, M., and Ahringer, J. (2001). Roles for 147 embryonic lethal genes on C.elegans chromosome I identified by RNA interference and video microscopy. EMBO J. *20*, 3984–3992.

Chapter 2. A Pushing Mechanism for Microtubule Aster Positioning in a Large Cell Type

Johnathan L. Meaders[1,2], Salvador N. de Matos[1], and David R. Burgess[1,2]

[1]Department of Biology, Boston College, Chestnut Hill, Massachusetts, USA

[2]Marine Biological Laboratory, Woods Hole, USA

Corresponding Author: David R. Burgess. Email: david.burgess@bc.edu

*This chapter is adapted from an article published in Cell Reports:

Meaders J.L., N. de Matos, S, Burgess, D.R. A Pushing Mechanism for Microtubule Aster Positioning in a Large Cell Type. *Cell Rep.* 33:1

Summary

Following fertilization, microtubule (MT) sperm asters undergo long-range migration to accurately position pronuclei. Due to the large sizes of zygotes, the forces driving aster migration are considered to be from pulling on the leading astral MTs by dynein, with no significant contribution from pushing forces. Here, we re-investigate the forces responsible for sperm aster centration in sea urchin zygotes. Our quantifications of aster geometry and MT density precludes a pulling mechanism. Manipulation of aster radial lengths and growth rates, combined with quantitative tracking of aster migration dynamics indicates that aster migration is equal to the length of rear aster radii, supporting a pushing model for centration. Additionally, we find that inhibition of dynein causes an increase in aster migration rates. Finally, ablation of rear astral MTs halts migration, while front and side ablations do not. Collectively, our data indicates that a pushing mechanism can drive migration of asters in a large cell type.

2.1 Introduction

Asters are radial arrays of microtubules (MTs) nucleated from microtubule organizing centers (MTOCs) such as the centrosome. Accurate positioning of asters is indispensable for central cellular functions during cell division and development. In the zygote, sperm asters nucleate from centrosomes anchored to the male pronucleus and serve a wide range of functions, including uniting the maternal and paternal DNA, providing the centrioles, accurate positioning of the pronuclei, and in some animals targeted delivery of organelles and information to precise locations in order to help establish later cell fate specification (Paix et al., 2011; Reinsch and Gonczy, 1998; Roegiers et al., 1999). Furthermore, during cell division in the embryo, mitotic asters help organize the spindle and deliver cortical signals to dictate the cleavage plane, which subsequently ensures correct partitioning of genetic material into daughter cells (Pollard and O'Shaughnessy, 2019; Rappaport, 1961). Despite its crucial importance to cellular development and function, there are still many gaps in our knowledge of the force balance required for accurate aster positioning.

Mathematical modeling and experimental evidence have supported opposing views for how asters find the correct position in cells of differing shapes and sizes. *In vivo* and *in vitro* evidence indicate that polymerization of MTs against the cell cortex can generate enough force to push their associated MTOCs to the correct position in small cells, such as *Schizosaccharomyces pombe* (Holy et al., 1997; Tran et al., 2001). However, in large cells where asters often span dozens to several hundreds of microns, pushing forces from MT polymerization against the cortex are thought to be lost due to MT buckling and slipping as MTs become longer (Bjerknes, 1986; Dogterom and Yurke, 1997; Dogterom

et al., 2005; Holy et al., 1997). Therefore, large cells such as sea urchin, frog, and *C. elegans* zygotes are widely thought to have adopted a pulling mechanism on astral MTs using the minus end-directed motor protein dynein anchored to the leading cortex (Laan et al., 2012; Nguyen-Ngoc et al., 2007; Saito et al., 2006) or cytoplasmic membranes (Barbosa et al., 2017; Gönczy et al., 1999; Kimura and Onami, 2005; Kimura and Kimura, 2011; Minc et al., 2011; De Simone et al., 2018; Tanimoto et al., 2016, 2018). In this pulling model, retrograde motility of cytoplasmic and/or cortical dynein along astral MTs generates pulling force in the opposite direction. While dynein-mediated cortical and/or cytoplasmic pulling mechanisms for aster positioning have been extensively studied, there is no evidence in support of a MT based pushing mechanism in large cell-types.

The sperm aster has long served as an instrumental *in vivo* model for studying the positioning of large asters in a cellular and developmental context, due to its long-range movements and opportunity for straightforward manipulation (Bestor and Schatten, 1981; Hamaguchi and Hiramoto, 1986; Harris et al., 1980). The theory that sperm nuclei cannot be pushed to the zygote center due to astral MT buckling and slipping was largely constructed around the radial elongation model for aster growth. In this model, the aster is composed of many long individual MTs that originate from the centrosome (Bergen et al., 1980). However, recent mounting evidence has changed our understanding of MT nucleation, revealing that MTs originate from locations remote from the centrosome in branched (Ishihara et al., 2014, 2016; Murata et al., 2005; Petry et al., 2013; Thawani et al., 2019; Verma and Maresca, 2019) or bundled forms (David et al., 2019). In this updated model for aster growth, pushing forces due to MT polymerization against the cortex may be redistributed among many shorter branched or reinforced bundled MTs, which would prevent buckling and slipping along the cortex. Thus, it is worth revisiting large aster positioning in consideration of the potential for MT polymerization based pushing forces.

Here, we have reanalyzed the question of pushing vs. pulling during aster positioning in a large cell type by using the sea urchin zygote, combined with quantitative fixed and live cell confocal imaging, global and local MT manipulation, and dynein inhibition. We find that aster geometry and MT density precludes a MT length-dependent and cortical pulling mechanism for aster centration. Chemical manipulation of astral MT lengths and growth rates, combined with quantitative tracking of aster migration dynamics indicates that aster migration is equal to and limited by the length of rear astral MTs but not correlated with the length of leading front astral MTs, providing further support for a pushing rather than a pulling model for sperm aster centration. We also find that rear astral MTs are anchored to the rear cortex, which would antagonize pulling from dynein along front astral MTs. Furthermore, inhibition of dynein causes an increase in aster migration, indicating that it likely represses centration forces rather than contributing to them. Finally, using a light inducible MT depolymerizing agent, we show that ablation of rear astral MTs halts aster migration, while front and side ablations of astral MTs do not. Collectively, our data indicates that a pushing mechanism can drive migration of asters in a large cell type.

2.2 Results

2.2.1 Sperm Aster Geometry and Density is Inconsistent with a MT Length-Dependent and Cortical Pulling Model

Forces may be exerted on the sperm aster from pulling by dynein in the cytoplasm or the cortex, or from pushing by MT polymerization against the cortex. According to a MT-length dependent cytoplasmic pulling model, the MTs in the front of the aster must be longer than those in the rear (Hamaguchi and Hiramoto, 1986; Kimura and Onami, 2005; Kimura and Kimura, 2011; Tanimoto et al., 2016). Such a length asymmetry is predicted to produce more dynein-dependent pulling forces along the front of the aster relative to the rear,

pulling the aster forward. Similarly, in a cortical pulling model the front of the aster is predicted to be longer than the rear because it must reach the far opposite cortex well before the aster begins moving. Conversely, if rear MTs are pushing the aster to the cell center, aster migration should be limited to the length of the rear portion of the aster and independent of the length of the front. To distinguish between these possible sites of force generation in the sea urchin zygote, we quantified aster geometry and densities using quantitative live-cell and immunofluorescence confocal microscopy during the aster migration phase, which lasts ~15-20 minutes until centration is complete.

We first performed confocal time-lapse microscopy of live zygotes co-injected with purified EB1-GFP protein to label growing MT plus-ends and purified Tau-mCherry protein, which labels MTs regardless of their dynamic state (Mooney et al., 2017). In order to define front, rear, top, and bottom portions of the aster, we performed our imaging using a specific cellular orientation. Cells were selected for imaging in which the sperm enters the egg at the equatorial plane (Figure S1A). Because the aster migrates in a straight line toward the cell center, deviations in the z-axis were not common. We imaged a z-plane across the MTOC, which is where the front and rear radius of the aster is the longest due to the spherical geometry of the aster (Figure S1A). Any portions of the aster extending up or down are “top” or “bottom” portions of the sperm aster exit our imaged z-plane and are excluded from the analysis. Using this orientation, we acquired a single image of Tau-mCherry, followed by a 30 second video of EB1-GFP at 2.5 seconds per frame at various time points post-fertilization (Figure 1A and Movie S1), which minimized photobleaching. Because the exact moment when fertilization occurs is difficult to distinguish, we used male pronuclear migration distance, detected by Hoescht staining, as a measure of time post fertilization. To this end, we acquired videos and images at time points when the male pronucleus had migrated 10, 15, 20, 25, 30, and 35 μm from the site of sperm entry. We

then converted EB1 movies to maximum intensity projections, allowing us to detect and quantify EB1 tracks. Last, to understand the geometry of the aster we measured the distance from the most distal portion of EB1-tracks to the MTOC in the front (toward the cell center) and rear (toward the point of sperm entry) portions of the aster, which allowed us to measure the maximum aster radius from the MTOC. The front radius of the aster was defined as an average of all tracks included in a ROI extending in front of the MTOC at a 45 degree angle relative to the direction of migration (Lfront). A similar 45 degree ROI extending between the MTOC and the rear cortex was used to define the rear radius of the aster (Lrear) (Figure 1A).

At early time points during migration, when the aster has moved only 10 and 15 um from the point of sperm entry, the average Lfront is not significantly longer than the average Lrear (Figure 1A-1B and Movie S1). By time the aster migrated 20-35 um from the site of sperm entry, Lrear becomes significantly longer than Lfront (Figure 1A-1B), which is inconsistent with a MT-length dependent cytoplasmic pulling model. To provide additional characterization of aster geometry we repeated a similar analysis (see Materials and Methods) on images of Tau-mCherry (Figure S1B-S1C and Movie S1). Similar to our EB1-GFP quantifications, we find that the average Lfront of the aster is not significantly different than Lrear during very early time points post-fertilization when the aster has only migrated 10-15 μm from the point of sperm entry (Figure S1B-S1C). However, the rear portions of the aster become significantly longer than front portions once the aster has migrated 20 μm or farther from the point of sperm entry (Figure S1B-S1C). Lastly, in order to obtain length data of the aster in 3D, we fertilized eggs and fixed them in suspension for immunofluorescence confocal microscopy at varying time points post-fertilization. We generated maximum intensity projections of z-stacks of the entire aster (Figure 1C), using

the same cellular orientation as in our live-cell analysis to ensure top and bottom portions of the aster do not bias our measurements (Figure S1A). Using our defined front and rear

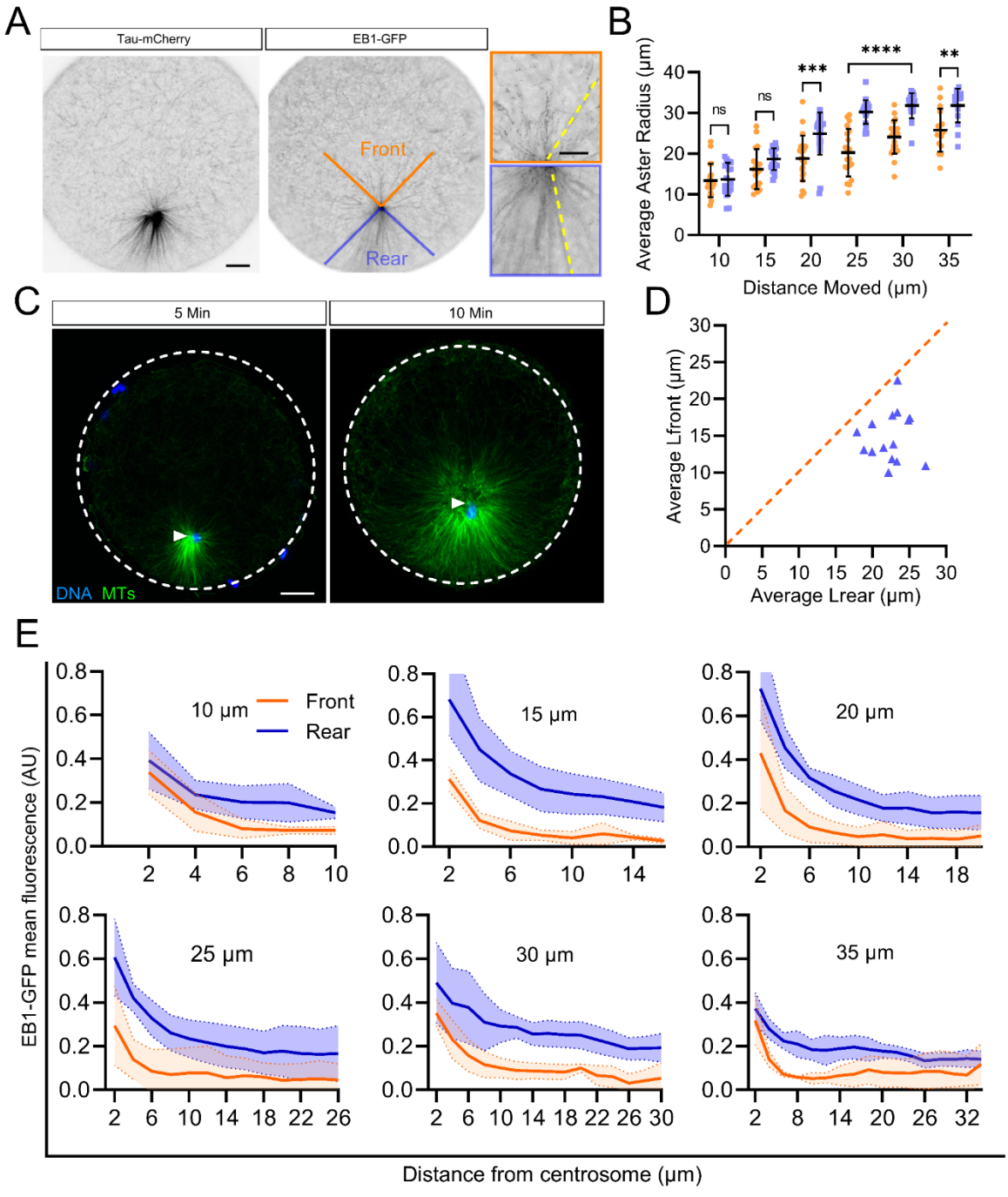

Figure 1. Rear Portions of the Sperm Aster are Longer and More Dense than Front Portions

(A) Live cell confocal microscopy of a zygote co-injected with Tau-mCherry and EB1-GFP. EB1-GFP was imaged for 30 seconds at 2.5 second intervals, followed by a single frame of Tau-mCherry (see also Movie S1). The imaging process was repeated at time points when the male pronucleus reached 10, 15, 20, 25, 30, and 35 μm from the site of sperm entry. The EB1-GFP channel shown is a maximum temporal projection of an aster that has moved 25 μm from the point of sperm entry, which yields quantifiable EB1-GFP tracks (insets) in defined front and rear portions of the aster (Figure S1A and Star Methods for more detailed definitions). Measurements of the most distal portion of the EB1-GFP tracks to the centrosomes (dashed yellow lines) were performed to obtain an average length of EB1-GFP tracks in front (orange outline), or cytoplasmic facing side of the aster (defined as Lfront/Front radius, top inset), and the rear, or cortical facing side of the aster (defined as Lrear/Rear radius, bottom inset, blue outlines). Scale bars, 10 μm

(B) Average maximum aster radius in defined front (Lfront) and rear (Lrear) portions of the aster as described in (A). Each orange circle is the average Lfront of each aster, and each blue square is the average Lrear of each aster (n=16 zygotes from 5 separate animals). ** P<.01, *** P<.001, ****P<.0001, 2-way ANOVA with Sidak's multiple comparisons. Data represented as mean, ± SD.

(C) Representative maximum intensity projections of immunofluorescence z-stacks at 5 and 10 minutes post-sperm addition. Sample orientation is the same as described in Figure S1A, in order to define front vs. rear aster radii. Arrow heads denote the MTOC. Scale bars, 10 μm

(D) Quantifications of the average maximum Lfront and Lrear of the sperm aster, imaged as in **(C)**. The dashed red line represents a symmetrical aster. n=15

(E) Quantifications of average EB1-GFP densities as a function of distance from the MTOC (2 μm intervals) in front and rear portions of the aster at the indicated migration distances. Intensity profiles were corrected for background and non-astral EB1-GFP signal and normalized to the fluorescence intensity of the MTOC (see Star Methods for additional info.) Shaded areas represent ± SD. P<.01, 2–way ANOVA with Sidak's multiple comparisons, n=9 zygotes.

See Figure S1 for imaging methods and length/density quantifications based on live Tau-mCherry signal

ROIs, we find that by ~5-10 minutes post-sperm addition the rear radius of the aster is longer than the front (Figure 1D).

Asymmetries in aster MT density could also account for a cytoplasmic pulling model. Similar to length asymmetries, a higher density of MTs within the front portion of the aster

than in the rear could allow more dynein-dependent pulling forces along the front relative to the rear. To quantify aster densities, we performed average intensity projections of our EB1-GFP time frames producing an average EB1 density map of the sperm aster. We used these projections to quantify mean EB1-GFP fluorescence at 2 um intervals extending from the centrosome to the aster periphery using the same front and rear 45 degree ROIs used in our aster length quantifications. We observe a sharp decrease in mean EB1-GFP intensity between ~2-6 μm from the centrosome (Figure 1E). However, beyond ~6 μm the aster density becomes constant throughout the extent of the aster in both front and rear portions (Figure 1E). Furthermore, during all time points after fertilization and at all distances from the centrosome, we find the rear

portion of the aster to be more dense than the front (Figure 1E). To further quantify aster densities, we repeated the same analysis on our images of Tau-mCherry acquired from the same cells, which produces results comparable to EB1-GFP intensity profiles (Figure S1D). Finally, we performed structured illumination microscopy (SIM) to gain higher resolution of the density asymmetries of fixed sperm asters. Consistent with fixed confocal and live cell imaging, these super resolution images allow us to qualitatively observe a much higher density in rear portions of the sperm aster relative to the front (Figure S1E). Hence, the rear radius of the aster is longer and contains more MTs than the front during the rapid migration phase (see below), which is inconsistent with a MT-length dependent cytoplasmic pulling model for aster migration.

2.2.2 Sperm Aster Migration Rates Are Equal to Growth Rates of the Rear Portion of the Aster

We next sought to determine if sperm aster migration distance and/or rates are limited to lengths and growth rates of Lrear. According to the MT length-dependent cytoplasmic pulling model the formula L_{front} - L_{rear} was proposed to dictate migration rates, which is

thought to account for a constant maximum migration rate regardless of aster size (Tanimoto et al., 2016). Consequently, if aster size is proportionately increased or decreased, aster migration rates should stay the same. Conversely in a pushing model, aster migration rates will be strictly limited to growth rates of Lrear. To test these hypotheses, we treated cells with urethane (ethyl carbamate) or hexylene glycol (HG) to shorten or lengthen asters, respectively. Urethane was previously shown to shorten astral MTs within the mitotic aster by increasing MT catastrophe (Rappaport and Rappaport, 1984; Strickland et al., 2005), while HG increased MT growth rates by decreasing MT catastrophe (Strickland et al., 2005). We found in both live and fixed cells, urethane and HG pretreatment decreased or increased sperm aster diameter, respectively (Figure 2A-2B and S2A).

We next measured aster migration rates in urethane, HG, and DMSO (control) treated zygotes by two methods (Figure 2C and S2B). In the first method, which is similar to previous studies (Tanimoto et al., 2016), we labeled male and female gamete DNA with Hoechst and tracked male pronuclear movement as a readout for aster migration. Second, to directly detect and track the aster itself, we injected EB1-GFP and tracked aster MTOCs at 5, 10, and 15-minute time points after sperm addition, which also allowed us to compare migration rates with growth rates of Lfront and Lrear. In control zygotes, we find that both methods yield migration rates that are highly consistent with each other, indicating that EB1-GFP injections do not affect aster migration (Figure S2B). Additionally, both methods yield migration rates that are consistent with the three phases of sperm aster migration described by previous studies (Chambers, 1939; Schatten, 1981; Tanimoto et al., 2016) (Figure S2B and Movie S2). The first is a slow penetration phase just after sperm entry (2.29 +/-.09 μm/min). The second is the migration phase in which the aster moves the

majority of the distance to the cell center and reaches a constant maximum velocity (4.8 +/- .2 μm/min). The third is a slow-down phase as the aster nears the cell center and the

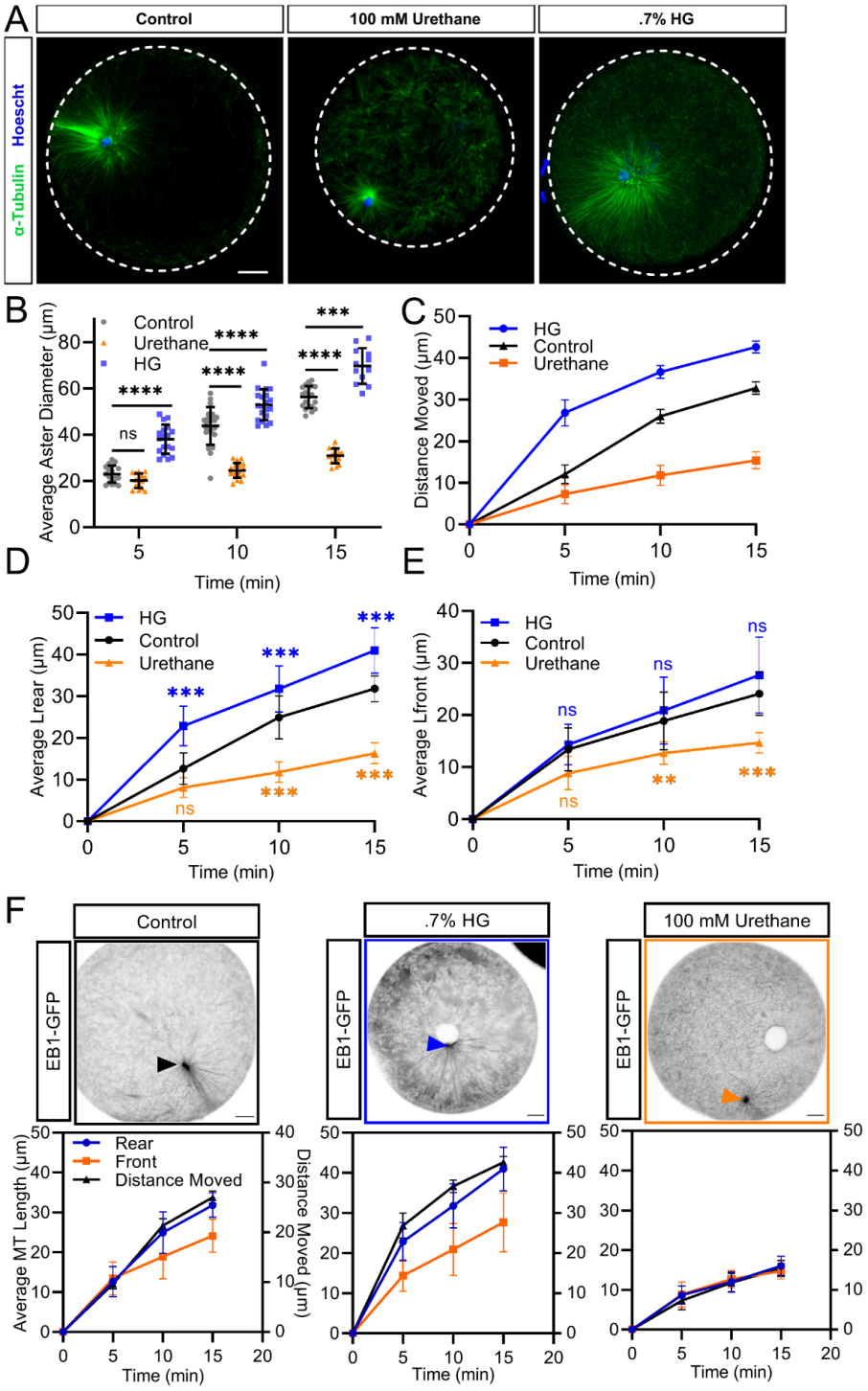

Figure 2. Sperm Aster Migration Rates Scale with Lrear, but not Lfront Growth Rates

(A) Representative maximum intensity projections of fixed immunofluorescence z-stacks of sperm asters in zygotes treated with Urethane to decrease aster size and Hexylene Glycol (HG) to increase aster size. Asters shown are from zygotes fixed 10 minutes post-sperm addition. Scale bars, 10 μm

(B) Quantifications of aster diameters determined by EB1-GFP signal in live embryos imaged for 30 seconds every 2.5 seconds at 5, 10, and 15 minutes post-sperm addition (see also Movie S2). Changes in diameter are consistent with quantifications of fixed immunofluorescence z-stacks represented in (A) (See Figure S2A for quantifications). ***P<.001, ****P<.0001, ns not significant, 2-way ANOVA with Turkey's multiple comparison test. Data represent mean diameter from 10+ zygotes, error bars ± SD.

(C) Quantifications of average distance moved plotted as a function of time post-sperm addition based on the distance of the MTOC, detected by EB1-GFP signal (see Movie S2), from the site of sperm entry at the indicated time points (see Figures S2B-S2C for further quantifications of aster migration speeds). The aster increases migration rate in HG-treated zygotes and comes to an early stop in urethane-treated zygotes. Lines represent the mean distance moved (n=8+ zygotes) and error bars ± SD.

(D) and (E) Lfront and Lrear measured by EB1-GFP maximum intensity temporal projections quantified the same as in Figure 1B at 5, 10, and 15 minute time points post-sperm addition. 10 minute projections are represented by the images shown in (F). Note that Lrear in HG-treated zygotes expands sooner compared to Lrear of controls (D). However, Lfront in HG-treated zygotes does not grow faster than controls (E). ** P<.01, *** P<.001, **** P<.0001 ns, not significant, 2-way ANOVA with Tukey's multiple comparisons. Lines represent mean Lrear or Lfront calculated from 8+ zygotes from 3 different animals. Error bars ± SD.

(F) Comparison of Lfront and Lrear calculated in (D) and (E) with the migration rates calculated in (C), across control, HG, and urethane-treated zygotes. Distance moved scales with Lrear, but not Lfront in control and HG-treated conditions. In urethane-treated conditions, aster expansion never occurs, and sperm asters never reach the cell center. P>.05 (ns) comparing distance moved vs. Lrear at all time points in all 3 conditions. P<.001 (*** highly significant) comparing distance moved vs. Lfront at 10 and 15 minute time points post-fertilization in control and HG-treated asters. 2-way ANOVA with Tukey's multiple comparisons. Lines are mean from 8+ zygotes, error bars, ± SD. Scale bars, 10 μm. See also Figure S2C and Movie S2.

MTOC becomes bipolar (1.250 +/- .25 μm/min). In a pushing model we predict that the observed changes in migration rates should scale with changes solely in growth rates of Lrear. To test this hypothesis, we performed a regression analysis comparing changes in average Lfront and Lrear growth rates with changes in average migration rates throughout the three phases of migration in control zygotes (Figure S2C). We find that growth rates of Lrear and migration rates strongly fit a logistic growth curve (R^2=.80 and .98 respectively, P<.001, comparisons of fit test) (Figure S2C). Conversely, growth rates of Lfront weakly fit a logistic growth curve, (R^2=.51, P>.05), instead better fitting a linear growth model (Figure S2C). That is, during the first slow phase of aster migration, Lrear is growing slowly and matches growth rates of Lfront (Figures 1B, S2B and S2C), which explains the equal average Lfront and Lrear we observe (Figure 1B). During the second phase, aster migration rates and Lrear growth rates accelerate to a maximum (Figures S2B and

S2C). Finally, when the aster slows down during the third and final stage of migration, Lrear growth rates also decrease as centrosomes separate forming bipolar asters on each side of the centered male/female pronuclear complex. Conversely, Lfront grows in a slow, more linear fashion, regardless of the phase of aster migration, providing support that migration rates scale specifically with Lrear growth rates (Figure S2C).

In HG-treated zygotes, we find a striking increase in aster migration rates relative to controls (Figure 2C and Movie S2). Importantly, asters in HG-treated zygotes display increased growth rates of Lrear, but not Lfront relative to controls (Figures 2D and 2E), further confirming that increases in migration rates are dictated solely by growth rates of rear MTs. Furthermore, migration rates closely match growth rates of only Lrear (not Lfront) in both control and HG-treated zygotes (Figure 2F). Conversely, in urethane-treated zygotes the aster is arrested in the first phase of migration in which expansion of

Lrear never occurs resulting in equal Lfront and Lrear (Figures 2C-2F), and asters never accelerate toward the zygote center (Figures 2C, 2F, and Movie S2). Collectively these data strongly support a pushing model in which aster migration rates are exclusively controlled by growth rates of Lrear rather than a pulling model in which migration rates are dictated by the equation $L_{front} - L_{rear}$.

2.2.3 The Sperm Aster is Anchored to the Rear Cortex

We next aimed to determine whether or not rear astral MTs are also anchored to the rear cortex, which would highlight two key points. The first is that anchoring to the rear cortex should antagonize any potential pulling forces during aster centration. The second is that anchoring of MTs has been shown to prevent MT slipping as polymerization-induced pushing forces are generated by MTs growing against a surface (Pavin et al., 2012). To explore this question, we utilized a cortical isolation method commonly used to identify the actin cortex and its interactions with developmental determinants (Burgess and Schroeder, 1977; Henson et al., 2019; Peng and Wikramanayake, 2013). Cortical isolations were prepared ~5 minutes post sperm addition, before side and front portions of the aster interact with the cortex (Figure 1C), which means any potential interactions between the aster and the cortex are exclusively in the rear. In this experiment, we hypothesized that if the aster is not anchored to the actin cortex it will be washed away with the rest of the zygote cytoplasm during the cortical isolation procedure. Instead, we find full asters including male pronuclei remaining in the cortical preparations, (Figure 3A), indicating that the sperm aster is anchored to the rear cortex

2.2.4 Retrograde Female Pronuclear Transport Exerts Pulling Forces that are not Essential for Sperm Aster Centration

In other systems, plasma membrane (PM) indentations or invaginations have been used as a readout for pulling forces on MTs physically coupled to the cell cortex (Negishi et al., 2016; Redemann et al., 2010; Yi et al., 2013). Therefore, we hypothesize that any existing pulling forces on the cortically anchored sperm aster may result in plasma membrane invaginations. However, there are two major caveats to detecting potential PM invaginations in our system. The first is that the aster, most notably the rear portion, is rapidly growing during aster migration when potential cytoplasmic pulling forces may be present, which would counteract invaginations of the PM due to pulling from the front portion of the aster. Secondly, by the time the sperm aster comes to a stop near the zygote center, pronuclear fusion and centrosome separation has usually already occurred resulting in bipolar asters, which are characterized by their own pulling forces to center the zygote nucleus (Minc et al., 2011). To overcome both of these challenges we designed an experiment in which the sperm aster approaches the zygote center and halts migration well before engagement, transport, and fusion of the female pronucleus is complete. Unfertilized eggs were centrifuged resulting in the female pronucleus floating to the centripetal pole (Harvey, 1933). We then fertilized eggs and selected those in which the sperm entry point was at the opposite pole from the female pronucleus for quantitative imaging (Movie S3). In fixed samples, sperm aster size and morphology of centrifuged eggs is comparable to non-centrifuged eggs indicating that centrifugation does not affect aster growth (Figure 3D and Figures S3A-S3C). In live centrifuged cells, we find that male and female pronuclear migration occurs in three separate phases (Figures 3B-3C and Movie S3). During the first ~6 minutes after fertilization, the male pronucleus migrates toward the zygote center in the absence of female pronuclear movement/engagement. Between ~6-12 minutes post-fertilization, the sperm aster captures the female pronucleus and both pronuclei moved at approximately the same rate toward each other. Finally, during the third phase the male pronucleus comes to a stop near the zygote center, while

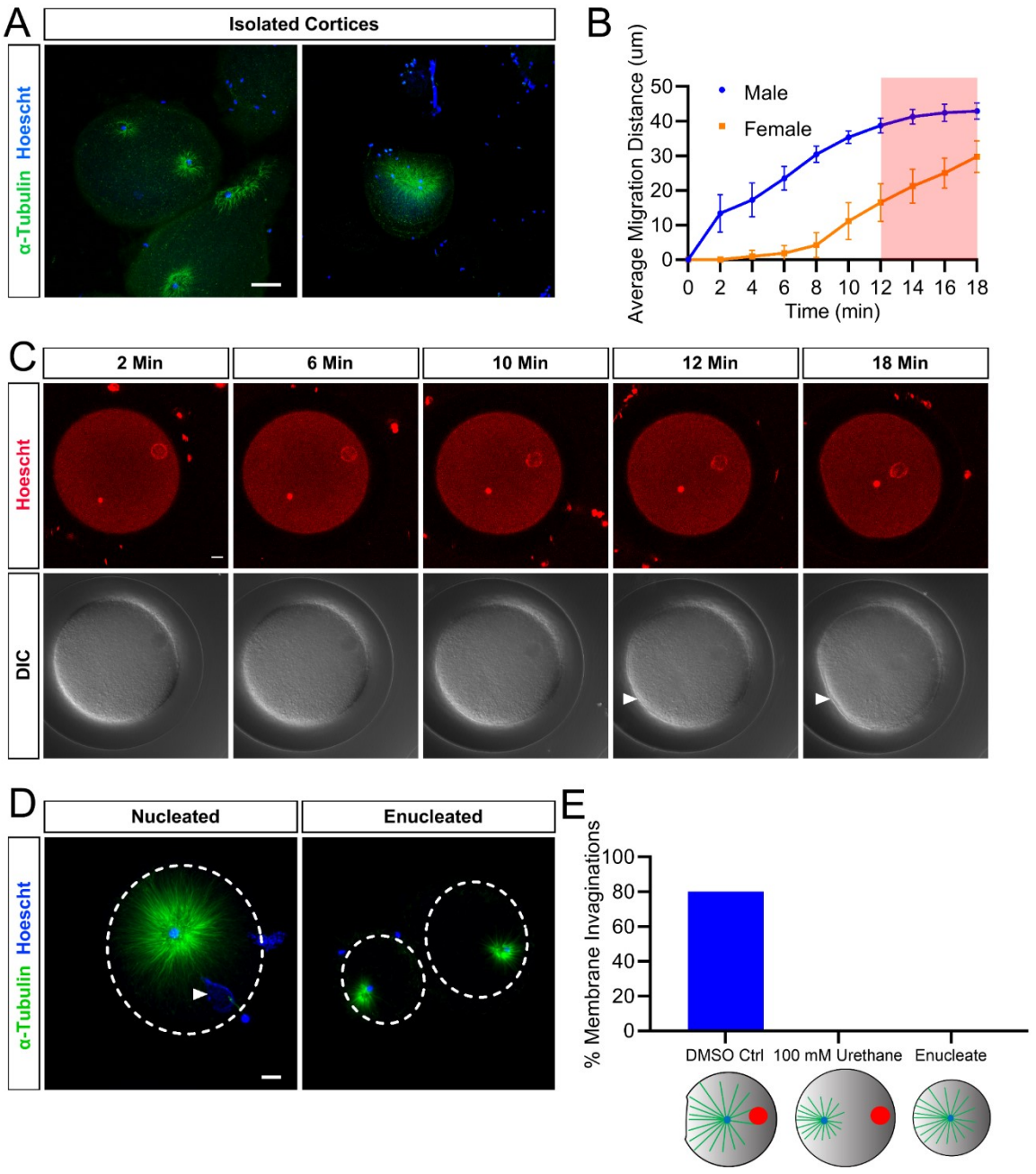

Figure 3. The sperm aster is anchored to the rear cortex

(A) Representative immunofluorescence maximum intensity projections of cortical isolations containing anchored sperm asters. Cortical isolations were fixed and prepared for IF at ~10 minutes post-fertilzation. Max projections are ~10 µm think in z. Scale bars, 10 µm

(B) and (C) Live maximum intensity projections and quantification of pronuclear migration dynamics in eggs centrifuged pre-fertilization, which floats the female pronucleus to the cell periphery. Sperm

entry in these samples is directly opposite of the female pronucleus. The red region (B) at 12-18 minutes post sperm-addition indicates when the female pronucleus is being transported along an immobile aster/male pronucleus. Arrow head in (C) annotates rear plasma membrane invaginations on the side of sperm entry during the same time points. See also Movie S3. Lines in (B) represent average distance moved at the indicated time point post-fertilization. Error bars, ± SD, n=12+ zygotes. Scale bar, 10 μm

(D) Fixed immunofluorescence 3D projections of sperm asters in centrifuged zygotes. Centrifuging the eggs longer causes them to split, resulting in nucleated and enucleated halves. Arrow head marks the female pronucleus in a nucleated zygote. Scale bar, 10 μm

(E) Quantification of zygote rear cortical invaginations as detected in (B) and (C) at 12-18 minutes post-fertilization. See also Movie S3. Schematics illustrate possible pulling forces to generate rear membrane invaginations: DMSO Ctrls-pulling from the female pronucleus (red circle) and/or cytoplasmic MT length-dependent factors. 100 mM urethane-cytoplasmic MT length-dependent factors. Enucleated zygotes-cytoplasmic MT length dependent factosr. Note that sperm asters also center in the absence of the female pronucleus (n=10+ per condition)

the female pronucleus completes its final migration (Figure 3B-3C and Movie S3). During the third phase, the female pronucleus is transported along a stationary aster, which should allow us to detect potential pulling forces. Consistent with this, between ~12-18 minutes post-fertilization, when engagement between the stationary aster and female pronucleus occurs, the rear membrane displays a dramatic invagination as the female pronucleus completes its final migration along the stationary sperm aster (Figures 3C and 3E and Movie S3). This result further confirms that the sperm aster is anchored to the rear cortex and suggests that pulling forces are present between the male and female pronucleus upon engagement (Figure 3C and Movie S3).

The PM invaginations we observe during the last phase of female pronuclear movement could be due to pulling forces from retrograde transport of the female pronucleus, MT-length dependent cytoplasmic forces, or a combination of both. To distinguish between these possibilities, we repeated the centrifugation experiments in a urethane-treated

condition, which results in stationary short asters unable to interact with or capture the female pronucleus (Movie S3). We hypothesize that if MT-length dependent cytoplasmic forces are significant, we should observe PM invaginations in the absence of aster/female pronuclear engagement. In this condition there are no observable PM invaginations (Figure 3E and Movie S3), suggesting that MT-length dependent cytoplasmic pulling does not substantially contribute the pulling forces required to cause PM invaginations, and the invaginations observed in control centrifuged eggs are instead due to pulling by retrograde transport of the female pronucleus.

To further investigate this point, we tested pulling forces in the complete absence of the female pronucleus, enabling us to directly determine if pulling forces other than those from engagement between the male and female pronuclei contribute to the dimpling we observe. To this end, we centrifuged eggs slightly longer and at a higher speed to split them into two cells, resulting in nucleated and enucleated halves. Both halves can be fertilized and develop to the pluteus larval stage (Harvey, 1933). When we fertilized enucleated halves, we observe smaller asters that display a front:rear aspect ratio comparable to full-sized cells. This indicates that while smaller enucleuated eggs results in smaller asters, the shape of these smaller asters are not affected (Figures) S3A-S3B. More importantly, enucleated halves display normal sperm aster centration (Figures S3A and Movie S3C) confirming that potential pulling forces from the female pronucleus are non-essential to aster migration (Figure 3D and Movie S3C). Furthermore, in centered, stationary asters of enucleated zygotes, we do not observe any membrane invaginations, indicating that the engagement between the male and female pronuclei provides the pulling force seen in nucleated eggs (Figures 3D-3E and Movie S3). We conclude that retrograde transport of the female pronucleus generates substantial pulling forces on the sperm aster, which are non-essential for the majority of sperm aster migration as the aster

centers normally in enucleated eggs. Moreover, there is no detectable contribution of MT length-dependent cytoplasmic pulling forces to these indentations.

2.2.5 Inhibition of Dynein-Dependent Retrograde Transport Results in Faster Aster Migration Rates

The lack of essential cytoplasmic pulling forces detected in this system prompted us to revisit the requirement for dynein during aster positioning. The cytoplasmic dynein inhibitor ciliobrevin was previously used to purportedly stop dynein activity and male pronuclear migration (as a readout for aster migration) in sea urchins, an experiment integral to the MT-length dependent cytoplasmic pulling model (Tanimoto et al., 2016). However, cytoplasmic dynein has been strongly implicated in focusing of MTs to centrosomes (Goshima et al., 2005; Merdes et al., 2000). Additionally, ciliobrevins have been shown to inhibit spindle pole focusing (Firestone et al., 2012). Because the specificity of ciliobrevin, a general AAA ATPase inhibitor, for dynein is also in question (Roossien et al., 2015), we carefully analyzed the effects of ciliobrevin on sperm asters. We observed sperm aster integrity using live and fixed-cell immunoflourescnce microscopy in ciliobrevin-treated zygotes. Ciliobrevin was added to cells 5 minutes post-fertilization in order to ensure there is sufficient time for the aster to expand. We used 100 μM and 50 μM, which were the concentrations previously used to purportedly inhibit aster migration in sea urchins (Tanimoto et al., 2016, 2018). By immunofluorescence, we find that a 5 minute treatment with 100 μM of ciliobrevin completely abolishes asters (Figure 4A). At 50 μM ciliobrevin aster MTs were almost completely disassembled (Figure 4A). Following MTs in live cells with injected Tau-mCherry, disruption of aster morphology becomes apparent at ~125 seconds after ciliobrevin addition (Figure 4B, and Movie S4A). These cells display signs of MT disassembly in both rear and front portions of the aster, followed by complete disintegration of the aster by 10 minutes. These data indicate that the previously reported

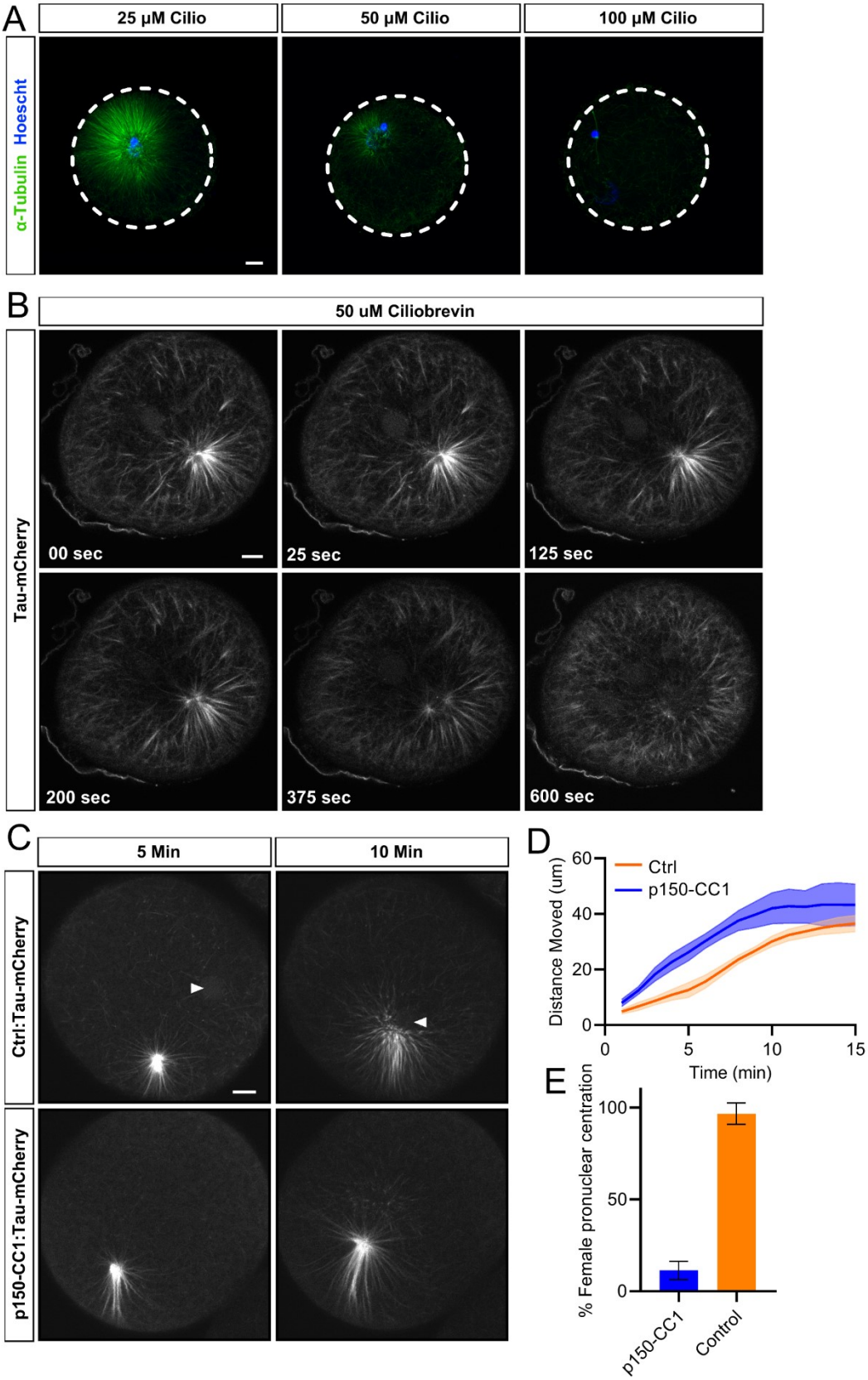
A
25 µM Cilio
50 µM Cilio
100 µM Cilio
α-Tubulin Hoescht
B
50 uM Ciliobrevin
Tau-mCherry
00 sec
25 sec
125 sec
200 sec
375 sec
600 sec
C
5 Min
10 Min
Ctrl:Tau-mCherry
p150-CC1:Tau-mCherry
D
Ctrl
p150-CC1
Distance Moved (um)
60
40
20
0
0
5
10
15
Time (min)
E
% Female pronuclear centration
100
50
0
p150-CC1
Control

Figure 4. Dynein inhibition with p150-CC1 prevents capture/transport of the female pronucleus and increases aster migration rates

(A) Representative immunofluorescence maximum intensity projections of sperm asters in zygotes treated with different concentrations of the dynein inhibitor, ciliobrevin D. Zygotes were treated at ~5 minutes post sperm-addition, and fixed 5 minutes later Scale bar, 10 μm

(B) Live-cell confocal time-series of sperm asters labeled with Tau-mCherry and treated with 50 μM of ciliobrevin. Drug was added at time point 0. See also Movie S4A. Scale bar, 10 μm

(C) Live-cell confocal images of cells injected with only Tau-mCherry or coinjected with Tau-mCherry and p150-CC1 to inhibit dynein. See also Movie S4B. Arrow head marks the female pronucleus in controls. Scale bar, 10 μm

(D) Quantifications of aster migration distance as a function of time post-fertilization from videos acquired in (C). Aster migration was tracked by following the distances of the centrosome from the site of sperm entry at 10-15 second intervals. Solid lines represent the average distance moved in each condition, shaded areas represent ± SD (n=11 zygotes per condition). Distance moved is significantly different between conditions from 1-9 minutes ($P<.05$). 9-15 minutes is not significantly different, 2-way ANOVA with Sidak's multiple comparisons.

(E) Average percentage of zygotes in which the female pronucleus undergoes retrograde transport along the sperm aster to the cell center in p150-CC1-injected and control zygotes imaged as in (C). n=11 zygotes per condition from 3 separate animals, Error bars, ± SD

halt in male pronuclear migration seen after ciliobrevin treatment (Tanimoto et al., 2016) may not be due to inhibiting dynein-dependent MT-length dependent cytoplasmic pulling forces along the associated aster. Instead, the observed halt of the male pronucleus may be because there is no longer an aster to provide centration forces.

To more directly assess the requirement of dynein during aster migration in sea urchin zygotes, we employed a more specific method to inhibit dynein. To this end, we co-injected eggs with Tau-mCherry and the p150-CC1 fragment, which functions through dominant-negative disruption of the dynactin/dynein interaction to inhibit cytoplasmic dynein (Quintyne et al., 1999). Surprisingly, we find that sperm asters in p150-CC1 injected

zygotes migrate to the cell center at faster rates compared to controls injected only with Tau-mCherry (Figures 4C-4D and Movie S4B). We also find that in some cases, asters begin rotating in the egg revealing spiral shapes as they near the cell center (Movie S4B), suggesting that asters may have lost cortical attachment.

To determine if the level of dynein disruption is sufficient to stop retrograde transport in p150-CC1 injected eggs, we quantified the percentage of microinjected zygotes in which the female pronucleus reaches the cell center, which is likely due to dynein-dependent transport along the sperm aster as shown in other systems (Reinsch and Karsenti, 1997). We find that only 11.3% of p150-CC1 injected zygotes contain centrally located female pronuclei, while 96% of controls contain centrally located nuclei 20 minutes after sperm addition (Figures 4C and 4E and Movie S4B), indicating that cytoplasmic dynein is sufficiently disrupted to prevent retrograde cytoplasmic transport of the female pronucleus along astral MTs. Finally, because p150-CC1 injections were performed before fertilization, dynein is inhibited at each of the three stages of sperm aster migration, indicating that that pulling forces from dynein-dependent retrograde transport is not essential for any stage of aster migration. Taken together, we conclude that while dynein activity is required for engagement and retrograde transport of the female pronucleus along the sperm aster, it may instead function antagonistically to centration forces acting on the sperm aster, as indicated by increased migration rates in the presence of p150-CC1.

2.2.6 The Sperm Aster is Pushed to the Zygote Center by Rear MTs

So far our data indicates that the sperm aster is pushed to the cell center by expansion of the rear portion of the aster. Additionally, while we observe pulling forces along the front of the aster, they appear to be primarily attributed to capture/retrograde transport of the

female pronuclues toward the male pronucleus at late stages of karyogamy, and they are not essential for any of the three phases of sperm aster migration. As a final, more direct approach to testing the contribution of pushing vs. pulling forces during aster centration, we sought to ablate the rear portion of the aster and directly follow aster migration dynamics using the Tau-mCherry MT label (Mooney et al., 2017). A long-standing hypothesis proposes that ablation of rear astral MTs will stop aster migration if pushing is predominant (Reinsch and Gonczy, 1998). Conversely, if aster migration is driven by pulling forces that scale with the length of front MTs, rear ablation should increase migration rates by increasing Lfront relative to Lrear (Reinsch and Gonczy, 1998). Laser ablation of the rear astral MTs is not feasible because it purportedly disrupts the rear cell membrane in the sea urchin zygote (Tanimoto and Minc, 2017). Therefore, we instead employed targeted chemical ablation of MTs with the light inducible MT depolymerizing compound, caged-combretastatin 4A (CA4) (Costache et al., 2017; Wühr et al., 2010). We activated a low dose of CA4 between ~4-8 minutes post sperm addition in a rectangular region of the rear sperm aster, proximal to the rear cortex (Figure 5A and Movie S5A). We observe depolymerization of the dense rear MTs near the cortex after the UV pulse (Figures 5A and 5B and Movie S5A). Sperm aster migration comes to a complete stop almost immediately after rear UV-activation, well before it reaches the zygote center (Figures 5A-5C and Movie S5A). Conversely, ablation of front or side portions of the aster does not halt aster migration (Figure 5C and Movie S5B). However, side ablations do cause the sperm aster to drift away from the side of ablation, which suggests a role in guiding the aster (Movie 5SB). Before UV uncaging, aster migration rates in CA4-treated zygotes are ~4.8 um/min, which is comparable to aster migration rates in untreated zygotes (Figure S2A and Figure 5C), indicating that the caged compound is not affecting aster migration in unintended ways. Additionally, cells treated with CA4 without UV activation display normal spindles and equatorial division, further controlling for

unintended effects of CA4 on MT organization (Figures 5D and 5E). Together, these data provide direct support that pushing from rear MT growth drives sperm aster migration, while ruling out any significant contribution from cytoplasmic pulling forces that scale with MT length.

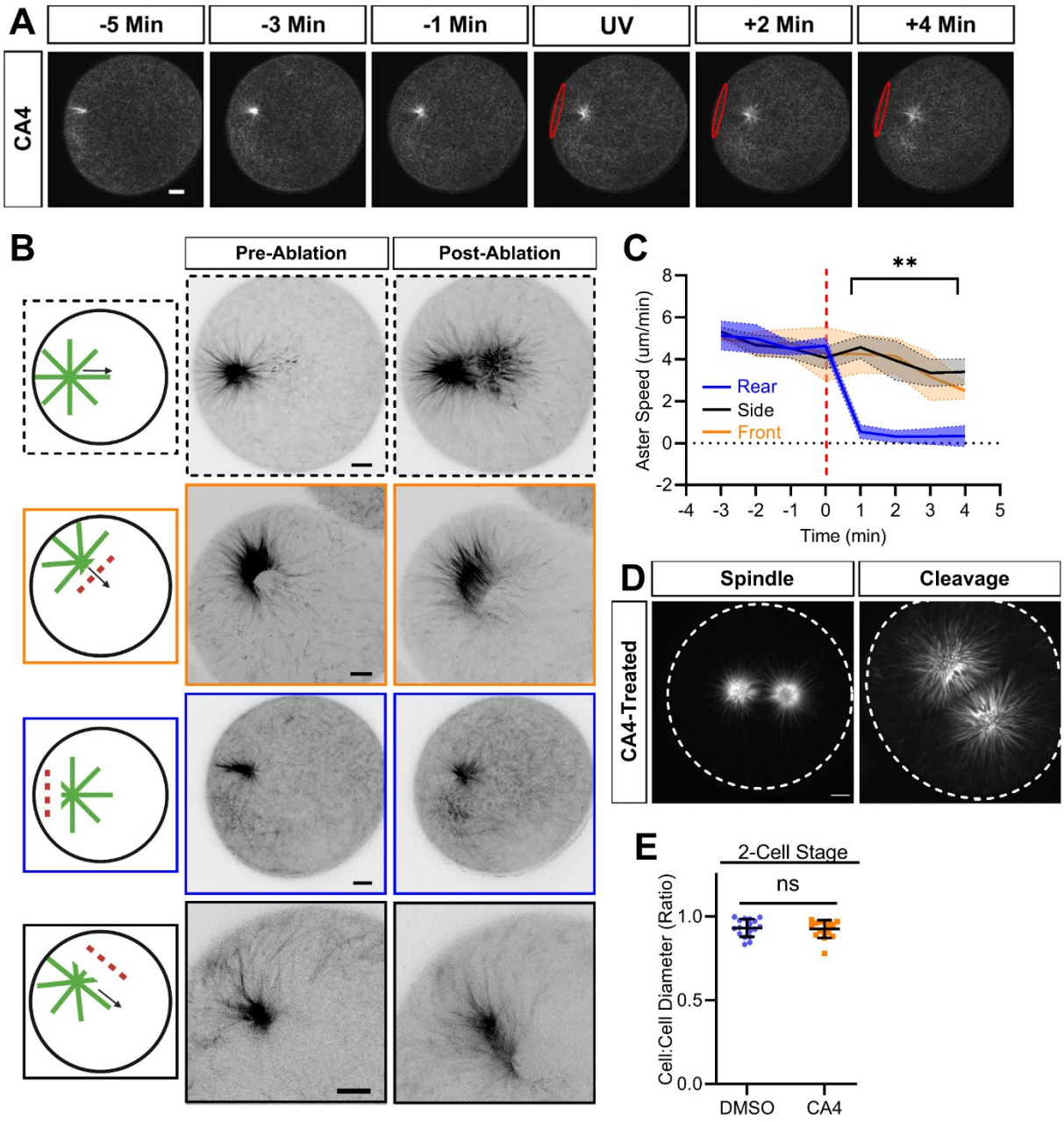

Figure 5. The sperm aster is pushed to the zygote center by rear astral MTs

(A) Confocal time-lapse images of Tau-mCherry injected zygotes treated with the light inducible MT inhibitor CA4. A region of the rear astral MTs were irradiated with UV light (outlined in red). Scale bars, 10 μm

(B) Maximum temporal projections of non-ablated (top panel), front-ablated (second panel), rear ablated (thrid panel), and side ablated (bottom panel) before and after activation of CA4. The approximate regions of UV activation are indicated in the left illustrations. Grayscale LUTs were inverted to more easily detect aster mass loss. See also Movies S5A and S5B. Scale bar,10 μm.

(C) Quantifications of average aster speed as a function of time before and after ablation of rear, side and front portions of the sperm aster. The red dashed line indicates the ablation time point. See also Movies S5A and S5B. Solid lines represent the mean, shaded regions represent ± SD (n=6 per condition). ** P<.001 comparing Rear vs. Side and Rear vs. Front, 2-way ANOVA with Sidak's multiple comparisons test.

(D) Live-cell images of spindle formation and cleavage in Tau-mCherry-injected embryos treated with CA4. Without UV activation of CA4, cells form robust spindles, which proceed to equatorial cleavage. The future cleavage plane can be determined by the mid-zone between anaphase asters where tubulin signal is not present.

(E) Quantification of cell diameter in the 2-cell embryo, after cleavage has completed. The cell:cell ratio is the diameter ratio of each of the two cells. Note in both conditions, the ratio very close to 1.0 indicating that each of the two cells are approximately equal diameter as a result of equatorial division. P<.7336 (ns), Unpaired t-test. Error bars represent SD (n=17 per condition).

2.3 Discussion

Correct positioning of MT asters is vital to cellular development and function. Hence, the nature of the force mechanism responsible for MT aster positioning represents an important question in developmental and cellular biology. Elaborate studies of large mitotic asters in zebrafish and *C. elegans* embryos have elucidated cortical and cytoplasmic dynein-dependent pulling mechanisms (Kozlowski et al., 2007; Wühr et al., 2010). However, *in vivo* studies of sperm aster migration are notably limited to work in *C. elegans*

(Barbosa et al., 2017; Gönczy et al., 1999; Nguyen-Ngoc et al., 2007; De Simone et al., 2018), which convincingly indicates that the sperm aster/pronuclear complex is predominantly pulled to the zygote center by dynein-dependent forces. Furthermore, a wealth of *in vitro* and *in silico* data indicates pushing during large aster migration is unlikely (Bjerknes, 1986; Dogterom and Yurke, 1997; Holy et al., 1997). Thus, a pushing mechanism for large aster positioning has not been identified. Here, we applied live cell imaging of MTs and their plus-ends, precise astral MT length measurements, coupled with MT length manipulation techniques and chemical ablation to reveal a long-ranged MT based pushing mechanism responsible for sperm aster centration in the sea urchin zygote.

Our findings contrast with the previously proposed cytoplasmic MT length-dependent pulling model in the sea urchin system (Hamaguchi and Hiramoto, 1986; Tanimoto et al., 2016). First, the pulling model is dependent on a longer front aster radius than the rear. However, we find the exact opposite with Lrear being substantially longer than Lfront during the second, rapid migration phase and the third phase of aster migration (Figures 1A-1B and S1B-S1C). The only time point in which we find Lfront to be equal to Lrear is during the early, slow moving penetration phase just after fertilization (Figures 1B and S1C). Our quantifications at each of the three stages of aster migration are strikingly consistent with early observations of aster asymmetry in the sea urchin (Chambers, 1939), yet are inconsistent with more recent work in support for a MT-length dependent pulling model (Tanimoto et al., 2016). One potential explanation for the inconsistencies between our result and recent work is a difference in the point of reference when performing aster length measurements. Measurements of aster Lfront and Lrear performed by Tanimoto et al., (2016) used the male pronucleus to estimate the location of the MTOC. As such, their study measures the aster radius in front and rear portions of the aster from the male pronucleus. Conversely, in our live and fix-cell imaging we perform our measurements

from the MTOC itself, which is located in front of the nucleus soon after fertilization (Figure 1C and Movie S1). Our observation that the MTOC is located in front of the male pronucleus is consistent with older work using electron microscopy, which shows that the MTOC rotates to the front of the male pronucleus prior to aster formation (Longo and Anderson, 1968). Because (Tanimoto et al., 2016) measures from the male pronucleus, which ranges from ~5-8 μm in length, these quantifications simultaneously over and under represent front and rear lengths of the aster, respectively. This over/under representation of front/rear aster radii likely accounts for the conclusion that the aster front radius is 5-10 μm longer than the rear (Tanimoto et al., 2016). Finally, one decisive advantage of our aster length measurements over previous quantifications is that we further support our measurements by imaging the aster in living cells. Such live cell imaging obviates potential artifacts of fixing MTs and pronuclei for immunofluorescence.

Second, experimental support for dynein's role in the cytoplasmic length-dependent pulling model was entirely based on the use of ciliobrevin, assuming that it's only effect was on dynein (Sallé et al., 2018; Tanimoto et al., 2016, 2018). We find that ciliobrevin completely abolishes aster integrity, preventing interpretations of its effects on dynein's role during sperm aster migration (Figures 4A-4B and Movie S4A). Indeed, the degree of specificity of ciliobrevin for dynein inhibition is unclear (Roossien et al., 2015), raising significant concerns about any results attributing its effects on aster migration to dynein inhibition. By inhibiting dynein specifically through p150-CC1 fragment injections, our work indicates that dynein may instead be functioning antagonistically to centration forces in the sea urchin sperm aster. That is, sperm asters center at a higher migration rate in p150-CC1 injected cells (Figures 4C-4E and Movie S4B). Therefore, our results indicate that retrograde transport by cytoplasmic dynein is more likely antagonistic to aster centration in sea urchin zygotes.

What is the exact role(s) for dynein during aster migration in the sea urchin? While we speculate more on the role of cortical and cytoplasmic dynein below, our study demonstrates with the use of p150-CC1 injection that cytoplasmic dynein is required for engagement and retrograde transport of the female pronucleus along the sperm sperm aster. A role for dynein during female pronuclear capture and transport has been well studied in other systems (Gönczy et al., 1999; Payne et al., 2003; Reinsch and Karsenti, 1997). However, outside the use of ciliobrevin, which causes a loss of the sperm aster (Figures 4A and 4B), a role for dynein during female pronuclear capture and transport has not been investigated in the sea urchin system prior to this study. We also demonstrate that while this transport provides pulling forces on the aster, it is neither essential for centration (Movie S3 and Figure S3A), nor is it guaranteed that this transport will happen on the front of the aster where centering pulling forces must occur in a MT length-dependent cytoplasmic pulling pulling model. That is, female pronuclear engagement and subsequent transport along the sperm aster occurs at locations and time points that are dependent on where the sperm enters the egg relative to the female pronucleus. If the egg is fertilized at a location in which the female pronucleus is located at the side of the aster, female pronuclear transport will generate pulling forces along the side portion of the sperm aster, which indeed causes minor lateral movements of the sperm aster toward the female pronucleus as it is being transported toward the male pronucleus (Chambers, 1939; Tanimoto et al., 2016). Furthermore, retrograde transport of the female pronucleus along the front of the sperm aster does not increase sperm aster migration rates (Tanimoto et al., 2016), as would be expected in a MT length-dependent cytoplasmic pulling model, which we hypothesize is likely because the sperm aster is anchored to the rear membrane (Figure 3), and migration rates are primarily determined by growth rates of the rear portion of the sperm aster (Figure 2). Together this data highlights that while retrograde cytoplasmic transport of the female pronucleus is dynein-dependent and does generate

pulling force along the sperm aster, it is not the predominant force driving aster centration and is not essential to successfully center the sperm aster in sea urchins.

Third, work done by (Tanimoto et al., 2016) using laser ablation of the side of the aster as a read out for pushing vs. pulling during migration, concluded that aster migration away from the side of ablation indicated pulling forces. Importantly, a role for dynein in these movements away from the side of ablation was not tested. A more direct way to determine if the aster is pushed or pulled to the center is the experiment proposed by (Reinsch and Gonczy, 1998), hypothesizing that ablation of the rear portion of the aster will halt migration in a MT pushing model. When we ablate the rear portion of the sperm aster, migration comes to a halt (Figures 5A-5C and Movie S5A). We instead favor the idea that any dynein-dependent pulling on side portions of the aster may maintain directionality of aster movement (Tanimoto et al., 2018) as it is being pushed to the zygote center by polymerization of rear MTs against the cortex. Consistent with this idea, we find that p150-CC1-mediated inhibition of dynein results in occasional rotation of the sperm aster as it approaches the center (Movie S4B), suggesting that dynein inhibition is causing defects in the direction of aster migration. This “steering” role for lateral astral MTs is also supported by ablations of side portions of the aster, which results in directional defects during aster migration (Tanimoto et al., 2016). We hypothesize that this phenotype could be due to a lack of dynein dependent force balancing along the sides of the aster when dynein is inhibited or by lack of dynein/dynactin anchoring of astral MTs at the cell cortex.

A final inconsistency we found between our data and the MT length-dependent cytoplasmic pulling model is in our aster MT density measurements. We find greater MT density in the rear portion of the sperm aster than in the front, which was not taken into account in the one-dimensional MT length-dependent pulling model (Tanimoto et al., 2016) (Figures 1E and S1D-S1E). In a cytoplasmic pulling model a greater number of MTs

in the aster rear should also allow more dynein-dependent force generation on the rear relative to the front, which is not the case because asters would then move toward the rear cortex rather than toward the cell center. Instead, the increased density we observe in the rear portions of the aster may be consistent with MT branching and/or bundling allowing for MT based pushing. A wealth of recent *in vitro* studies indicate that acentrosomal nucleation of MTs leads to large asters formed from branched MTs networks in *Xenopus* extracts (Alfaro-Aco et al., 2017; Petry et al., 2013; Song et al., 2018; Thawani et al., 2019). Additionally, MT branching *in vivo* was recently discovered to occur in mitotic asters of *Drosophila* S2 cells (Verma and Maresca, 2019). Furthermore, through a similar mechanism used for nucleating branching, MT bundle formation was recently showed to play a role in guiding spindle MTs to kinetochores (David et al., 2019). We hypothesize that MT branching/bundling could permit a pushing mechanism based on growth of numerous short MTs polymerizing against the cortex during large aster positioning, which would prevent MT buckling and slipping. Similarly, bundling of MTs should increase the amount of compression force allowed on MTs before buckling occurs. Interestingly, EB1-GFP comets along rear MTs in the aster appear to traverse over the same MT track multiple times, which partially accounts for the greater MT density along rear portions of the aster (Figures 1E, S1D-S1E and Movie S1). This “waterfall” pattern of EB1-GFP signal we observe is similar to the multiple EB3-GFP comets detected along MT tracks in bundled spindle MTs (David et al., 2019), suggesting that bundling may also occur in MTs within the rear portion of the sperm aster. Finally, it is worth noting that studies at first cleavage division in other invertebrates in which one mitotic aster is much larger than the sister aster suggests that as the large aster grows it pushes the whole mitotic apparatus toward the opposite pole resulting in unequal cell division (Ren and Weisblat, 2006). Consequently, pushing forces generated by astral growth may be used during mitosis as well. Future work investigating potential MT bundling/branch factors within the sea urchin sperm aster

may provide more details for how a large aster can be pushed through the viscous cytoplasm.

Our study also reveals that the sperm aster is robustly anchored to the rear cortex in the sea urchin zygote (Figure 3 and Movie S3), which is similar to the anchoring of meiotic maternal centrioles in other systems (Fabritius et al., 2011). We find that membrane invaginations, likely where the sperm aster is anchored to the rear cortex, are only observed when the sperm aster captures the female pronucleus, indicating that pulling forces are negligible until the male and female pronuclei engage (Figures 3D-3E and Movie S3). Furthermore, in enucleated zygotes we find that the sperm aster still migrates to the cell center in the absence of engagement between the male and female pronuclei (Movie S3). These data suggest that force production from retrograde transport of the female pronucleus is not essential for sperm aster centration. An important question moving forward is how and why the sperm aster is anchored to the cortex. We predict, based on our results, that dynein is required to anchor the aster to the cortex as in other systems (Fujita et al., 2015; Kotak et al., 2012). Here we hypothesize that attachment of the aster to the rear cortex by dynein/dynactin, in combination with branching/bundling, helps prevent slipping of MTs as they polymerize and push the aster to the zygote center. Indeed, previous work suggests that pushing is more effective when slipping is reduced, while puling is more effective when slipping is increased (Pavin et al., 2012). Additionally, dynein may be required to regulate MT growth and anchoring at the cortex (Laan et al., 2012). Consistent with this idea, the rotational phenotype of asters in p150-CC1 injected cells could be due to an overgrowth of unanchored MTs once the aster is centered or near the centered, causing MT buckling. Thus, our study provides an *in vivo* framework for future studies to elucidate the physical nature of polymerization-induced pushing forces at the cell cortex during large aster positioning.

2.4 STAR Methods

2.4.1 Key Resources Table

REAGENT or RESOURCE	SOURCE	IDENTIFIER
Antibodies		
Anti-α-Tubulin, clone DM1A, Alexa Fluor 488 conjugate (Mouse monoclonal)	MilliporeSigma	16-232
Chemicals, Peptides, and Recombinant Proteins		
Protamine sulfate	Sigma-Aldrich	P4020
Urethane, Minimum 99%	Sigma-Aldrich	U2500
Hexylene glycol 99%	Sigma-Aldrich	112100
Hoescht Solution	ThermoFisher Scientifi	33342
Caged-Combretastatin 4A	Gift from Timothy Mitchison, Christine Field, and James Pelletier, Harvard University, (Wühr et al., 2010)	N/A
Tau peptide-mCherry	Gift from Jessie Gatlin, University of Wyoming (Mooney et al., 2017)	N/A
P150-CC1 peptide fragment	Gift from Timothy Mitchison, Christine Field, and James Pelletier, Harvard University, (Wühr et al., 2010)	N/A

EB1 peptide-GFP	Gift from Timothy Mitchoson, Christine Field, and James Pelletier, Harvard University	N/A
VALAP	Vaseline, Lanolin, Paraffin in 1:1:1 mass ratio	
Ciliobrevin D	Sigma-Aldrich	250401
Experimental Models: Organisms/Strains		
Sea Urchin *Lytechinus Pictus*	Marinus Scientific, LLC.	http://www.marinusscientific.com/
Software and Algorithms		
ImageJ	NIH	https://imagej.nih.gov/ij/index.html
Zen Black	Carl Zeiss Microscopy, LLC	https://www.zeiss.com/microscopy/us/downloads.html
Zen Blue	Carl Zeiss Microscopy, LLC	https://www.zeiss.com/microscopy/us/downloads.html
LAS AF	Leica Microsystems	https://www.leica-microsystems.com/products/microscope-software/p/leica-las-x-ls/
Graphpad Prism 8.2.1 for Windows 10	(Culley et al., 2018) Graphpad Software, La Jolla California USA	https://www.graphpad.com

2.4.2 Experimental model and Subject Details

Lytechinus Pictus

Sea urchins *Lytechinus pictus* were purchased from Marinus Scientific (Long Beach, Ca). Animals were maintained in a temperature-controlled aquarium at 16C filled with artificial sea water (ASW) made from Instant Ocean mix (30-35 ppm). Urchins were exposed to light cycles of 12 hour intervals. Gametes were collected the day of use by intracoelomic injection of .5M KCl. Adult L. pictus have no sexual dimorphism, so sex could only be determined after spawning. Sperm could be stored and used for up to ~5 days post-collection. Sperm was diluted and activated in filtered sea water from the Woods Hole Marine Biological Laboratories (MBLSW) at a 1:1000 dilution. Eggs were collected directly into MBLSW. For fixed imaging, eggs were fertilized and passed through a Nitex membrane (86-102 um) several times to remove fertilization envelopes and raised in filtered sea water at the appropriate temperatures until our time points of interest. For live imaging, jelly coats were removed from eggs by several passes through a 102 um Nitex membrane.

2.4.3 Method Details

Microscopy

Live and fixed-cell imaging of MTs and MT plus-ends was performed on a Zeiss 880 laser point scanning confocal microscope mounted with an Airyscan detector using a 40x 1.1 NA water immersion objective. Samples were maintained on a water-cooled stage at 16C connected to a refrigerated water circulator. Fixed MTs were imaged using an Argon laser, while live MTs were imaged using a 488 or 561 nm laser, depending on the fluorophore. Airyscan post acquisition processing was performed using Zen Blue software. Live-cell imaging of the male pronucleus was performed using a Leica SP5 laser point scanning confocal microscope with a 40x 1.1 NA water immersion objective and a 405 nm UV laser. The room for this microscope was maintained at 14-16 C.

Cellular orientation used to define front and rear portions of the aster

In all image acquisition throughout this study, cells were selected for in which the sperm enters +/- 10 um from the cell equator along the Z-axis (see Figure S1A). This equatorial fertilization ensures that the aster migrates along the cell equator without any deviations along the Z-axis. In this way, any portions of the aster that are slanted in the Z-axis are defined as “top” or “bottom”, while all portions of the aster parallel to the migration axis and coverslip are defined as “front’ or “rear” (Figure S1A). This orientation helps to exclude any top and bottom portions of the aster from our analysis of aster geometry. In live-cell imaging slanted portions of the aster leave the imaging plane, effectively excluding them from analysis. Similarly, in our immunofluorescence analysis, due to the spherical nature of the aster, slanted portions of the sperm aster do not extend to the maximum front and rear boundaries of the sperm aster in the X/Y axis (Figure S1A). Because we measure from the MTOC to the maximum aster boundaries in front and rear portions, as outlined below, these slanted top and bottom portions of the aster are excluded from our quantifications (Figure S1A).

Live MT and MT plus-end imaging

Tau-mCherry and EB1-GFP-labeled MT plus-ends and MTs were imaged on a Zeiss 880 Airyscan with a 40x 1.1 NA water immersion objective. Movies for Figure 2 were imaged at 5, 10, and 15 minute time points post sperm addition. Movies for Figure 1 were acquired at different time points based on how far the aster moved from the site of sperm entry, determined by EB1-GFP detection of the MTOC. In order to thoroughly sample the MTs and their plus-ends throughout migration, these time points were standardized to 10, 15, 20, 25, 30, and 35 μm of distance moved from the site of sperm entry (Figures 1A-1B and Movie S1). For both figures, single z-slices of EB1-GFP through the middle of the centrosome were acquired at 2.5 second intervals for at least 30 seconds at each time point, followed by a single z-slice of Tau-mCherry signal. For Figures 4 and 5, single z-slices (10-15 second/frame) of Tau-mCherry were acquired at the centrosome throughout the duration of aster migration (10-15 minutes).

Fixed MT imaging

To image DM1A-labeled α-tubulin in whole zygotes, fixed immunofluorescence imaging was performed on a laser point scanning confocal microscope (Zeiss 880 Airyscan), controlled by Zen Black software with a 40x 1.1 NA water immersion objective. 3D volumes (40 μm, composed of 20 z-sections at 2 μm intervals) were acquired for each sample to ensure the entire aster (Figures 1C, 3D, and 4A) was acquired in each data set. Only zyogtes in which the centrosomes were +/- 10 μm from the cell equator were imaged in order to ensure front and rear portions of the aster could be defined (see processing and analysis below for definitions). Isolated cortices were imaged on a Zeiss LSM 780 (Marine Biology Laboratories, Woodshole, MA), controlled by Zen Black with a 40X 1.2 NA water immersion objective. 3D volumes (10 μm, composed of 10 μm sections at 1 μm intervals, or roughly the thickness of the cortex) were acquired (Figure 3A).

Live pronuclei imaging

Eggs and sperm were incubated with Hoescht at a final concentration of 1 ug/ml to allow staining of male and female pronuclei. Eggs were then added to glass bottom dishes (35 x 10 mm) and allowed to settle to minimize movement during imaging. Hoescht-labeled pronuclei (movies for Figures S2B, 3C, and Movie S3) were imaged using a Leica SP5 LSM, controlled by LAS AF software, with a 40x 1.1 NA water immersion objective and a 405 nm UV laser. Zygotes in which the sperm entered +/- 10 μm from the cell equator were chosen for imaging to reduce the 3D volume required to capture the entire pronuclear migration process. 3D volumes of 40 μm at 2 μm intervals were acquired every 10-15 seconds from sperm penetration until male pronuclear centration was complete.

Processing and analysis of confocal microscopy images

Measuring aster Lfront and Lrear with EB1-GFP signal

The exact distance of individual EB1-GFP comets from the centrosome could not be reliably measured because the density of comets was too high, especially in rear portions of the aster. We therefor converted EB1-GFP movies (Figures 1A-1B, 2D-2E, Movies S1-S2) to maximum intensity temporal projections, which plots comet movement over time in a single 2D image. These plots

revealed smooth MT tracks, which represent individual MTs and/or MT bundles within the sperm asters. We then measured the distance from the most distal portion of EB1-tracks to the MTOC using FIJI (imageJ). We defined the front portions of the aster as an ROI extending in front of the MTOC (cytoplasmic facing) at 45 degree angles relative to the directional axis of aster migration, which in total produces a 90 degree ROI. Likewise, the rear portion of the aster was defined as an ROI extending behind the MTOC, between the MTOC and the cortical face containing the site of sperm entry, at 45 degree angles on each side of the directional axis of aster migration. These definitions thus excluded MTs on the remaining 90 degree ROIs on each side portion of the aster. All EB1-GFP tracks in each front and rear ROI at each of our time points were then averaged for each zygote to define the Lfront and Lrear, respectively. We then calculated a cumulative average of the Lfront and Lrears of all of the zygotes to obtain an average Lfront and Lrear. Differences between average LFront and Lrear were then tested for statistical significance ($P<.05$) using a 2 way ANOVA followed by a Tukey's multiple comparisons test using Graphpad Prism 8. In Figure 2E average Lfront and Lrear were also compared to distance moved (see below for aster migration rate quantification methods). In these quantifications, differences between Lfront or Lrear portions of the aster and distance moved were also individually tested for statistical significance ($P<.05$) by also using a 2-way ANOVA followed by Tukey's multiple comparisons.

Measuring aster Lfront and Lrear with Tau-mCherry signal and DM1A α-tubulin

Following EB1-GFP time-lapse acquisition, we obtained 1 frame of a single z-slice of Tau-mCherry signal from the same zygote, which allowed us the advantage of measuring lengths of potentially stable, non-growing MTs. We applied the same ROIs used to define front and rear portions of the aster during our EB1-GFP MT length measurements, and measured the lengths of the most distal tip of all detectable MTs/bundles to the centrosome in front and rear ROIs. We then averaged the lengths MT/bundles in front and rear ROIs to define Lfront and Lrear for each cell, and further cacluated the averages of Lfront and Lrear from all zygotes, similar to our EB1-GFP MT length measurements. Differences between average Lfront and Lrear from all zygotes were then tested for statistical significance ($P<.05$) using a 2-way ANOVA followed by Tukey's multiple comparisons.

We applied the same quantifications to maximum intensity projections of asters obtained from our 3D volumes of fixed immunofluorescence of DM1A-tagged α-tubulin (Figures 1C-1D).

Quantifying EB1-GFP and Tau-mCherry Fluorescence intensity

To estimate MT density in front and rear portions we converted each of our EB1-GFP time-lapse videos from Figures 1 into average temporal projections using Fiji (ImageJ). We then applied the same defined front and rear ROIs used in our MT/bundle length measurements. We manually measured fluorescence intensities as a function of distance from the centrosome in each ROI by using manually drawn lines in Fiji (ImageJ), perpendicular to the directional axis of aster migration at 2 μm intervals from the centrosome. The EB1-GFP background signal (and non-astral MTs) was estimated by measuring the average fluorescence intensity of three 10 μm diameter circles randomly placed in cytoplasm that is void of astral MTs. We then subtracted the average background signal from our fluorescence intensity measurements made in the aster. Next, we normalized our front and rear astral fluorescence intensities to the average fluorescence intensities of the MTOC, measured in a 2 μm diameter circle manually placed around the MTOC. This provided us with normalized average intensities of EB1-GFP signal at 2 μm intervals from the centrosome in front and rear portions of the sperm aster. We then calculated the statistical differences ($P<.05$) between intensity profiles from front and rear portions of the aster using a 2-way ANOVA followed by Sidak's multiple comparisons test in Graphpad Prism 8. We applied the same method to our single z-slice/single time frame images of Tau-mCherry signal obtained after EB1-GFP time lapse videos from the same cells, which yields similar intensity profiles in rear and front portions of the aster (Figure S1C).

Tracking aster migration rates using EB1-GFP signal and Hoescht-labeled male and female pronuclei

Confocal time-lapse videos of hoescht-labeled pronuclei (Figures S2B, 3C, and Movie S3) were converted to maximum intensity projections of the 3D volumes. We then tracked how far each pronucleus moved at each 10-15 second time interval by hand using Fiji (ImageJ). Because only zygotes in which sperm entry was at +/- 10 μm from the cell equator, deviations in Z were rare,

similar to what was seen by (Tanimoto et al., 2016). The average distance moved for each time point was then calculated and plotted as distances vs. time curves.

Aster migration rates were also quantified from confocal time-lapse videos of single z-slice EB1-GFP labeled MTOCs by measuring the distance between the MTOC and the site of sperm entry at 5, 10, and 15-minute time points post-fertilization using Fiji (ImageJ). These rates were then averaged and compared with the average rates obtained from Hoescht-labeled pronuclear tracking quantifications using Graphpad Prism 8, which produced no significant difference ($P<.05$) in a 2-way ANOVA followed by Tukey's multiple comparison.

The three separate phases of aster migration (Figure S2B) where determined by three regions of differential migration rates on distance vs. time plots: 0-5 min post fertilization,5-10 minutes post fertilization, and 10-15 minutes post fertilization. Aster speed during each of these three phases was determined by linear fitting of each phase, which yielded the slope of the curve throughout each phase of migration (2.29 +/-.09 μm, 4.8 +/- 2 μm, and 1.250 +/- .25 μm for phase 1, 2, and 3 respectively). The slopes were determined to be statistically different ($P<.001$) by performing an ANCOVA analysis of the three curves. All statistical analysis for this method were performed in Graphpad Prism 8.

Comparison of Lfront/Lrear and migration rates

Lfront and Lrear, quantified from our EB1-GFP length measurements in untreated zygotes were determined over 5, 10, and 15 minute time points and compared to our migration rate data (Figure S2C). We determined if there are any changes in Lfront and Lrear associated with the changes in migration rates by fitting the computed aster migration and Lfront/Lrear curves to a logistic model, which predicts an increased growth/migration rates (initial phase of aster migration) to a constant maximum growth/migration rate (second phase of migration), followed by a decrease in growth/migration rates as MTs reach their maximum lengths. Analysis was performed using Graphpad Prism 8.

Tracking aster migration distance using Tau-mCherry signal

To study the movement of Tau-mCherry labeled sperm asters, we measured the distance of the centrosome to the site of sperm entry manually using Fiji (ImageJ) at each 10-15 second intervals in our single z-plane videos (Movies S4B and S5). We then calculated the total average distance moved among all of our samples for each time point. The average distance was then plotted either as a function of time post sperm entry (Figure 4D), or as a function of time before and after UV-activation of CA4 (Figure 5C). Statistical differences in average distance moved at each ($P<.05$) between conditions were calculated using a 2-way ANOVA followed by Sidak's multiple comparisons test (Figure 4D and 5C).

Quantification of equatorial division

Eggs were fertilized in the presence of 50 nM CA4 or DMSO (control), protected from light, and incubated to the two-cell stage. They were then imaged under a brightfield dissecting microscope. Only embryos positioned with their long axis parallel to the bottom of the dish were chosen for analysis in order to accurately measure diameter of each of the two cells within each embryo. Diameter was measured from the plasma membrane between the two cells to the cell pole for each cell. The slightly smaller of the two cells was then divided by the slightly larger of the two cells to obtain the cell:cell ratio (Figure 5E). This experiment was repeated on 3 different batches of eggs from 3 separate female urchins.

Measuring the distance of the male pronucleus from the cell center

The center of the cell was defined as one half the cell diameter (or radius) as measured from the plasma membrane to the cell interior in maximum intensity projections of time-lapse confocal images. The distance from the center of the male pronucleus at the end of migration was then measured to this defined cell center using Fiji (ImageJ). The average distance was then calculated for all of our samples in each condition. Differences in averages were then calculated using a standard ANOVA in Graphpad Prism 8.

Immunostaining

Whole-cell zygotes were fixed and permeabilized in bulk (1.5 ml Eppendorf tubes) at the indicated time points (Figures 1C and 4A) using a fixation buffer composed of 100 mM Hepes (pH 7.0), 50 mM EGTA (pH 7.0), 10 mM MgSO4, 400 mM dextrose, 2% formaldehyde, and .2% Triton-X. Samples were incubated for 1 hr at room temperature with gentle agitation, rinsed 3X with (PBST) and left to sit overnight in PBST. We blocked samples in 5% BSA/PBST for 2 hrs at room temperature on a rocker. Samples were then transferred to Alexa-488 conjugated DM1A alpha tubulin antibody (1:1000) (EMD Millipore) in 5% BSA/PBST for 48 hrs at room temperature on a rocker. We rinsed the samples 3X in PBST over the course of 2 hours. Samples were mounted in 90% glycerol on chamber slides made from double-sided tape using 24 x 24 mm coverslips with a thickness no. 1.5 and sealed with VALAP.

Cortical isolations

Zygote cortical isolation procedures were adapted from (Burgess and Schroeder, 1977). Eggs were dejellied by incubation in acidic sea water (pH 4.0) for 3 min before transferring them back to filtered sea water. We then induced polyspermy by fertilizing the eggs in sea water containing 4 mg/ml of soy bean trypsin inhibitor (SBTI). At 5 minutes post-sperm addition zygote were settled onto protamine sulfate-coated coverslips. 3-5 minutes later (8 to 10 minutes post-sperm addition), zygotes were sheared by pipetting an isotonic buffer containing 0.8 M mannitol, 5mM MgCl2, 10 mM EGTA, and 10 mM HEPES (pH 7.4). Coverslips with the remaining cortices were then submerged in 2% formaldehyde/isotonic buffer for 5 min and processed for immunofluorescence microscopy (Figure 3A).

Microinjections

Dejellied eggs were rowed on coverslips coated with .1% protamine sulfate to prevent movement during injections and imaging. Coverslips were mounted in metal injection chambers containing MBLSW maintained at 16C. Injection volumes were set to roughly 3-5% of the egg volume using a Picospritzer III pressure regulator connected to a foot pedal injection control system. This injection volume resulted in final concentrations of roughly 10.5-17.5 nM of Tau-mCherry, .1mg/ml of EB1-GFP, and .25 ug/ml of p150-CC1. 20-25 eggs were injected per experiment. Eggs were then

allowed to incubate for 10 minutes at 16C to recover from injections. We then fertilized the eggs under the Ziess 880 LSM Airyscan and monitored them for sperm entry and aster growth.

Pharmacological inhibitors

For HG and urethane experiments (Figure 2), inhibitors were added to unfertilized eggs in filtered sea water and pre-incubated for 5-10 minutes before fertilization. Urethane (Sigma, >99% purity) was diluted in DMSO, and used at a 100 mM final concentration. HG (Sigma) was diluted to 0.7% in MBLSW. Control samples were treated with equal amounts of DMSO to experimental conditions. Ciliobrevin D (Sigma) was diluted to various concentrations in DMSO and added to zygotes 5 minutes post-fertilization (Figure 4A). Zygotes were either fixed ~3-5 minutes later and processed for immunofluorescence microscopy or immediately imaged for live-cell observation of aster dynamics.

Egg nuclear sedimentation and enucleation

Eggs in MBLSW were distributed over a 1.1M sucrose pad at 1 part eggs and 2 parts sucrose (Harvey, 1933). To float the female pronucleus to the egg periphery, we centrifuged them at 10,000g for 6 minutes. For enucleation, we centrifuged eggs at 10,000g for 10 minutes. In all conditions we used a Sorval HB-4 rotor. The eggs were then collected, rinsed 2X in filtered sea water, and labeled for DNA using 1ug/ml of Hoescht. We incubated eggs in 100 uM urethane or equal amounts of DMSO for control and enucleated conditions. Following treatment, we fertilized the eggs in glass bottom petri dishes (35 x 10 mm) and looked for zygotes in which the sperm entered directly opposite of the female pronucleus. We acquired 20-40 um z-stacks every 5-15 seconds until centration and pronuclear fusion was complete.

Chemical ablations

Eggs injected with Tau-mCherry fusion protein were treated with 50 nM of combretastatin 4A (CA4) (a gift from the Mitchison Lab) (Wühr et al., 2010), protected from light, and fertilized 10 minutes after injection. The drug was activated in a defined region of the rear portion, side or front portions of the aster using a 405 nm laser with 13 µsec dwell time on a Zeiss 880 LSM Airyscan. The region

of CA4 activation was near the distal portions of MTs (seen by Tau-mCherry signal), to prevent immediate diffusion of the active drug to other portions of the aster. Additionally, eggs in which CA4 was not uncaged were allowed to proceed through spindle formation and cleavage. These samples were subsequently imaged at a Z-plane through the bipolar MTOCs in order to show the center of spindle and telophase asters along their long axis respectively (Figure 5D).

Acknowledgements

We would like to thank Dr. Jesse Gatlin for sending us the Tau-mCherry fusion protein for imaging live MTs. We would also like to thank Dr. Timothy Mitchison, Dr. Christine Field, and James Pelletier for supplying us with CA4, p150-CC1, and EB1-GFP peptides, as well as for fruitful discussions. Finally, we would like to thank Dr. Charles Shuster and Leslie Toledo-Jacobo for constructive feedback when preparing the manuscript. We thank Bret Judson and the Boston College Imaging Core for infrastructure and support. This material is based upon work supported by NSF Grant No. 124425 to D.R.B.

Author Contributions

J.L.M conceived and designed experiments, performed the experiments, analyzed and interpreted the results, and wrote the manuscript. S.N.M. helped obtain and image enucleated eggs. D.R.B. conceived the project, designed experiments, and provided input and feedback for the manuscript.

Declaration of Interests

The authors declare no competing interests.

References

Alfaro-Aco, R., Thawani, A., and Petry, S. (2017). Structural analysis of the role of TPX2 in branching microtubule nucleation. J. Cell Biol. *216*, 983 LP – 997.

Barbosa, D.J., Duro, J., Prevo, B., Cheerambathur, D.K., Carvalho, A.X., and Gassmann, R. (2017). Dynactin binding to tyrosinated microtubules promotes centrosome centration in C. elegans by enhancing dynein-mediated organelle transport. PLOS Genet. *13*, e1006941.

Bergen, L.G., Kuriyama, R., and Borisy, G.G. (1980). Polarity of microtubules nucleated by centrosomes and chromosomes of Chinese hamster ovary cells in vitro. J. Cell Biol. *84*, 151 LP – 159.

Bestor, T.H., and Schatten, G. (1981). Anti-tubulin immunofluorescence microscopy of microtubules present during the pronuclear movements of sea urchin fertilization. Dev. Biol. *88*, 80–91.

Bjerknes, M. (1986). Physical theory of the orientation of astral mitotic spindles. Science (80-.). *234*, 1413 LP – 1416.

Burgess, D.R., and Schroeder, T.E. (1977). Polarized bundles of actin filaments within microvilli of fertilized sea urchin eggs. J. Cell Biol. *74*, 1032–1037.

Chambers, E.L. (1939). The Movement of the Egg Nucleus in Relation to the Sperm Aster in the Echinoderm Egg. J. Exp. Biol. *16*, 409 LP – 424.

Costache, V., Hebras, C., Pruliere, G., Besnardeau, L., Failla, M., Copley, R.R., Burgess, D., Chenevert, J., and McDougall, A. (2017). Kif2 localizes to a subdomain of cortical endoplasmic reticulum that drives asymmetric spindle position. Nat. Commun. *8*, 917.

Culley, S., Albrecht, D., Jacobs, C., Pereira, P.M., Leterrier, C., Mercer, J., and Henriques, R. (2018). Quantitative mapping and minimization of super-resolution optical imaging artifacts. Nat. Methods *15*, 263.

David, A.F., Roudot, P., Legant, W.R., Betzig, E., Danuser, G., and Gerlich, D.W. (2019). Augmin accumulation on long-lived microtubules drives amplification and kinetochore-directed growth. J. Cell Biol. *218*, 2150–2168.

Dogterom, M., and Yurke, B. (1997). Measurement of the Force-Velocity Relation for Growing Microtubules. Science (80-.). *278*, 856–860.

Dogterom, M., Kerssemakers, J.W., Romet-Lemonne, G., and Janson, M.E. (2005). Force generation by dynamic microtubules. Curr. Opin. Cell Biol. *17*, 67–74.

Fabritius, A.S., Ellefson, M.L., and McNally, F.J. (2011). Nuclear and spindle positioning during oocyte meiosis. Curr. Opin. Cell Biol. *23*, 78–84.

Firestone, A.J., Weinger, J.S., Maldonado, M., Barlan, K., Langston, L.D., O'Donnell, M., Gelfand, V.I., Kapoor, T.M., and Chen, J.K. (2012). Small-molecule inhibitors of the AAA+ ATPase motor cytoplasmic dynein. Nature *484*, 125.

Fujita, I., Yamashita, A., and Yamamoto, M. (2015). Dynactin and Num1 cooperate to establish the cortical anchoring of cytoplasmic dynein in S. pombe. J. Cell Sci. *128*, 1555 LP – 1567.

Gönczy, P., Pichler, S., Kirkham, M., and Hyman, A.A. (1999). Cytoplasmic Dynein Is Required for Distinct Aspects of Mtoc Positioning, Including Centrosome Separation, in the One Cell Stage Caenorhabditis elegans Embryo. J. Cell Biol. *147*, 135 LP – 150.

Goshima, G., Nédélec, F., and Vale, R.D. (2005). Mechanisms for focusing mitotic spindle poles by minus end–directed motor proteins. J. Cell Biol. *171*, 229 LP – 240.

Hamaguchi, M.S., and Hiramoto, Y. (1986). Analysis of the Role of Astral Rays in Pronuclear Migration in Sand Dollar Eggs by the Colcemid-UV Method. Dev. Growth Differ. *28*, 143–156.

Harris, P., Osborn, M., and Weber, K. (1980). Distribution of tubulin-containing structures in the egg of the sea urchin Strongylocentrotus purpuratus from fertilization through first cleavage. J. Cell Biol. *84*, 668 LP – 679.

Harvey, E.B. (1933). Development of the Parts of Sea Urchin Eggs Separated by Centrifugal Force. Biol. Bull. *64*, 125–148.

Henson, J.H., Samasa, B., and Burg, E.C. (2019). High resolution imaging of the cortex isolated from sea urchin eggs and embryos. Methods Cell Biol. *151*, 419–432.

Holy, T.E., Dogterom, M., Yurke, B., and Leibler, S. (1997). Assembly and positioning of microtubule asters in microfabricated chambers. Proc. Natl. Acad. Sci. *94*, 6228 LP – 6231.

Ishihara, K., Nguyen, P.A., Groen, A.C., Field, C.M., and Mitchison, T.J. (2014). Microtubule nucleation remote from centrosomes may explain how asters span large cells. Proc. Natl. Acad. Sci. *111*, 17715 LP – 17722.

Ishihara, K., Korolev, K.S., and Mitchison, T.J. (2016). Physical basis of large microtubule aster growth. Elife *5*.

Kimura, A., and Onami, S. (2005). Computer Simulations and Image Processing Reveal Length-Dependent Pulling Force as the Primary Mechanism for C. elegans Male Pronuclear Migration. Dev. Cell *8*, 765–775.

Kimura, K., and Kimura, A. (2011). Intracellular organelles mediate cytoplasmic pulling force for centrosome centration in the Caenorhabditis elegans early embryo. Proc. Natl. Acad. Sci. *108*, 137 LP – 142.

Kotak, S., Busso, C., and Gönczy, P. (2012). Cortical dynein is critical for proper spindle positioning in human cells. J. Cell Biol. *199*, 97–110.

Kozlowski, C., Srayko, M., and Nedelec, F. (2007). Cortical Microtubule Contacts Position the Spindle in C. elegans Embryos. Cell *129*, 499–510.

Laan, L., Pavin, N., Husson, J., Romet-Lemonne, G., van Duijn, M., López, M.P., Vale, R.D., Jülicher, F., Reck-Peterson, S.L., and Dogterom, M. (2012). Cortical Dynein Controls Microtubule Dynamics to Generate Pulling Forces that Position Microtubule Asters. Cell *148*, 502–514.

Longo, F., and Anderson, E. (1968). The Fine Structure of Pronuclear Development and Fusion in the Sea Urchin, Arbacia Punctulata. J. Cell Biol. *30*.

Merdes, A., Heald, R., Samejima, K., Earnshaw, W.C., and Cleveland, D.W. (2000). Formation of Spindle Poles by Dynein/Dynactin-Dependent Transport of Numa. J. Cell Biol. *149*, 851 LP – 862.

Minc, N., Burgess, D., and Chang, F. (2011). Influence of Cell Geometry on Division-Plane Positioning. Cell *144*, 414–426.

Mooney, P., Sulerud, T., Pelletier, J.F., Dilsaver, M.R., Tomschik, M., Geisler, C., and Gatlin, J.C. (2017). Tau-based fluorescent protein fusions to visualize microtubules. Cytoskeleton *74*, 221–232.

Murata, T., Sonobe, S., Baskin, T.I., Hyodo, S., Hasezawa, S., Nagata, T., Horio, T., and Hasebe, M. (2005). Microtubule-dependent microtubule nucleation based on recruitment of γ-tubulin in higher plants. Nat. Cell Biol. *7*, 961.

Negishi, T., Miyazaki, N., Murata, K., Yasuo, H., and Ueno, N. (2016). Physical association between a novel plasma-membrane structure and centrosome orients cell division. Elife *5*, e16550.

Nguyen-Ngoc, T., Afshar, K., and Gönczy, P. (2007). Coupling of cortical dynein and Gα proteins mediates spindle positioning in Caenorhabditis elegans. Nat. Cell Biol. *9*, 1294.

Paix, A., Le Nguyen, P.N., and Sardet, C. (2011). Bi-polarized translation of ascidian maternal mRNA determinant pem-1 associated with regulators of the translation machinery on cortical Endoplasmic Reticulum (cER). Dev. Biol. *357*, 211–226.

Pavin, N., Laan, L., Ma, R., Dogterom, M., and Jülicher, F. (2012). Positioning of microtubule organizing centers by cortical pushing and pulling forces. New J. Phys. *14*, 105025.

Payne, C., Rawe, V., Ramalho-Santos, J., Simerly, C., and Schatten, G. (2003). Preferentially localized dynein and perinuclear dynactin associate with nuclear pore complex proteins to mediate genomic union during mammalian fertilization. J. Cell Sci. *116*, 4727–4738.

Peng, C.J., and Wikramanayake, A.H. (2013). Differential Regulation of Disheveled in a Novel Vegetal Cortical Domain in Sea Urchin Eggs and Embryos: Implications for the Localized Activation of Canonical Wnt Signaling. PLoS One *8*, e80693.

Petry, S., Groen, A.C., Ishihara, K., Mitchison, T.J., and Vale, R.D. (2013). Branching Microtubule Nucleation in Xenopus Egg Extracts Mediated by Augmin and TPX2. Cell *152*, 768–777.

Pollard, T.D., and O'Shaughnessy, B. (2019). Molecular Mechanism of Cytokinesis. Annu. Rev. Biochem. *88*, null.

Quintyne, N.J., Gill, S.R., Eckley, D.M., Crego, C.L., Compton, D.A., and Schroer, T.A. (1999). Dynactin Is Required for Microtubule Anchoring at Centrosomes. J. Cell Biol. *147*, 321–334.

Rappaport, R. (1961). Experiments concerning the cleavage stimulus in sand dollar eggs. J. Exp. Zool. *148*, 81–89.

Rappaport, R., and Rappaport, B.N. (1984). Division of constricted and urethane-treated sand dollar eggs: A test of the polar stimulation hypothesis. J. Exp. Zool. *231*, 81–92.

Redemann, S., Pecreaux, J., Goehring, N.W., Khairy, K., Stelzer, E.H.K., Hyman, A.A., and Howard, J. (2010). Membrane Invaginations Reveal Cortical Sites that Pull on Mitotic Spindles in One-Cell C. elegans Embryos. PLoS One *5*, e12301.

Reinsch, S., and Gonczy, P. (1998). Mechanisms of nuclear positioning. J. Cell Sci. *111*, 2283 LP – 2295.

Reinsch, S., and Karsenti, E. (1997). Movement of nuclei along microtubules in Xenopus egg extracts. Curr. Biol. *7*, 211–214.

Ren, X., and Weisblat, D.A. (2006). Asymmetrization of first cleavage by transient disassembly of one spindle pole aster in the leech Helobdella robusta. Dev. Biol. *292*, 103–115.

Roegiers, F., Djediat, C., Dumollard, R., Rouviere, C., and Sardet, C. (1999). Phases of cytoplasmic and cortical reorganizations of the ascidian zygote between fertilization and first division. Development *126*, 3101 LP – 3117.

Roossien, D.H., Miller, K.E., and Gallo, G. (2015). Ciliobrevins as tools for studying dynein motor function. Front. Cell. Neurosci. *9*, 252.

Saito, T.T., Okuzaki, D., and Nojima, H. (2006). Mcp5, a meiotic cell cortex protein, is required for

nuclear movement mediated by dynein and microtubules in fission yeast. J. Cell Biol. *173*, 27–33.

Sallé, J., Xie, J., Ershov, D., Lacassin, M., Dmitrieff, S., and Minc, N. (2018). Asymmetric division through a reduction of microtubule centering forces. J. Cell Biol. jcb.201807102.

Schatten, G. (1981). Sperm incorporation, the pronuclear migrations, and their relation to the establishment of the first embryonic axis: Time-lapse video microscopy of the movements during fertilization of the sea urchin Lytechinus variegatus. Dev. Biol. *86*, 426–437.

De Simone, A., Spahr, A., Busso, C., and Gönczy, P. (2018). Uncovering the balance of forces driving microtubule aster migration in C. elegans zygotes. Nat. Commun. *9*, 938.

Song, J.-G., King, M.R., Zhang, R., Kadzik, R.S., Thawani, A., and Petry, S. (2018). Mechanism of how augmin directly targets the γ-tubulin ring complex to microtubules. J. Cell Biol. *217*, 2417 LP – 2428.

Strickland, L.I., Donnelly, E.J., and Burgess, D.R. (2005). Induction of Cytokinesis Is Independent of Precisely Regulated Microtubule Dynamics. Mol. Biol. Cell *16*, 4485–4494.

Tanimoto, H., and Minc, N. (2017). Quantitative approaches for the study of microtubule aster motion in large eggs. Methods Cell Biol. *139*, 69–80.

Tanimoto, H., Kimura, A., and Minc, N. (2016). Shape–motion relationships of centering microtubule asters. J. Cell Biol. *212*, 777 LP – 787.

Tanimoto, H., Sallé, J., Dodin, L., and Minc, N. (2018). Physical forces determining the persistency and centring precision of microtubule asters. Nat. Phys. *14*, 848–854.

Thawani, A., Stone, H.A., Shaevitz, J.W., and Petry, S. (2019). Spatiotemporal organization of branched microtubule networks. Elife *8*, e43890.

Tran, P.T., Marsh, L., Doye, V., Inoué, S., and Chang, F. (2001). A Mechanism for Nuclear Positioning in Fission Yeast Based on Microtubule Pushing. J. Cell Biol. *153*, 397 LP – 412.

Verma, V., and Maresca, T.J. (2019). Direct observation of branching MT nucleation in living animal cells. J. Cell Biol. *218*, 2829–2840.

Wühr, M., Tan, E.S., Parker, S.K., Detrich, H.W., and Mitchison, T.J. (2010). A Model for Cleavage Plane Determination in Early Amphibian and Fish Embryos. Curr. Biol. *20*, 2040–2045.

Yi, J., Wu, X., Chung, A.H., Chen, J.K., Kapoor, T.M., and Hammer, J.A. (2013). Centrosome repositioning in T cells is biphasic and driven by microtubule end-on capture-shrinkage. J. Cell Biol. *202*, 779 LP – 792.

Alfaro-Aco, R., Thawani, A., and Petry, S. (2017). Structural analysis of the role of TPX2 in branching microtubule nucleation. J. Cell Biol. *216*, 983 LP – 997.

Barbosa, D.J., Duro, J., Prevo, B., Cheerambathur, D.K., Carvalho, A.X., and Gassmann, R. (2017). Dynactin binding to tyrosinated microtubules promotes centrosome centration in C. elegans by enhancing dynein-mediated organelle transport. PLOS Genet. *13*, e1006941.

Bergen, L.G., Kuriyama, R., and Borisy, G.G. (1980). Polarity of microtubules nucleated by centrosomes and chromosomes of Chinese hamster ovary cells in vitro. J. Cell Biol. *84*, 151 LP – 159.

Bestor, T.H., and Schatten, G. (1981). Anti-tubulin immunofluorescence microscopy of microtubules present during the pronuclear movements of sea urchin fertilization. Dev. Biol. *88*, 80–91.

Bjerknes, M. (1986). Physical theory of the orientation of astral mitotic spindles. Science (80-.). *234*, 1413 LP – 1416.

Burgess, D.R., and Schroeder, T.E. (1977). Polarized bundles of actin filaments within microvilli of fertilized sea urchin eggs. J. Cell Biol. *74*, 1032–1037.

Chambers, E.L. (1939). The Movement of the Egg Nucleus in Relation to the Sperm Aster in the Echinoderm Egg. J. Exp. Biol. *16*, 409 LP – 424.

Costache, V., Hebras, C., Pruliere, G., Besnardeau, L., Failla, M., Copley, R.R., Burgess, D., Chenevert, J., and McDougall, A. (2017). Kif2 localizes to a subdomain of cortical endoplasmic reticulum that drives asymmetric spindle position. Nat. Commun. *8*, 917.

Culley, S., Albrecht, D., Jacobs, C., Pereira, P.M., Leterrier, C., Mercer, J., and Henriques, R. (2018). Quantitative mapping and minimization of super-resolution optical imaging artifacts. Nat. Methods *15*, 263.

David, A.F., Roudot, P., Legant, W.R., Betzig, E., Danuser, G., and Gerlich, D.W. (2019). Augmin accumulation on long-lived microtubules drives amplification and kinetochore-directed growth. J. Cell Biol. *218*, 2150–2168.

Dogterom, M., and Yurke, B. (1997). Measurement of the Force-Velocity Relation for Growing Microtubules. Science (80-.). *278*, 856–860.

Dogterom, M., Kerssemakers, J.W., Romet-Lemonne, G., and Janson, M.E. (2005). Force generation by dynamic microtubules. Curr. Opin. Cell Biol. *17*, 67–74.

Fabritius, A.S., Ellefson, M.L., and McNally, F.J. (2011). Nuclear and spindle positioning during oocyte meiosis. Curr. Opin. Cell Biol. *23*, 78–84.

Firestone, A.J., Weinger, J.S., Maldonado, M., Barlan, K., Langston, L.D., O'Donnell, M., Gelfand, V.I., Kapoor, T.M., and Chen, J.K. (2012). Small-molecule inhibitors of the AAA+ ATPase motor cytoplasmic dynein. Nature *484*, 125.

Fujita, I., Yamashita, A., and Yamamoto, M. (2015). Dynactin and Num1 cooperate to establish the cortical anchoring of cytoplasmic dynein in S. pombe. J. Cell Sci. *128*, 1555 LP – 1567.

Gönczy, P., Pichler, S., Kirkham, M., and Hyman, A.A. (1999). Cytoplasmic Dynein Is Required for Distinct Aspects of Mtoc Positioning, Including Centrosome Separation, in the One Cell Stage Caenorhabditis elegans Embryo. J. Cell Biol. *147*, 135 LP – 150.

Goshima, G., Nédélec, F., and Vale, R.D. (2005). Mechanisms for focusing mitotic spindle poles by minus end–directed motor proteins. J. Cell Biol. *171*, 229 LP – 240.

Hamaguchi, M.S., and Hiramoto, Y. (1986). Analysis of the Role of Astral Rays in Pronuclear Migration in Sand Dollar Eggs by the Colcemid-UV Method. Dev. Growth Differ. *28*, 143–156.

Harris, P., Osborn, M., and Weber, K. (1980). Distribution of tubulin-containing structures in the egg of the sea urchin Strongylocentrotus purpuratus from fertilization through first cleavage. J. Cell Biol. *84*, 668 LP – 679.

Harvey, E.B. (1933). Development of the Parts of Sea Urchin Eggs Separated by Centrifugal Force. Biol. Bull. *64*, 125–148.

Henson, J.H., Samasa, B., and Burg, E.C. (2019). High resolution imaging of the cortex isolated from sea urchin eggs and embryos. Methods Cell Biol. *151*, 419–432.

Holy, T.E., Dogterom, M., Yurke, B., and Leibler, S. (1997). Assembly and positioning of microtubule asters in microfabricated chambers. Proc. Natl. Acad. Sci. *94*, 6228 LP – 6231.

Ishihara, K., Nguyen, P.A., Groen, A.C., Field, C.M., and Mitchison, T.J. (2014). Microtubule nucleation remote from centrosomes may explain how asters span large cells. Proc. Natl. Acad. Sci. *111*, 17715 LP – 17722.

Ishihara, K., Korolev, K.S., and Mitchison, T.J. (2016). Physical basis of large microtubule aster growth. Elife *5*.

Kimura, A., and Onami, S. (2005). Computer Simulations and Image Processing Reveal Length-Dependent Pulling Force as the Primary Mechanism for C. elegans Male Pronuclear Migration. Dev. Cell *8*, 765–775.

Kimura, K., and Kimura, A. (2011). Intracellular organelles mediate cytoplasmic pulling force for centrosome centration in the Caenorhabditis elegans early embryo. Proc. Natl. Acad. Sci. *108*, 137 LP – 142.

Kotak, S., Busso, C., and Gönczy, P. (2012). Cortical dynein is critical for proper spindle positioning in human cells. J. Cell Biol. *199*, 97–110.

Kozlowski, C., Srayko, M., and Nedelec, F. (2007). Cortical Microtubule Contacts Position the Spindle in C. elegans Embryos. Cell *129*, 499–510.

Laan, L., Pavin, N., Husson, J., Romet-Lemonne, G., van Duijn, M., López, M.P., Vale, R.D., Jülicher, F., Reck-Peterson, S.L., and Dogterom, M. (2012). Cortical Dynein Controls Microtubule Dynamics to Generate Pulling Forces that Position Microtubule Asters. Cell *148*, 502–514.

Longo, F., and Anderson, E. (1968). The Fine Structure of Pronuclear Development and Fusion in the Sea Urchin, Arbacia Punctulata. J. Cell Biol. *30*.

Merdes, A., Heald, R., Samejima, K., Earnshaw, W.C., and Cleveland, D.W. (2000). Formation of Spindle Poles by Dynein/Dynactin-Dependent Transport of Numa. J. Cell Biol. *149*, 851 LP – 862.

Minc, N., Burgess, D., and Chang, F. (2011). Influence of Cell Geometry on Division-Plane Positioning. Cell *144*, 414–426.

Mooney, P., Sulerud, T., Pelletier, J.F., Dilsaver, M.R., Tomschik, M., Geisler, C., and Gatlin, J.C. (2017). Tau-based fluorescent protein fusions to visualize microtubules. Cytoskeleton *74*, 221–232.

Murata, T., Sonobe, S., Baskin, T.I., Hyodo, S., Hasezawa, S., Nagata, T., Horio, T., and Hasebe, M. (2005). Microtubule-dependent microtubule nucleation based on recruitment of γ-tubulin in higher plants. Nat. Cell Biol. *7*, 961.

Negishi, T., Miyazaki, N., Murata, K., Yasuo, H., and Ueno, N. (2016). Physical association between a novel plasma-membrane structure and centrosome orients cell division. Elife *5*, e16550.

Nguyen-Ngoc, T., Afshar, K., and Gönczy, P. (2007). Coupling of cortical dynein and Gα proteins mediates spindle positioning in Caenorhabditis elegans. Nat. Cell Biol. *9*, 1294.

Paix, A., Le Nguyen, P.N., and Sardet, C. (2011). Bi-polarized translation of ascidian maternal mRNA determinant pem-1 associated with regulators of the translation machinery on cortical Endoplasmic Reticulum (cER). Dev. Biol. *357*, 211–226.

Pavin, N., Laan, L., Ma, R., Dogterom, M., and Jülicher, F. (2012). Positioning of microtubule organizing centers by cortical pushing and pulling forces. New J. Phys. *14*, 105025.

Payne, C., Rawe, V., Ramalho-Santos, J., Simerly, C., and Schatten, G. (2003). Preferentially localized dynein and perinuclear dynactin associate with nuclear pore complex proteins to mediate genomic union during mammalian fertilization. J. Cell Sci. *116*, 4727–4738.

Peng, C.J., and Wikramanayake, A.H. (2013). Differential Regulation of Disheveled in a Novel Vegetal Cortical Domain in Sea Urchin Eggs and Embryos: Implications for the Localized Activation of Canonical Wnt Signaling. PLoS One *8*, e80693.

Petry, S., Groen, A.C., Ishihara, K., Mitchison, T.J., and Vale, R.D. (2013). Branching Microtubule Nucleation in Xenopus Egg Extracts Mediated by Augmin and TPX2. Cell *152*, 768–777.

Pollard, T.D., and O'Shaughnessy, B. (2019). Molecular Mechanism of Cytokinesis. Annu. Rev. Biochem. *88*, null.

Quintyne, N.J., Gill, S.R., Eckley, D.M., Crego, C.L., Compton, D.A., and Schroer, T.A. (1999). Dynactin Is Required for Microtubule Anchoring at Centrosomes. J. Cell Biol. *147*, 321–334.

Rappaport, R. (1961). Experiments concerning the cleavage stimulus in sand dollar eggs. J. Exp. Zool. *148*, 81–89.

Rappaport, R., and Rappaport, B.N. (1984). Division of constricted and urethane-treated sand dollar eggs: A test of the polar stimulation hypothesis. J. Exp. Zool. *231*, 81–92.

Redemann, S., Pecreaux, J., Goehring, N.W., Khairy, K., Stelzer, E.H.K., Hyman, A.A., and Howard, J. (2010). Membrane Invaginations Reveal Cortical Sites that Pull on Mitotic Spindles in One-Cell C. elegans Embryos. PLoS One *5*, e12301.

Reinsch, S., and Gonczy, P. (1998). Mechanisms of nuclear positioning. J. Cell Sci. *111*, 2283 LP – 2295.

Reinsch, S., and Karsenti, E. (1997). Movement of nuclei along microtubules in Xenopus egg extracts. Curr. Biol. *7*, 211–214.

Ren, X., and Weisblat, D.A. (2006). Asymmetrization of first cleavage by transient disassembly of one spindle pole aster in the leech Helobdella robusta. Dev. Biol. *292*, 103–115.

Roegiers, F., Djediat, C., Dumollard, R., Rouviere, C., and Sardet, C. (1999). Phases of cytoplasmic and cortical reorganizations of the ascidian zygote between fertilization and first division. Development *126*, 3101 LP – 3117.

Roossien, D.H., Miller, K.E., and Gallo, G. (2015). Ciliobrevins as tools for studying dynein motor function. Front. Cell. Neurosci. *9*, 252.

Saito, T.T., Okuzaki, D., and Nojima, H. (2006). Mcp5, a meiotic cell cortex protein, is required for nuclear movement mediated by dynein and microtubules in fission yeast. J. Cell Biol. *173*, 27–33.

Sallé, J., Xie, J., Ershov, D., Lacassin, M., Dmitrieff, S., and Minc, N. (2018). Asymmetric division through a reduction of microtubule centering forces. J. Cell Biol. jcb.201807102.

Schatten, G. (1981). Sperm incorporation, the pronuclear migrations, and their relation to the establishment of the first embryonic axis: Time-lapse video microscopy of the movements during fertilization of the sea urchin Lytechinus variegatus. Dev. Biol. *86*, 426–437.

De Simone, A., Spahr, A., Busso, C., and Gönczy, P. (2018). Uncovering the balance of forces driving microtubule aster migration in C. elegans zygotes. Nat. Commun. *9*, 938.

Song, J.-G., King, M.R., Zhang, R., Kadzik, R.S., Thawani, A., and Petry, S. (2018). Mechanism of how augmin directly targets the γ-tubulin ring complex to microtubules. J. Cell Biol. *217*, 2417 LP – 2428.

Strickland, L.I., Donnelly, E.J., and Burgess, D.R. (2005). Induction of Cytokinesis Is Independent of Precisely Regulated Microtubule Dynamics. Mol. Biol. Cell *16*, 4485–4494.

Tanimoto, H., and Minc, N. (2017). Quantitative approaches for the study of microtubule aster motion in large eggs. Methods Cell Biol. *139*, 69–80.

Tanimoto, H., Kimura, A., and Minc, N. (2016). Shape–motion relationships of centering microtubule asters. J. Cell Biol. *212*, 777 LP – 787.

Tanimoto, H., Sallé, J., Dodin, L., and Minc, N. (2018). Physical forces determining the persistency and centring precision of microtubule asters. Nat. Phys. *14*, 848–854.

Thawani, A., Stone, H.A., Shaevitz, J.W., and Petry, S. (2019). Spatiotemporal organization of branched microtubule networks. Elife *8*, e43890.

Tran, P.T., Marsh, L., Doye, V., Inoué, S., and Chang, F. (2001). A Mechanism for Nuclear Positioning in Fission Yeast Based on Microtubule Pushing. J. Cell Biol. *153*, 397 LP – 412.

Verma, V., and Maresca, T.J. (2019). Direct observation of branching MT nucleation in living animal cells. J. Cell Biol. *218*, 2829–2840.

Wühr, M., Tan, E.S., Parker, S.K., Detrich, H.W., and Mitchison, T.J. (2010). A Model for Cleavage Plane Determination in Early Amphibian and Fish Embryos. Curr. Biol. *20*, 2040–2045.

Yi, J., Wu, X., Chung, A.H., Chen, J.K., Kapoor, T.M., and Hammer, J.A. (2013). Centrosome repositioning in T cells is biphasic and driven by microtubule end-on capture-shrinkage. J. Cell Biol. *202*, 779 LP – 792.

2.5 Supplementary Figures and Legends

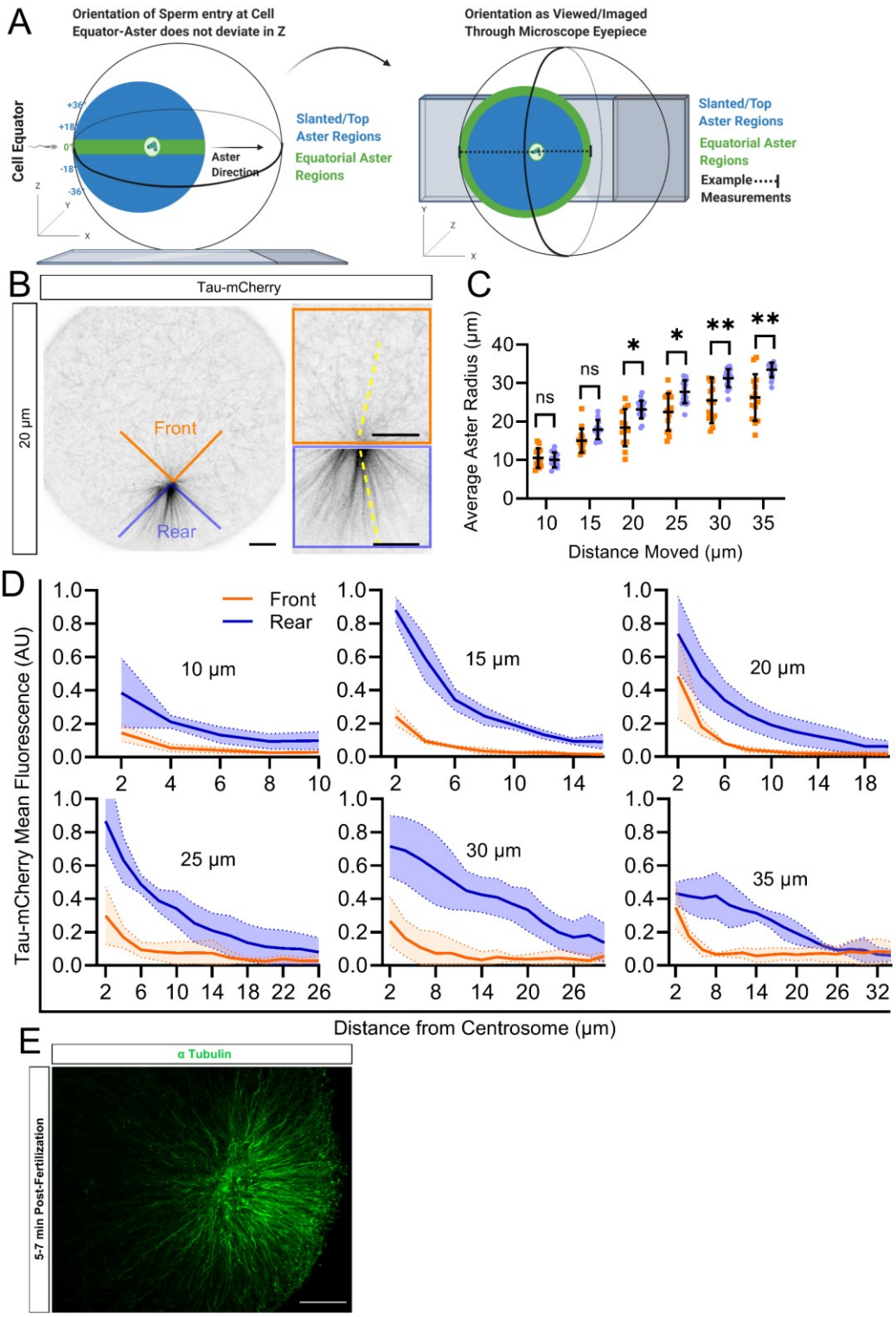

Figure S1. Additional live-cell geometry and density quantification of asters

(A) Sample orientation for live and immunofluorescence imaging and analysis. Cells were selected for imaging in which the sperm enters the egg +/- 10 μm from the egg equator along the Z-axis (Left cartoon). The sperm aster migrates along the cell equator, without deviating in Z, toward the cell center. By orienting the cell and sperm aster in this way, any slanted MTs in the Z-axis (Blue Regions) are defined as top and bottom portions of the sperm aster. Conversely, equatorial portions of the sperm aster (Green Regions) in front and behind the MTOC are defined as front and rear radii, respectively. Due to the spherical geometry of the aster, these front and rear equatorial radii represent the longest portions of the aster in the front and rear, respectively. We quantify the average maximum distance from the MTOC in front and rear equatorial portions using maximum intensity Z-projections of immunofluorescence images (Right Cartoon and Figure 1C-1D). This orientation allows us to exclude slanted top/bottom portions from our measurements because they do not reach the maximum radii of the sperm aster in front and rear equatorial portions (Right Cartoon, maximum boundaries are Green Equatorial Regions). In our live imaging, we use a single Z-plane through the MTOC of the sperm aster (Green Equatorial Region). The top and bottom portions of the sperm aster exit this Z-plane (Blue Regions), excluding them from our analysis (in reference to Figures 1A-1B and S1B-S1C).

(B) and (C) Tau-mCherry signal from zygotes imaged in Figure 1A and 1B. Tau-mCherry labeled MTs were measured from their most distal ends to the MTOC (yellow dashed line) in front (orange) and rear (blue) portions of the aster and averaged (Lfront and Lrear, respectively). Average Lfront and Lrear was calculated at time points in which the aster had moved 10, 15, 20, 25, 30, and 35 μm from the point of sperm entry (B). Data represent mean ± SD (n=16 zygotes), *P<.05, **P<.01, 2-way ANOVA with Sidak's multiple comparisons. See also Movie S1

(D) Densities of front and rear portions of the aster measured by Tau-mCherry mean fluorescence using the same ROI as in (A), as a function of distance from the centrosome. Fluorescence intensity is normalized to the MTOC for all data points (see materials and methods for more info.). Data represent the mean, shaded regions represent ± SD (n=9). P<.01

(E) Representative structured illumination microscopy image of the sperm aster ~10 minutes post-fertilization. Image represents a Z-stack of 50 μm 3D volume at 0.5 μm. intervals converted to a maximum intensity projection.
Scale bars, 10 μm throughout.

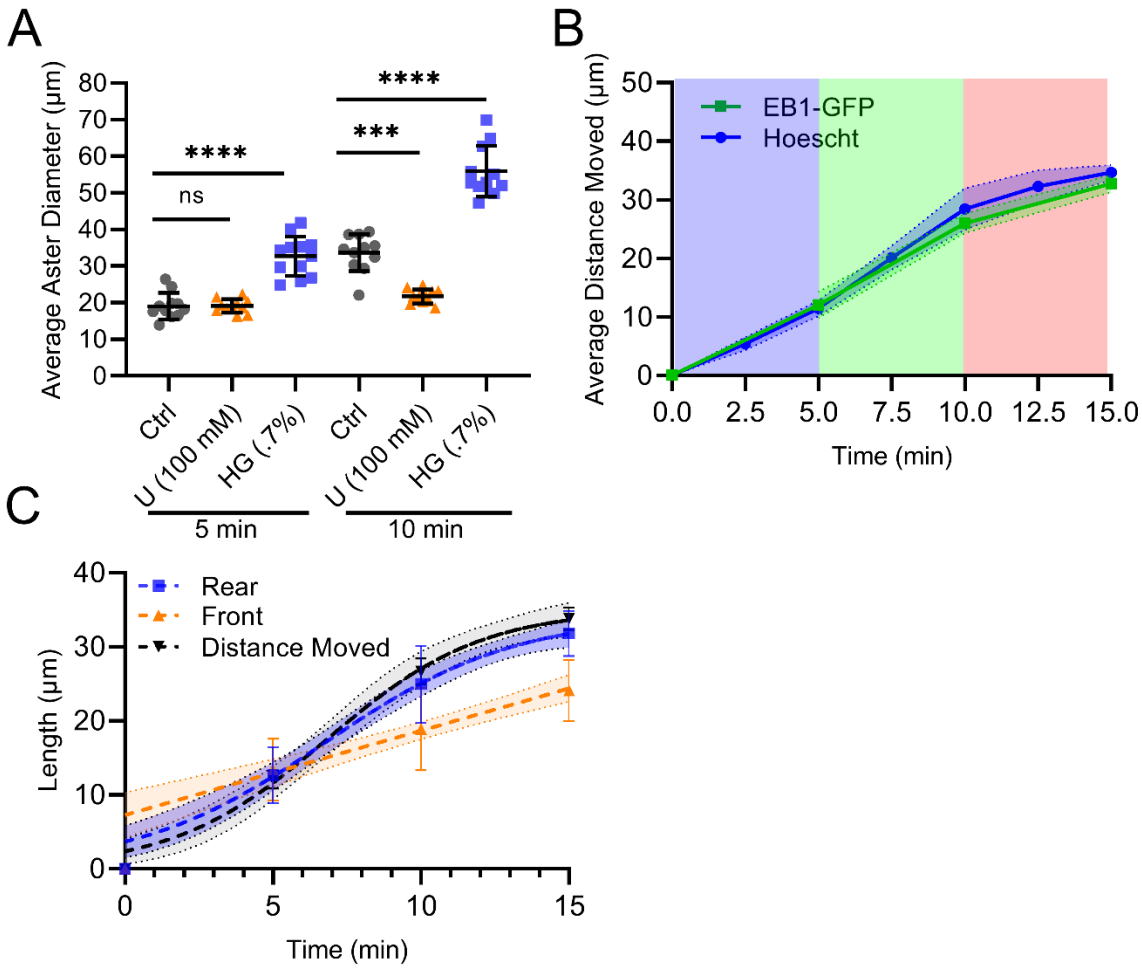

Figure S2. Additional analysis of aster diameters, migration dynamics, and comparison of migration dynamics with aster lengths

(A) Aster diameters in different conditions quantified from z-stacks of fixed immunofluorescence images of zygotes represented by Figure 2A. ***P<.001, ****P<.0001 2-way ANOVA with Tukey's multiple comparisons test. Each shape is the diameter of an individual aster. Data are represented as the mean, ± SD (n=11 zygotes).

(B) Comparison of average distance moved over time in control zygotes tracked by either the MTOC (EB1-GFP) or the male pronucleus (Hoescht labelling). Solid lines represent the mean, shaded areas ± SD (n=13 zygotes per condition). Each shaded area represents a region with a different slope/migration speed (2.29 +/-.09 µm, 4.8 +/- 2 µm, and 1.250 +/- .25 µm for blue, green, and red regions respectively). Statistical difference of the slopes was determined by a ANCOVA, P<.0001

(C) Comparison of aster migration rates with aster geometry. Shapes represent the mean Lfront, Lrear, and distance moved for n=12 zygotes (Orange, blue, and black shapes, respectively). Dotted lines correspond to the best fit logistic regression curves for each parameter. Distance moved and Lrear, R^2 of .803 and .984, respectively (P<.001). Lfront, R^2 of P=.84 (ns). Shaded areas represent 95% confidence interval.

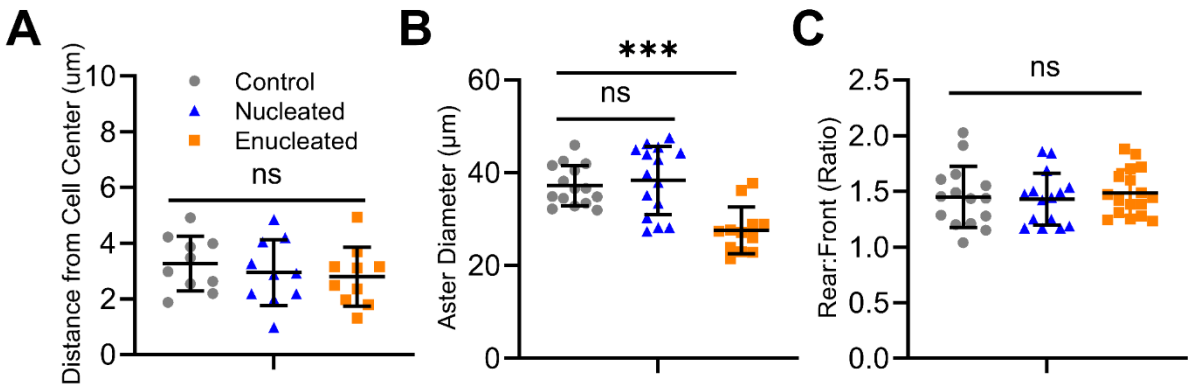

Figure S3. Characterization of Centration and Aster Geometry in Centrifuged enucleated and nucleated zygotes

(A) Quantification of male pronuclear distance from the center of the zygote based on live-cell imaging of the male pronucleus (See Movie S3). The distance is not significantly different between non-centrifuged controls (gray circles), full-sized/nucleated centrifuged eggs (blue triangles), and enucleated centrifuged egg-halves (orange squares). One-way ANOVA, p>.5. Error bars represent SD (n=10 zygotes per condition)

(B) Average aster diameter of asters using the same conditions as in **(A)** based on immunofluorescence maximum intensity projections of sperm asters ~ 10 minutes post-sperm addition (See Figure 3D). Note aster diameter from non-centrifuged and full-sized/nucleated centrifuged eggs are not significantly different (p=.856, One-way ANOVA), while asters from smaller enucleated halves are significantly smaller (*** p>.0001, One-way ANOVA). Error bars represent SD (n=15 zygotes per condition). See STAR Methods for diameter measurement methods.

(C) Rear:Front aspect ratio of sperm asters using the same conditions as in **(A)** and **(B)** based on immunofluorescence maximum intensity projections of sperm asters ~10 minutes post-sperm addition. For all three conditions the Rear:Front aspect ratio is ~1.5, indicating that aster shape with regards to front and rear portions are not altered by centrifugation and enucleation. One-way

ANOVA, p>.8. Error bars represent SD (n=15 zygotes per condition). See Star Methods for aspect ratio quantification methods.

Supplementary Movies

Movie S1. Live cell microscopy of MTs and MT plus-ends within the sperm aster using Tau-mCherry and EB1-GFP, respectively. The movie represents combined videos from 6 different time points during aster migration. Corresponds to Figures 1A-1B and Figure 1E. Scale bars, 10 μm.

Movie S2. Live cell microscopy of Tau-mCherry and EB1-GFP co-labeled sperm asters in control, urethane, and HG-treated zygotes. The movie represents combined videos from 3 different time points during aster migration. Corresponds to Figure 2. Scale bars, 10 μm.

Movie S3. Live cell microscopy of pre-centrifuged zygotes (control, urethane treated, and enucleated) stained with hoescht to visualize and track pronuclei. Corresponds to Figure 3. Scale bars, 10 μm.

Movie S4A. Live cell microscopy of Tau-mCherry-labeled sperm asters treated with 50 μM of ciliobrevin D. Ciliobrevin was added just before imaging began. Corresponds to Figure 4B. Scale bars, 10 μm.

Movie S4B. Live cell microscopy of control Tau-mCherry-labeled and p150-CC1:Tau-mCherry co-injected zygotes. Scale bars, 10 μm.

Movie S5A. Chemical ablation of rear, cortical facing astral MTs with UV-inducible CA4. Red line marks region of UV activation. Scale bars, 10 μm.

Movie S5B. Chemical ablation of side (top) and front portions of the sperm aster with CA4. Red line marks region of UV activation. Scale bars, 10 μm.

Chapter 3. Preliminary Data and Outlooks

3.1 Potential Size-Scaling for Aster Size Determination

Abstract

Microtubule (MT) asters coordinate spatial organization in a wide variety of cell shapes, sizes and cell cycle states. During development in non-parthenogenetic animals, microtubule (MT) sperm asters grow as they migrate to the cell center, a process essential to determining the first cleavage plane. Within the extremely wide range of egg volumes across organisms, sperm asters display diverse sizes, which appears to be critical in determining the force generating mechanisms required for centration. Despite this fundamental importance, the regulatory mechanisms responsible for aster size determination are largely unknown. Here we monitor aster size using the interphase sperm aster of the sea urchin zygote. Manipulations of egg size through centripetal force indicates that aster size during defined time points of migration directly scales with egg size. Despite smaller zygote and aster size, centration still occurs in the same time period compared to full-sized zygotes, which suggests that migration rates are also slower. Together, our data provide evidence that aster growth and migration rates scale with cell size.

3.1.1 Introduction

Cells display remarkably diverse sizes across organisms, tissue types, and developmental states. Accordingly, intracellular organelles and structures must also scale with cell size in order to ensure proper cellular function. This process, known as organelle size scaling, has been particularly well studied during successive rounds of division during development (Wesley et al., 2020 for a recent review). For example, centrosomes, mitotic

spindles, and nuclei have been shown to scale to cell size during reductive divisions of the early embryo (Conklin, 1912; Decker et al., 2011; Good et al., 2013; Hazel et al., 2013; Lacroix et al., 2018; Mukherjee et al., 2020). There are currently two models for how the size of these organelles scales with cell size. The first is a limiting pool model in which there are limiting amounts of size regulatory factors homogenously distributed throughout the cytoplasm (Goehring and Hyman, 2012). As cells become smaller through division, the total amount of these factors becomes smaller, reducing organelle size. Alternatively, temporally controlled regulators are hypothesized to reduce organelle size depending on developmental and/or cell cycle stages (Goehring and Hyman, 2012). Distinguishing between these two models has been a major challenge, as both cell volume and developmental regulation change as embryos undergo rounds of division.

While many recent studies have focused on the changes in organelle size and regulation during reductive embryonic division, less attention has been given to organelle size prior to division. One striking instance, is the variation in egg sizes across different species and in some cases, within the same species (Chambers, 1909). Immediately after fertilization, spatial organization of the egg undergoes marked changes, which results in newly formed structures and organelles. As such, these structures and organelles must scale with the size of the egg to ensure accurate union of gamete chromosomes and cell division (West and Brown, 2005). The sperm aster, nucleated from a sperm-derived MT organizing center (MTOC), is one such structure that is essential to these processes, as it migrates and transports male and female pronuclei toward the cell center. The size and growth dynamics of sperm asters differs dramatically across model organisms (Meaders and Burgess, 2020). These variations are also accompanied by differences in how asters generate and respond to the forces required during migration. While aster size and growth

dynamics are essential to development, the fundamental principles governing sperm aster size are still unknown.

The sea urchin egg represents an ideal *in vivo* system for studying sperm aster size regulation. Sperm aster growth and migration dynamics are highly consistent in this system (Chambers, 1939; Tanimoto et al., 2016) and occur during a 15-20 minute interphase time period, which prevents difficulties interpreting data in the context of changing developmental and cell cycle cues. Furthermore, the extremely malleable nature of the egg makes it possible to experimentally increase and decrease egg size through multiple methods (Bennett and Mazia, 1981). We take advantage of these features and show that when we decrease egg diameter, asters still migrate to the cell center in the same amount of time as full size control eggs. By using immunofluorescence microscopy, we find that asters are smaller in these eggs, and aster size directly scales with a reduction in cell size. Together, this data set provides strong preliminary evidence that aster size is fundamentally determined by cell size.

3.1.2 Results

By centrifuging eggs prior to fertilization, we were previously able to break them into two separate cells, one of which contains the female pronucleus and the other being enucleated (Chapter 2, Figure 3). When we fertilized these smaller eggs, sperm aster growth results in centration timing that is comparable to full sized eggs. However, our previous study revealed that while aster geometry was unaffected, diameter in these smaller eggs was significantly decreased, even though small and full sized eggs were fixed at the same time point after fertilization (Figure 1A and 1B). This comes as a surprise

because aster size and geometry is highly consistent at defined time-points after fertilization (Chapter 2). Instead this change in aster size suggests that growth of these interphase sperm asters are regulated by cell size, a hallmark of organelle size scaling.

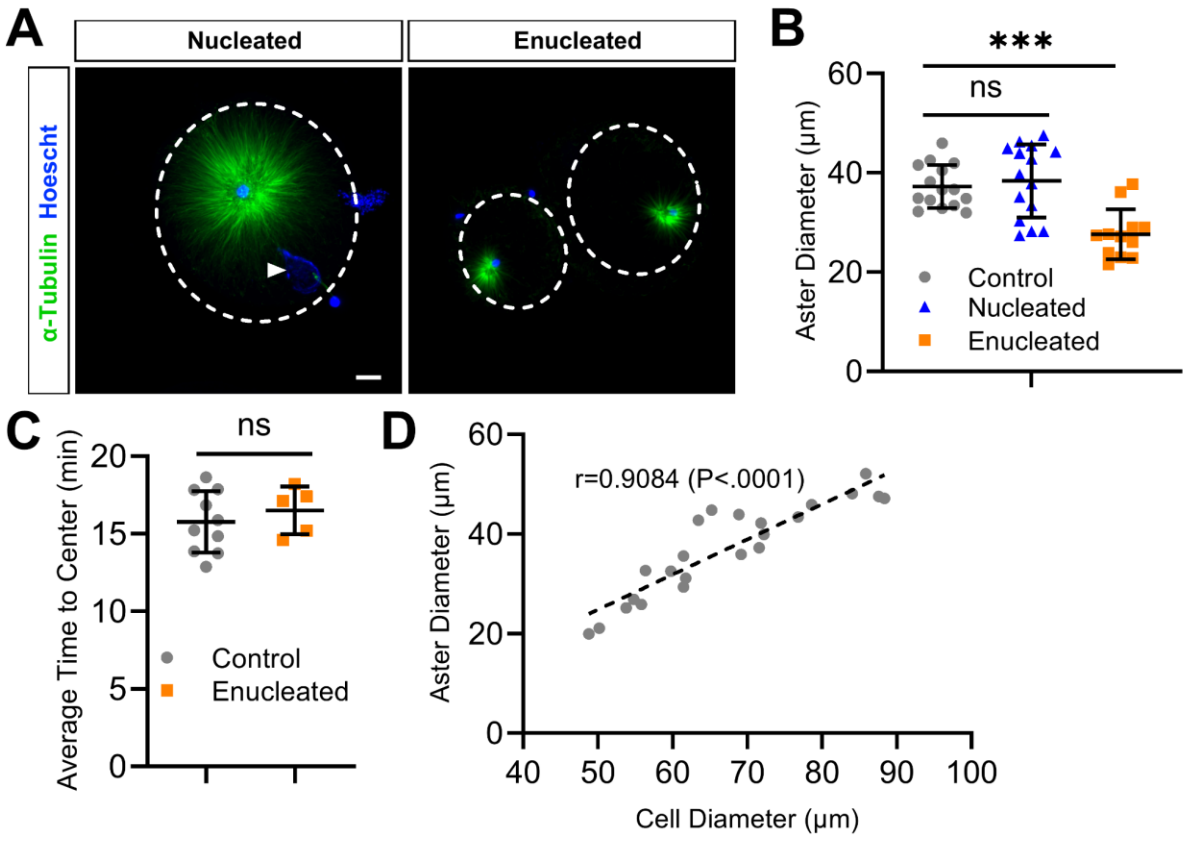

Figure 1. Comparison of aster diameter and centration timing with cell diameter

(A). Fixed immunofluorescence 3D projections of sperm asters in centrifuged zygotes repurposed from experiments conducted in Chapter 2 (Figure 3D). Centrifuging the eggs at higher rates (see Chapter 2.4 for methods) causes them to split, resulting in nucleated (left image) and enucleated halves (right image) of different sizes. Eggs were fixed at 10 min post-sperm addition, so time points during aster migration are approximately the same. Arrow head marks the female pronucleus in a nucleated zygote. Scale bar, 10 µm

(B) Average aster diameter of asters using the same conditions as in **(A)** based on immunofluorescence maximum intensity projections of sperm asters ~ 10 minutes post-sperm addition. Control zygotes are non-centrifuged, nucleated zygotes are centrifuged, full-sized zygotes, and enucleated are split zygotes of different, but smaller sizes compared to controls. Note aster diameter from non-centrifuged and full-sized/nucleated centrifuged eggs are not

significantly different (p=.856, One-way ANOVA), while asters from smaller enucleated halves are significantly smaller (*** p>.0001, One-way ANOVA). Error bars represent SD (n=15 zygotes per condition). Diameter measurement methods are provided in Chapater 2.4 STAR Methods.

(C) Average time to centration between full-sized centrifuged eggs and eggs centrifuged at a higher speed to split and enucleated them. Note enucleated eggs are a smaller diameter (see Materials and Methods 3.3 for measurement details). Average centration timing was compared using and Unpaired t test (P=.4774, ns). n=10 zygotes for controls, n=5 zygotes for enucleated. Error bars represent SD.

(D) Sperm aster diameter plotted as a function of cell diameter in eggs centrifuged at rates/times that split them into various sizes. Analysis was performed on sperm asters ~10 minutes post fertilization. See Materials and Methods 3.3 for diameter measurement details. Diameters were compared using Pearson's correlation (r=.9084, P=.0001, n=23 zygotes), indicating a strongly linear associated between aster diameter and cell diameter. Hashed line represents Linear regression of the data, with a slope of .7050.

To further investigate this possibility, we first asked if the sperm aster is centering on the same time scale as full sized eggs. Sperm asters have a much smaller distance to the cell center in these smaller eggs, and therefore we hypothesize that equal migration rates in smaller cells would result in earlier centration when compared to full-sized cells. Conversely, if aster growth and size is scaling to cell size, we hypothesize that migration rates will also decrease, resulting in centered sperm asters at similar time points post-fertilization as full-sized eggs. We measured the time required for asters to reach the approximate cell center (see Materials and Methods) in full-sized and split eggs. We find that centration timing is highly comparable between both conditions (Figure 1C), indicating that migration rates of sperm asters in smaller eggs is decreased.

To directly address if aster size is scaling to cell size we plotted estimated aster diameter as a function of cell diameter in halved and full sized eggs at ~10 minutes post-fertilization. Because centrifugation of eggs at high speed results in eggs which do not split perfectly

in half, we were able to acquire a data set of eggs in a nearly 2-fold range of diameter (Figure 1D). We find that as egg diameter increases or decreases, aster diameter scales accordingly with a strong linear correlation (.9084 Pearson correlation, P<.0001). Importantly, data points include eggs nucleated or enucleated prior to fertilization, indicating that the female pronucleus does not have an effect on sperm aster size scaling or migration. Together, these data provide strong preliminary evidence that interphase sperm aster growth rates, size, and migrations rates scale with cell size to ensure tightly regulated centration timing in eggs of differing sizes.

3.1.3 Discussion and Conclusions

While we provide one method to change cell size and find that aster diameter and migration rates directly scale (Figure 1C and 1D), there are still several key experiments required to adequately test our hypothesis. First, what happens when we increase cell size beyond control averages? Sea urchin eggs can be fused together, resulting in much larger sizes. Furthermore, these eggs can also be fertilized and develop well past the first cell stage, suggesting that aster centration and first cleavage proceed normally (Bennett and Mazia, 1981). Additionally, fusing an enucleated half of a particular size to a full size, non-centrifuged egg, gives us some control over exactly how much volume we add to the egg, while at the same time preventing artificial introduction of two female pronuclei. Second, while aster size and geometry appears unaffected by the centrifugation process (Chapter 2, Figure S3B and S3C), a more direct way to control for potential artifacts is by manually cutting eggs into smaller portions using a glass knife (Mukherjee et al., 2020). This second iteration of reducing cell size will prove valuable when confirming whether or not aster sizes directly scale to cell size.

A second question to address is how cell size regulates aster size. Because sea urchin sperm asters migrate during interphase of the first developmental cell cycle, it is very unlikely that time-dependent developmental cues are affecting size scaling. Therefore, we favor a limiting pool model in which size regulating factors are reduced/increased when cell size is reduced/increased, respectively (Goehring and Hyman, 2012). A more obvious candidate for this factor is soluble tubulin itself. Much like during spindle size scaling (Lacroix et al., 2018), we predict that the amount of tubulin, through dynamic instability (Mitchison and Kirschner, 1984), may be regulating aster size. One simple method to test this hypothesis is by inducing polyspermy. In this condition, multiple asters will form, resulting in less total tubulin available for each MTOC to nucleate an aster. We hypothesize this will result in increasingly smaller asters at defined time points, dependent on how many sperm asters are present in a given cell. For example, three sperm asters would be overall smaller than two sperm asters, and so on in a given cell. A way to further test this model in polyspermic eggs will be to destroy one or multiple MTOCs either through laser ablation, and measure aster growth dynamics of the remaining aster(s), which will conceptually increase soluble tubulin to fuel growth of the remaining aster. In a limiting pool model, we hypothesize that the remaining asters will display increased growth rates and therefore size after removal of one or more aster(s).

Finally, our model of aster size scaling offers an attractive explanation for how the sperm aster size scales across eggs of incredibly diverse sizes. This explanation also isn't limited to differences between organism. For example, frog eggs from an individual female can range in sizes from ~1 mm to 1.8 mm in diameter (Chambers, 1909). Our model of size scaling accounts very well for how eggs differing in size of this magnitude may ensure tightly regulated timing of pronuclear union and centration with the first mitotic division. This idea is well supported by our data in the sea urchin showing that smaller eggs result

in centration timing that is strikingly comparable to full sized eggs (Figure 1C). Collectively, our hypothesis predicts that sperm aster size scaling may allow centration to be tightly coordinated with developmental and cell cycle clocks during very early development.

3.2. Evidence for Microtubule Branching within the Sperm Aster

Abstract

We previously show that a pushing mechanism is essential and sufficient to drive migration of large microtubule (MT) sperm asters in the sea urchin zygote. The exact nature of such a mechanism is unclear, especially given the wealth of data indicating that centration of large MT structures is not feasible due to buckling and slipping of long MTs. To solve these physical issues during centration of large asters, we proposed a hypothesis in which the sperm aster may nucleate according to a collective growth model, or MT-dependent MT nucleation, which can account for both MT branching and bundling. Here we begin testing this hypothesis in sea urchin sperm asters using standard confocal combined with super resolution microscopy. We find in both live and immunofluorescence imaging, density of the sperm aster as a function of distance from the MT organizing center (MTOC) is conceptually consistent with a collective growth model. Additionally, we identify potential branch points in sperm and mitotic asters using two different methods of super resolution microscopy. Together, these data provide preliminary support that sperm aster morphology may be consist with branching and/or bundling, which may provide a mechanistic explanation for how large asters are pushed during migration.

3.2.1 Introduction

MT polymerization against the cortex is sufficient to push MTOCs to the correct location *in vitro* and in smaller cell types such as fission yeast (Tran et al., 2001). Our previous data identifying a similar mechanism in large (~100 um diameter) sea urchin zygotes comes as a surprise because previous work has shown that as MTs polymerize to greater lengths, force loss during pushing can occur due to MT slippage along the cortex and MT buckling (Dogterom and Yurke, 1997; Holy et al., 1997). Indeed, to the best of our knowledge, pulling along front astral MTs by dynein at the cortex or in the cytoplasm were previously the only reported mechanisms for sperm aster positioning in large zygotes. Therefore, the question of how a large microtubule structure, such as the sperm aster, may be pushed during migration remains unanswered.

Recent *in vitro* and theoretical studies have challenged the radial elongation, or standard model for aster growth, suggesting that asters are composed of interconnected, branching MTs as a result of centrosome-independent MT nucleation (Ishihara et al., 2014, 2016; Petry et al., 2013). We predict that this updated model for aster growth and morphology, coined the collective growth model (Ishihara et al., 2014), could serve as a potential mechanism to prevent MT buckling and slipping as many shorter MTs would grow against the cortex rather than as long individual MTs. However, to date, MT branching has only been observed *in vivo* in one model organism (Verma and Maresca, 2019). Using *Drosophila* S2 cells, (Verma and Maresca, 2019) show that mitotic asters reaching the cortex branch through MT-dependent MT nucleation. Whether or not MT branching and/or bundling occurs in other systems, cell types, and cell cycle states is completely unknown.

Much of the ongoing research in the field is instead focused on the regulatory mechanisms and pathways required for MT branching and bundling *in vitro* (Alfaro-Aco et al., 2017, 2020; Basnet et al., 2018; King and Petry, 2020; Thawani et al., 2019). A series of

influential studies using Xenopus extracts have shown that step-wise branching pathways begin with γ-tubulin deposition on the side of a parental MT, through recruitment by centrosome independent MT nucleation factors called Augmin and TPX2 (Alfaro-Aco et al., 2017; Petry et al., 2013; Song et al., 2018). γ-Tubulin then nucleates a daughter MT from the side of the parental MT, resulting in a branching MT architecture. Likewise, this same pathway was recently shown to be responsible for MT bundling during MT-to-kinetochore guidance in mammalian tissue culture (David et al., 2019). In this sense, MT bundling can be thought of as branching of new MTs at a 180-degree angle from parental MTs.

Importantly, a branched aster MT architecture was recently shown in extracts from *Xenopus* eggs to account for MT density that does not decrease as distance from the MTOC increases (Ishihara et al., 2016), which is inconsistent with an expected reduction in MT density proposed by the standard radial elongation model (Bergen et al., 1980). Here we investigate these characteristic of MT branching/bundling within the sperm aster of the sea urchin zygote. By measuring density of the aster as function of distance from the MTOC in live cells injected with EB1-GFP, we find that density is not fully maintained, but also only displays a minor decrease as MTOC distance increases. Additionally, we label γ-tubulin using immunofluorescence confocal microscopy and find it distributed throughout the sperm aster, rather than confined to the MTOC. Finally, in an attempt to directly detect branching and/or bundling we utilized two methods of super resolution fluorescence microscopy to visualize the sperm aster: structured illumination microscopy (SIM) and super resolution radial fluctuations microscopy (SRRF). Both of these methods yield asters that display signs of potential MT-dependent MT nucleation with thin the sperm aster. Together, this data provides preliminary evidence for collective growth rather than radial elongation during sperm aster growth in the sea urchin zygote.

3.2.2 Results

In a standard/radial elongation model, MT density should decrease as a function of distance from the MTOC, while in a branched/collective growth model MT density should be maintained at increasing distances from the MTOC (Ishihara et al., 2014, 2016). We took advantage of this discrepancy in our previous study (Chapter 2) and measured MT density as a function of distance from the MTOC at six different time points after fertilization in the sea urchin sperm aster. While our original objective was to compare density between front and rear portions of the sperm aster, we acquired applicable density curves as a function of distance from the MTOC in front and, more importantly, rear portions of the aster where we hypothesize MT-dependent MT nucleation to allow MT-based pushing forces against the rear cortex. In live-cell fluorescence microscopy of sperm asters labeled with EB1-GFP, we observe a sharp decrease in MT density just beyond the MTOC, which likely represents a difference in fluorescence intensity between the MTOC and astral MTs (Figure 2A). As distance from the bright MTOC increases, we find that aster density becomes much more evenly distributed, but still displays a minor decline.

Next, we aimed to determine if MT branch nucleation factors are present throughout the sperm aster. To this end we labeled γ-tubulin in eggs fixed ~10 post sperm addition. In a standard/radial elongation model, we expect γ-tubulin to be restricted to the MTOC, as MTs are thought to nucleate solely from the MTOC. Conversely, in a collective growth model, we expect γ-tubulin to be at the MTOC and distributed throughout that sperm aster where it would be nucleating branched MTs. In maximum intensity projections of sperm

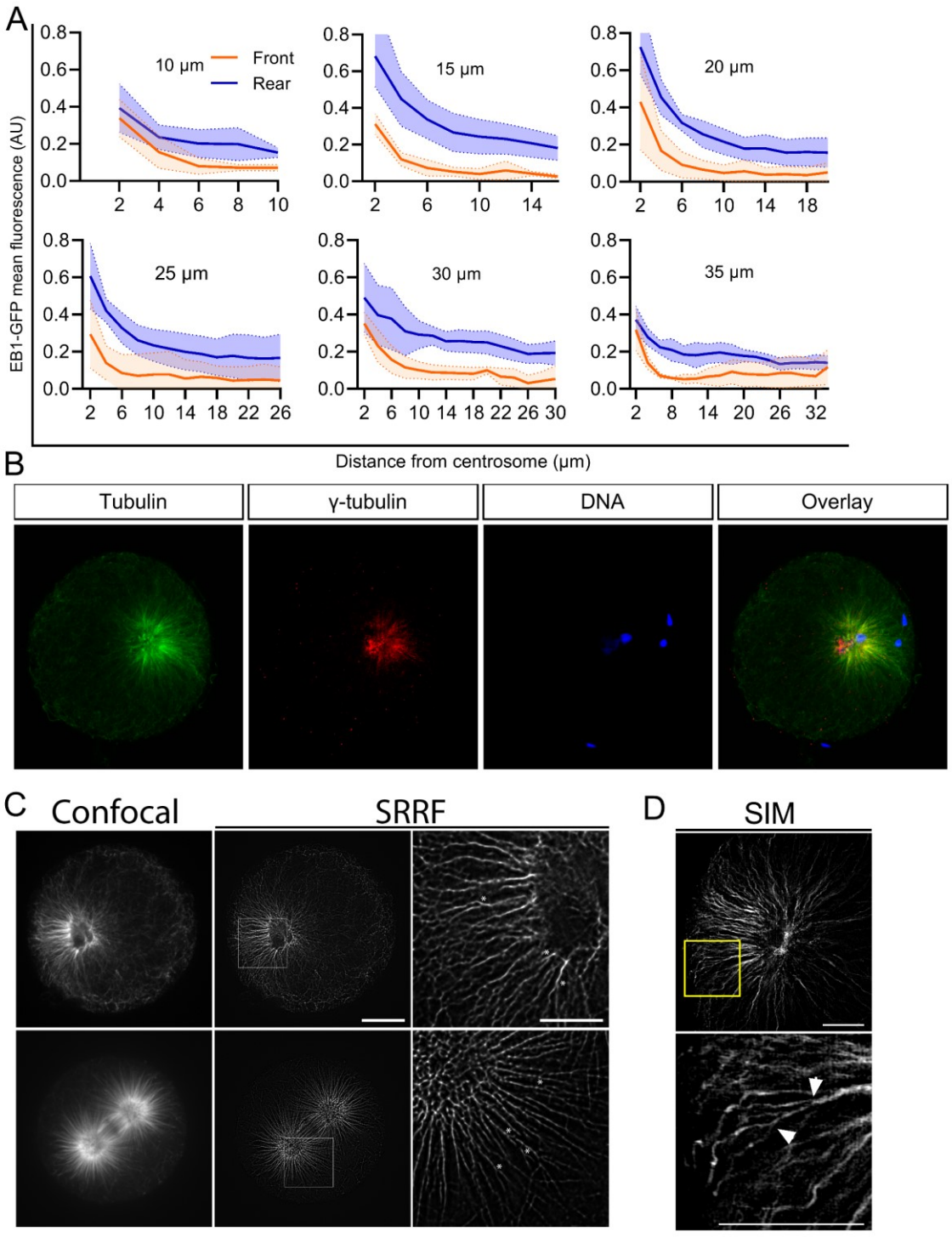

Figure 2. Evidence for MT-dependent MT nucleation within the sperm aster

(A). Data is repurposed from Chapter 2.2.1, Figure 1E. Quantifications of average EB1-GFP densities as a function of distance from the MTOC (2 µm intervals) in front and rear portions of the aster at the indicated migration distances from the site of sperm entry. Intensity profiles were

corrected for background and non-astral EB1-GFP signal and normalized to the fluorescence intensity of the MTOC (see Star Methods Chapter 2.4.3 for additional info.) Shaded areas represent ± SD. P<.01, 2–way ANOVA with Sidak's multiple comparisons, n=9 zygotes.

(B) Immunofluorescence max. intensity z-projections of γ-tubulin distribution throughout the sperm aster. Asters are from cells fixed ~10 minutes post fertilization. γ-tubulin is localized to the MTOC and throughout the astral array.

(C) SRRF microscopy of a single z-plane in sperm asters (fixed ~10 minutes post fertilization) and the mitotic spindle. Insets (right column) are zoomed images outlined by the white boxes (middle column). Asterisks mark potential branch points within the rear sperm and peripheral spindle asters. Scale bars, 20 μm

(D) SIM microscopy of a single z-plane containing the sperm MTOC, fixed ~10 minutes post fertilization. Lower image is a zoomed inset outlined by the yellow box in the top image. Arrow heads mark potential MT branching along the rear portion of the sperm aster. Scale bars, 10 μm

asters, we find γ-tubulin at the MTOC and heavily distributed throughout the sperm aster (Figure 2B). While we have yet to test the specificity of our γ-tubulin antibody, this localization is consistent with a collective growth model for sperm aster morphology.

To better resolve the morphology of MT arrays within the sperm aster we used structured illumination microscopy (SIM) and, in a collaborative effort with Brad Shuster's lab, super resolution radial fluctuations (SRRF) microscopy. Asters were oriented using our methods from our previous study (Chapter 2) in order to define front and rear portions of the sperm aster. Both super resolution imaging methods qualitatively yield asters containing potential branch points (Figure 2C and 2D). That is, sperm asters appear more like a dense network of MTs, notably in the rear portion of the sperm aster, rather than straight, radially elongated MTs expected by the standard model for aster growth. Furthermore, we observe potential branch points in mitotic asters during the first cell division (Figure 2C). While we cannot yet conclude that these are authentic branch points without using a marker for

branching (i.e. TPX2 or Augmin), these experiments lay the ground work for more elaborate investigations of MT-dependent MT nucleation within the sea urchin sperm aster.

3.2.3 Discussion and Conclusions

While MT branching in animal models has recently been an area of intense investigation *in vitro* (Alfaro-Aco et al., 2017, 2020; Basnet et al., 2018; King and Petry, 2020; Thawani et al., 2019), identification of branched MTs *in vivo* is notably limited to a single study in one system (Verma and Maresca, 2019). Thus, it is of fundamental importance to determine the extent of which MTs branch *in vivo* and how well this MT morphology is conserved across model organisms. Moreover, while much of the experimental focus is on determining the pathways and characteristics of branching, very little is known about a function for MT-dependent MT nucleation.

In the sea urchin sperm aster, we hypothesize that MT-dependent MT nucleation functions to circumvent the previously proposed limitations to a pushing model during positioning of large MT structures (Dogterom and Yurke, 1997; Holy et al., 1997). Here we have begun investigations to determine if the sperm aster is characterized by a branched and/or bundled MT morphology. We show qualitatively that sperm aster morphology appears as a potentially branched network of MTs rather than long individual MTs expected in a standard model for aster growth. However, it is still unclear if this morphology is due to crosslinking of MTs or simply an artifact of fixation. Evidence for the latter comes from our live-cell imaging of EB1-GFP in Chapter 2. In these movies, we observe a more radial morphology within the sperm aster. Moreover, in rear portions of the sperm aster constant

streaming of EB1-GFP comets creates a “waterfall” pattern of plus-end growth that is comparable with Augmin-dependent MT bundling observed K-fibers of mammalian mitotic spindles (David et al., 2019). Additionally, the minor decline we see in aster density as distance from the MTOC increases is a phenotype that falls in between what’s expected for a branching model and a standard growth model, which may be indicative of a bundled aster MT morphology. Therefore, it is still unclear whether or not the sperm aster grows with branched and/or bundled morphology. Modelling what density curves at various distances from the MTOC in a branched, bundled, or hybrid model, and making comparisons with our experimental curves will help clarify these discrepancies.

We also show that γ-tubulin is widely distributed throughout the sperm aster (Figure 1B). While we cannot yet rule out that this is non-specific staining, this localization is consistent with its function as a branched MT nucleation factor (Song et al., 2018). Determining whether or not our γ-tubulin antibody is specifically labelling γ-tubulin puncta along astral MTs is complicated by the fact that removal of γ-tubulin will also likely remove the sperm aster. Therefore, future live-cell experiments injecting fluorescently labeled Augmin and/or TPX2, both of which are conserved in the sea urchin (Kanehisa, 2019; Kanehisa and Goto, 2000; Kanehisa et al., 2019), will be integral experiments when determining whether or not branching/bundling occurs within the sea urchin.

3.3 Materials and Methods

Microscopy

Fixed MT and γ-tubulin imaging with standard confocal microscopy

To image DM1A-labeled α-tubulin in whole zygotes, imaging was performed on a laser point scanning confocal microscope (Zeiss 880 Airyscan), controlled by Zen Black software with a 40x

1.1 NA water immersion objective. 3D volumes (40 µm, composed of 20 z-sections at 2 µm intervals) were acquired for each sample to ensure the entire aster (Figures 1A) was acquired in each data set. Only zyogtes in which the centrosomes were +/- 10 µm from the cell equator were imaged in order to ensure front and rear portions of the aster could be defined.

Live pronuclei imaging

Eggs and sperm were incubated with Hoescht at a final concentration of 1 ug/ml to allow staining of male and female pronuclei. Eggs were then added to glass bottom dishes (35 x 10 mm) and allowed to settle to minimize movement during imaging. Hoescht-labeled pronuclei were imaged using a Leica SP5 LSM, controlled by LAS AF software, with a 40x 1.1 NA water immersion objective and a 405 nm UV laser. Zygotes in which the sperm entered +/- 10 µm from the cell equator were chosen for imaging to reduce the 3D volume required to capture the entire pronuclear migration process. 3D volumes of 40 µm at 2 µm intervals were acquired every 10-15 seconds from sperm penetration until male pronuclear centration was complete. Deviations of the male pronucleus in the z-axis were rare and excluded from the analysis.

Structured illumination and super resolution radial fluctuation microscopy

SRRF images of sperm asters were performed by Brad Shuster and Leslie Toledo. Zygotes were fixed as described below and imaged on an Andor Dragonfly spinning disc confocal microscope driven by Andor Fusion software. Standard confocal and Super Resolution Radial Fluctuation (SRRF) images were acquired with an Andor iXon 888 EMCCD camera. SRRF images were generated by acquiring 100 frames with a ring radius of 1.5 pixels. To ensure that any branch points were not due to artifact, SRRF images were processed using Nano-J SQUIRREL, which compares super resolution images with a standard confocal or wide-field reference image to quantitatively map artifacts generated by the super resolution technique (Culley et al., 2018)

SIM images of sperm asters were acquired on an Elyra 880 (Zeiss) platform. Images shown were acquired using a 60x 1.4 NA oil immersion objective. AlexaFluor 488 conjugated primary antibody (see below) was excited using a 488 nm laser line combined with a 495-550 nm emission filter. For

3D imaging the grating pattern was rotated 5 times. Raw images were reconstructed using the Zeiss Zen Black software SIM tool. The resulting reconstructions consist of z-stacks with .11 micron slice spacing measuring a total of 11.88 microns in depth.

Method Details

Immunostaining

Whole-cell zygotes were fixed and permeabilized in bulk (1.5 ml Eppendorf tubes) at the indicated time points (Figures 1C and 4A) using a fixation buffer composed of 100 mM Hepes (pH 7.0), 50 mM EGTA (pH 7.0), 10 mM MgSO4, 400 mM dextrose, 2% formaldehyde, and .2% Triton-X. Samples were incubated for 1 hr at room temperature with gentle agitation, rinsed 3X with (PBST) and left to sit overnight in PBST. We blocked samples in 5% BSA/PBST for 2 hrs at room temperature on a rocker. Samples were then transferred to Alexa-488 conjugated DM1A alpha tubulin antibody (1:1000) (EMD Millipore) and 1:1000 γ-tubulin polyclonal antibody (ab11317 Abcam) in 5% BSA/PBST for 48 hrs at room temperature on a rocker. We rinsed the samples 3X in PBST over the course of 2 hours, before incubating them in anti-rabbit Alexa Fluor 594-conjugated secondary (Abcam, 1:2000) in 5% BSA/PBST, 4 hours at room temperature. Samples were subjected to 2X 10 minute washes in PBST and once in PBS for 10 minutes before mounting in 90% glycerol on chamber slides made from double-sided tape using 24 x 24 mm coverslips with a thickness no. 1.5 and sealed with VALAP.

Image Analysis

Measuring the distance of the male pronucleus from the cell center

The center of the cell was defined as one half the cell diameter (or radius) as measured from the plasma membrane to the cell interior in maximum intensity projections of time-lapse confocal images (Figure 1B). The distance from the center of the male pronucleus at the end of migration was then measured to the cell center using Fiji (ImageJ). The average distance was then calculated for all of our samples in each condition. Differences in averages were then calculated using a standard ANOVA in Graphpad Prism 8.

Measuring the average time required for the male pronucleus to center

The center of the cell was defined as outlined above. The amount of time between fertilization and the completion of centration was estimated by calculating the total elapsed time between sperm entry (estimated by when the male pronucleus first becomes visible) and the first image frame in which the male pronucleus reaches the estimated cell center using Fiji (ImageJ) (Figure 1C). This elapsed time was then averaged, and differences where calculated using an Unpaired t-test in Graphpad Prism 8.

Correlation analysis of aster diameter and cell diameter

Immunofluorescence z-projections of of asters in centrifuged eggs acquired in chapter two were repurposed for this analysis (see Chapter 2 for method details for centrifugation). To measure aster diameter six radial lines at approximately 45 degree angles from each other were drawn from one side of the aster boundary to the direct opposite side in Fiji (ImageJ). Each of these lines was drawn through the MTOC as a central point of reference. The length of each of these lines was then averaged, resulting in an estimated aster diameter for each cell, represented as an individual data point when plotted (Figure 1D). Cell diameter was estimated in the same way, instead using the cell boundaries as the beginning and end of each of the six lines.

Average aster diameter for each cell was compared to the diameter of the cell from which it was measured using a Pearson Correlation analysis and plotted as aster diameter as a function of cell diameter. We then applied a linear regression analysis in order to test the potential for linear correlation between aster and cell diameters. Both of these analyses were performed using Graphpad prism 8.

References

Alfaro-Aco, R., Thawani, A., and Petry, S. (2017). Structural analysis of the role of TPX2 in branching microtubule nucleation. J. Cell Biol. *216*, 983 LP – 997.

Alfaro-Aco, R., Thawani, A., and Petry, S. (2020). Biochemical reconstitution of branching microtubule nucleation. Elife *9*, e49797.

Basnet, N., Nedozralova, H., Crevenna, A.H., Bodakuntla, S., Schlichthaerle, T., Taschner, M., Cardone, G., Janke, C., Jungmann, R., Magiera, M.M., et al. (2018). Direct induction of microtubule branching by microtubule nucleation factor SSNA1. Nat. Cell Biol. *20*, 1172–1180.

Bennett, J., and Mazia, D. (1981). Interspecific Fusion of Sea Urchin Eggs. Exp. Cell Res. *131*, 197–207.

Bergen, L.G., Kuriyama, R., and Borisy, G.G. (1980). Polarity of microtubules nucleated by centrosomes and chromosomes of Chinese hamster ovary cells in vitro. J. Cell Biol. *84*, 151 LP – 159.

Chambers, E.L. (1939). The Movement of the Egg Nucleus in Relation to the Sperm Aster in the Echinoderm Egg. J. Exp. Biol. *16*, 409 LP – 424.

Chambers, R. (1909). Einfluss der Eigrosse und der Temperature auf das Wachsthum und die Grosse des Frosches und dessen Zellen (The Influence of the Size of the Egg and Temperature on the Growth of the Frog). Univ. Chicago Press Am. Soc. Nat. *43*, 57–62.

Conklin, E.G. (1912). Cell size and nuclear size. J. Exp. Zool. *12*, 1–98.

David, A.F., Roudot, P., Legant, W.R., Betzig, E., Danuser, G., and Gerlich, D.W. (2019). Augmin accumulation on long-lived microtubules drives amplification and kinetochore-directed growth. J. Cell Biol. *218*, 2150–2168.

Decker, M., Jaensch, S., Pozniakovsky, A., Zinke, A., O'Connell, K.F., Zachariae, W., Myers, E., and Hyman, A.A. (2011). Limiting Amounts of Centrosome Material Set Centrosome Size in C. elegans Embryos. Curr. Biol. *21*, 1259–1267.

Dogterom, M., and Yurke, B. (1997). Measurement of the Force-Velocity Relation for Growing Microtubules. Science (80-.). *278*, 856–860.

Goehring, N.W., and Hyman, A.A. (2012). Organelle Growth Control through Limiting Pools of Cytoplasmic Components. Curr. Biol. *22*, R330–R339.

Good, M.C., Vahey, M.D., Skandarajah, A., Fletcher, D.A., and Heald, R. (2013). Cytoplasmic Volume Modulates Spindle Size During Embryogenesis. Science (80-.). *342*, 856 LP – 860.

Hazel, J., Krutkramelis, K., Mooney, P., Tomschik, M., Gerow, K., Oakey, J., and Gatlin, J.C. (2013). Changes in Cytoplasmic Volume Are Sufficient to Drive Spindle Scaling. Science (80-.). *342*, 853 LP – 856.

Holy, T.E., Dogterom, M., Yurke, B., and Leibler, S. (1997). Assembly and positioning of microtubule asters in microfabricated chambers. Proc. Natl. Acad. Sci. *94*, 6228 LP – 6231.

Ishihara, K., Nguyen, P.A., Groen, A.C., Field, C.M., and Mitchison, T.J. (2014). Microtubule nucleation remote from centrosomes may explain how asters span large cells. Proc. Natl. Acad. Sci. *111*, 17715 LP – 17722.

Ishihara, K., Korolev, K.S., and Mitchison, T.J. (2016). Physical basis of large microtubule aster growth. Elife *5*.

Kanehisa, M. (2019). Toward understanding the origin and evolution of cellular organisms. Protein Sci. *28*, 1947–1951.

Kanehisa, M., and Goto, S. (2000). KEGG: kyoto encyclopedia of genes and genomes. Nucleic Acids Res. *28*, 27–30.

Kanehisa, M., Sato, Y., Furumichi, M., Morishima, K., and Tanabe, M. (2019). New approach for understanding genome variations in KEGG. Nucleic Acids Res. *47*, D590–D595.

King, M.R., and Petry, S. (2020). Phase separation of TPX2 enhances and spatially coordinates microtubule nucleation. Nat. Commun. *11*, 270.

Lacroix, B., Letort, G., Pitayu, L., Sallé, J., Stefanutti, M., Maton, G., Ladouceur, A.-M., Canman, J.C., Maddox, P.S., Maddox, A.S., et al. (2018). Microtubule Dynamics Scale with Cell Size to Set Spindle Length and Assembly Timing. Dev. Cell *45*, 496-511.e6.

Meaders, J.L., and Burgess, D.R. (2020). Microtubule-Based Mechanisms of Pronuclear Positioning. Cells *9*, 505.

Mitchison, T., and Kirschner, M. (1984). Dynamic instability of microtubule growth. Nature *312*, 237–242.

Mukherjee, R.N., Sallé, J., Dmitrieff, S., Nelson, K.M., Oakey, J., Minc, N., and Levy, D.L. (2020). The Perinuclear ER Scales Nuclear Size Independently of Cell Size in Early Embryos. Dev. Cell.

Petry, S., Groen, A.C., Ishihara, K., Mitchison, T.J., and Vale, R.D. (2013). Branching Microtubule Nucleation in Xenopus Egg Extracts Mediated by Augmin and TPX2. Cell *152*, 768–777.

Song, J.-G., King, M.R., Zhang, R., Kadzik, R.S., Thawani, A., and Petry, S. (2018). Mechanism of how augmin directly targets the γ-tubulin ring complex to microtubules. J. Cell Biol. *217*, 2417 LP – 2428.

Tanimoto, H., Kimura, A., and Minc, N. (2016). Shape–motion relationships of centering microtubule asters. J. Cell Biol. *212*, 777 LP – 787.

Thawani, A., Stone, H.A., Shaevitz, J.W., and Petry, S. (2019). Spatiotemporal organization of branched microtubule networks. Elife *8*, e43890.

Tran, P.T., Marsh, L., Doye, V., Inoué, S., and Chang, F. (2001). A Mechanism for Nuclear Positioning in Fission Yeast Based on Microtubule Pushing. J. Cell Biol. *153*, 397 LP – 412.

Verma, V., and Maresca, T.J. (2019). Direct observation of branching MT nucleation in living animal cells. J. Cell Biol. *218*, 2829–2840.

Wesley, C.C., Mishra, S., and Levy, D.L. (2020). Organelle size scaling over embryonic development. Wiley Interdiscip. Rev. Dev. Biol. e375.

West, G.B., and Brown, J.H. (2005). The origin of allometric scaling laws in biology from genomes to ecosystems: towards a quantitative unifying theory of biological structure and organization. J. Exp. Biol. *208*, 1575 LP – 1592.

Chapter 4. Conclusions and Final Discussion

Nearly four decades of research investigating aster positioning have uncovered elaborate details for elegant pulling mechanisms, which drive aster migration in the context of large developmental cells. The work presented in this dissertation contributes to the field by uncovering a novel MT-based pushing mechanism for aster positioning in the large (~100 µm) sea urchin zygote (Figure 1), a process previously thought to be exclusive to very small cell types (Meaders et al., 2020). Our model, which we present the bulk of in Chapter 2, proposes that pushing from rear microtubules extending behind the sperm aster are essential for centration of the sea urchin sperm aster and its associated male pronucleus (Figure 1).

There are still several important details left to investigate in future research. The first is the mechanism for pushing on a molecular level. In Chapter 2 we present data that indicates MT aster migration rates match growth rates of the rear portion of the aster and not front portions (Figure 1 and Chapter 2, Figure 2), which suggests that pushing is driven by growth rates of the rear portion of the aster. These data are consistent with a possible mechanism by which MT polymerization against the rear cortex drives the aster forward. However, we have not ruled out a motor driven mechanism for pushing. For example, cytoplasmic kinesins may contribute to pushing in a manner similar to dynein in the proposed cytoplasmic MT-length dependent pulling model. In this hypothesis, a longer rear portion of the aster relative to the front would result in a greater number of kinesin motors moving toward MT plus-ends on the rear than the front, netting greater pushing from the rear of the aster and propelling it forward. This idea may be tested in the future by microinjection of different anti-kinesin inhibitory antibodies (Ingold et al., 1988), and measuring aster migration dynamics.

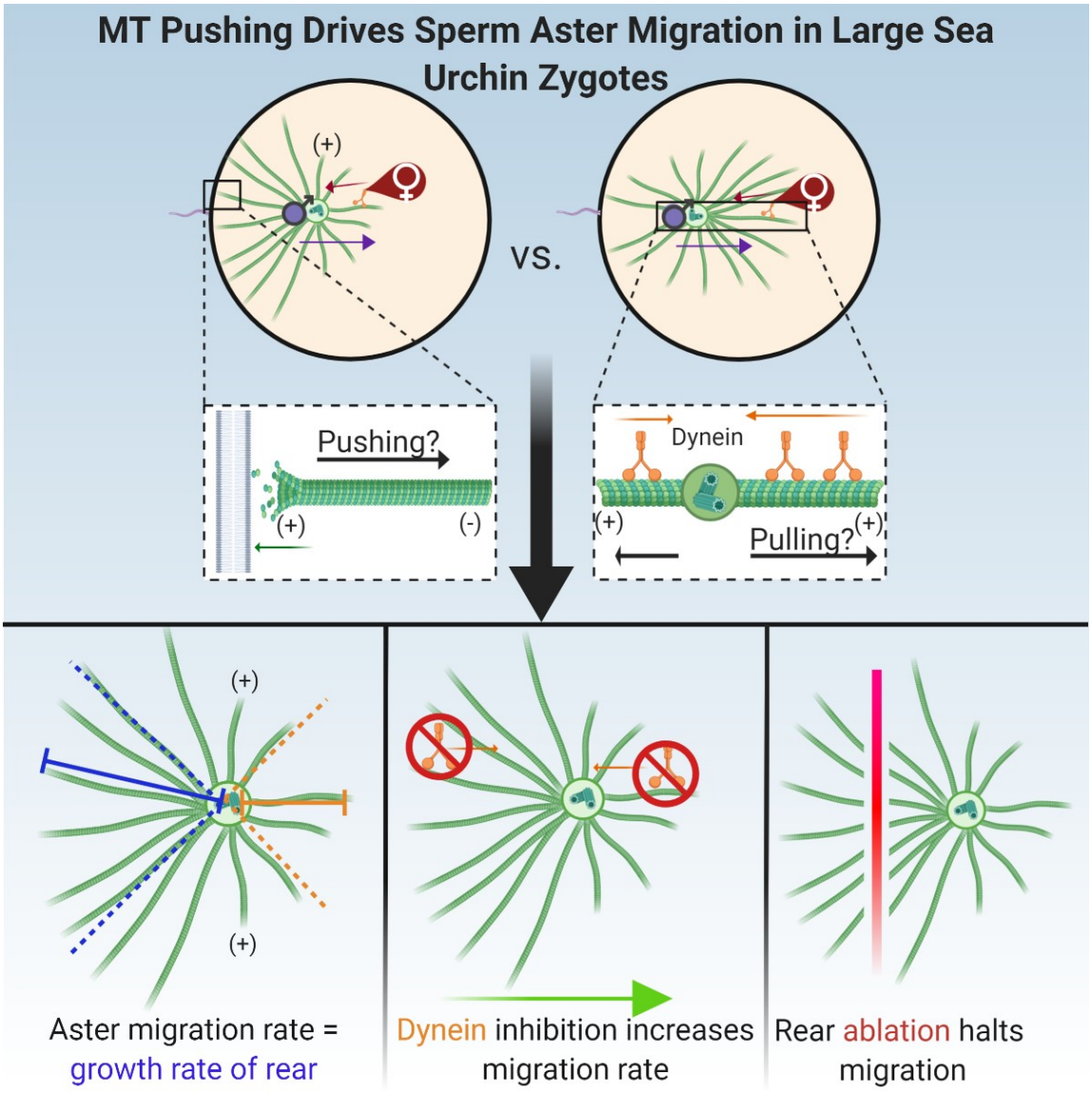

Figure 1. Model for Force Generating Mechanism during Aster Positioning in Sea Urchin Zygotes

Top panel: Proposed models for sperm aster centration in sea urchin zygotes. Left, pushing: MT polymerization of rear astral MTs against the rear cortex may propel the sperm aster forward toward the cell center. Right, pulling: Aster length asymmetries translates to more cytoplasmic dynein on front portions of the aster than rear portions, which results in greater pulling forces forward toward the cell center. **Bottom left panel:** We find in this body of work that the rear portion of the aster (blue) is longer than the front (orange), and aster migration rates match growth rates of rear portions of the sperm aster. **Bottom middle panel:** We also find that dynein inhibition using p150-CC1

increases aster migration. **Bottom right panel:** We show that ablation of rear portions of the sperm aster halts aster migration, while side and front ablations do not, providing direct evidence for a pushing model driven by rear MTs.

A second important aim for future research is determining how the rear aster grows longer and more dense than the front. In terms of density, a simple explanation is that the spherical curvature of the egg boundaries restricts range of motion of rear MTs near the cortex more than front cytoplasmic MTs. This restricted range near the cortex may condense rear MTs leading to a more dense rear astral region when compared to the front. Testing this hypothesis may be done by forcing eggs into PDMS chambers (Chang et al., 2014) containing curvatures with a more restrictive range of motion, or higher angles, and measuring whether or not these curvatures induce greater MT density. In terms of aster lengths, it is intuitive to assume that the front portion of the aster would grow longer than the rear because rear lengths are limited by the nearby rear cortex, while front portions have a greater cytoplasmic volume to expand into. We therefore favor active regulation of MT dynamics within the aster and/or at astral MT-plus ends to enable longer rear aster radii. These regulators may include TPX2, which is involved in regulating MT dynamics and MT branching within mitotic asters and the spindle (Alfaro-Aco et al., 2020; Petry et al., 2013; Verma and Maresca, 2019). One testable assumption of this model is that TPX2 and/or other regulatory factors may be asymmetrically distributed within the sperm aster. A second testable assumption is that TPX2 dysregulation should alter aster growth dynamics, resulting in asters of different size, shape, and/or migration dynamics. Finally, aster lengths may be regulated by cortical and/or cytoplasmic factors. For example, at the cortex dynamics such as growth rates and MT stability may be regulated in ways that enforce net growth more than front portions of the aster which do not interact with the cortex. Future studies targeting potential MT length regulatory factors at the cortex will be required to test this hypothesis.

Lastly, and perhaps most importantly, is the relevance of a pushing mechanism during aster positioning in other developmental models. In very large cell types, such as frog eggs in which MT asters must migrate hundreds of microns to the cell center (Chapter 1, Chart 1), we would expect a pulling model to dominate due to less physical limitations compared to a pushing model. However, a very recent study published at the time of writing this dissertation found that large interphase asters in frog extracts are pushed to the center of PDMS chambers in the absence of cytoplasmic dynein activity (Sulerud et al., 2020). Similar to our predictions, this recent study hypothesizes that large asters may overcome the proposed buckling/slipping limitations of a pushing mechanism through MT branching and/or bundling. While the chambers used in this study are similar in size to sea urchin zygotes, the authors present powerful evidence for a MT pushing based mechanism used to drive interphase aster migration for the first time in a frog system (Sulerud et al., 2020). Thus, their findings provide initial support that the MT-based pushing model uncovered in this dissertation may be an evolutionarily conserved feature, rather than exclusive to sea urchin eggs. Taken together this body of work prompts a reconsideration of the dogmatic pulling-based models currently used to explain aster positioning in large cell types.

References

Alfaro-Aco, R., Thawani, A., and Petry, S. (2020). Biochemical reconstitution of branching microtubule nucleation. Elife *9*, e49797.

Chang, F., Atilgan, E., Burgess, D., and Minc, N. (2014). Manipulating Cell Shape by Placing Cells into Micro-fabricated Chambers. In Mitosis: Methods and Protocols, D.J. Sharp, ed. (New York, NY: Springer New York), pp. 281–290.

Ingold, A.L., Cohn, S.A., and Scholey, J.M. (1988). Inhibition of kinesin-driven microtubule motility by monoclonal antibodies to kinesin heavy chains. J. Cell Biol. *107*, 2657–2667.

Meaders, J.L., de Matos, S.N., and Burgess, D.R. (2020). A Pushing Mechanism for Microtubule Aster Positioning in a Large Cell Type. Cell Rep. *33*, 108213.

Petry, S., Groen, A.C., Ishihara, K., Mitchison, T.J., and Vale, R.D. (2013). Branching Microtubule Nucleation in Xenopus Egg Extracts Mediated by Augmin and TPX2. Cell *152*, 768–777.

Sulerud, T., Sami, A.B., Li, G., Kloxin, A., Oakey, J., and Gatlin, J. (2020). Microtubule-dependent pushing forces contribute to long-distance aster movement and centration in Xenopus laevis egg extracts. Mol. Biol. Cell *0*, mbc.E20-01-0088.

Verma, V., and Maresca, T.J. (2019). Direct observation of branching MT nucleation in living animal cells. J. Cell Biol. *218*, 2829–2840.